Experimental demonstration of high-fidelity entanglement via Rydberg blockade

Craig J. Picken

Abstract

The strong dipole interactions of Rydberg atoms are ideal candidates to facilitate interactions between neutral atoms to generate entanglement for quantum information processing. This offers the potential to scale to large atom arrays through well established techniques for neutral atoms, overcoming limitations of other architectures for quantum information processing. This thesis presents the design and development of an experiment for quantum information processing using Rydberg atoms, concluding with the deterministic preparation of two caesium atomic qubits in a maximumly entangled Bell state.

The experiment presented achieves low error readout of two single atoms held in optical tweezers using new imaging technology as an alternative to what is typically used in the field, offering a cost effective solution whilst maintaining high shot to shot retention as is necessary for qubit operations. Qubit manipulations are demonstrated with fast two-photon rotations between the hyperfine ground states and the $69S_{1/2}$ Rydberg state. Due to the cold single atom temperatures achieved, $T \approx 10$ μK, the ground-Rydberg dephasing times measured through Ramsey spectroscopy find coherence times around twice that of previously reported experiments, over an order of magnitude greater than the gate time.

Demonstration of Rydberg blockade between two atoms with a separation of 6 μm is shown with an almost compete suppression to the doubly excited state and observation of a $\sqrt{2}$-enhancement of coupling to an entangled symmetric $|\mathcal{W}\rangle$ state. Finally the $|\mathcal{W}\rangle$ state is mapped to the ground state qubit levels to create a maximally entangled Bell state achieving a loss-corrected fidelity of $\mathcal{F}_{pairs} = 0.81 \pm 0.05$. This result represents the highest corrected ground state neutral atom entanglement fidelity via Rydberg blockade and is equal to that achieved via Rydberg dressing . The limitation of this Bell

state preparation is primarily due to laser phase noise as found in other experiments and is verified through the long coherence times measured in this thesis. Generation of entanglement in the magnetically insensitive hyperfine states of caesium allows long coherence times to be achieved with Ramsey spectroscopy used to measured transverse dephasing times of $T_2^* = 10 \pm 1$ ms and $T_2' = 150 \pm 20$ ms, offering an excellent platform for quantum computation.

Experimental demonstration of high-fidelity entanglement via Rydberg blockade

Craig J. Picken

A thesis submitted in partial fulfilment
of the requirements for the degree of
Doctor of Philosophy

Department of Physics
University of Strathclyde

April 30, 2019

Contents

List of Figures

Declaration

I confirm that no part of the material offered has previously been submitted by myself for a degree in this or any other University. Where material has been generated through joint work, the work of others has been indicated.

Craig J. Picken
Glasgow, April 30, 2019

Acknowledgements

The last three years have presented an enduring, but at most of the time enjoyable, experience and I would like to take this opportunity to thank the people who have helped me along the way. First my thanks go to my supervisor Jon Pritchard for giving me the opportunity to take on this project. I have been very fortunate to have a supervisor who is on hand to answer daily questions and readily available to assist in the lab which has really helped in progression of the experiment. Secondly I would like to thank Erling Riis for encouraging and giving me the chance to continue my studies after an unfortunate start to this journey. I would also like to thank Paul Griffin for always being happy to help and answer questions. Thanks also to Aidan Arnold for many useful suggestions at group meetings. Special thanks go out to Rémy who began this PhD journey with me three years ago, the progress we have made in this time could not of been done without you and to Katie for your help in the lab towards the end. I would also like to thank every member of the EQOP group past and present for providing a friendly working environment, I have felt very welcome from day one and will truly miss working here.

Finally I would like to thank my parents, sisters and grandfather for their continued love and support over not just the last three years but my whole life, and Sarah for your understanding and endless encouragement during this journey.

For your endless love, support and encouragement
this thesis is dedicated to Sarah, Mum and Dad.

Part I

Introduction to quantum information processing with Rydberg atoms

Chapter 1

Quantum Information - a primer

Quantum information processing is an area which has seen rapid progression in recent years, due to the major advantages potentially offered through quantum mechanics in comparison to conventional computing. For example quantum entanglement offers unprecedented levels of security via quantum cryptography [1–4], and provides a platform to overcome the limitations of classical computation through potential exponential increases in processing speeds though quantum computation [5–9]. Full realisation of fault tolerant quantum computing requires harnessing over a million of qubits [10] far exceeding current advancements in the field. However small scale systems using only a few qubits can still be utilised with simulations already been performed on quantum computers to calculate electronic structure of molecules using variational quantum eigensolvers [11, 12] and factorisation of small numbers via Shor's algorithm [13]. The building block behind all this is a two-level quantum system known as a qubit.

1.1 The Qubit

This opportunity to revolutionise modern day computation is provided by quantum mechanics. A qubit is a two-level system represented by logical states $|0\rangle$ and $|1\rangle$. The state vector of a such a system is given by

$$|\psi\rangle = \alpha|0\rangle + \beta|1\rangle \equiv \begin{pmatrix} \alpha \\ \beta \end{pmatrix}, \tag{1.1}$$

where $|\alpha|^2$ ($|\beta|^2$) represents the probability of being in state $|0\rangle$ ($|1\rangle$) such that $|\alpha|^2 + |\beta|^2 = 1$. The advantage quantum mechanics offers over the classical bit, which has discrete values of 0 and 1, lies in the ability to create superposition states such as

$$|\psi\rangle = \frac{1}{\sqrt{2}}(|0\rangle + |1\rangle). \tag{1.2}$$

Despite the qubit potentially occupying infinite linear combinations of α or β only two outcomes are presented from measurement with a 50 % probability of measuring $|0\rangle$ or $|1\rangle$ for the example presented above. However as we will see the real power in quantum computation lies in the ability to create entanglement.

1.1.1 Quantum Entanglement

Whilst this superposition can be understood from a classical viewpoint, the concept of entanglement has no classical analog and is a quirk of the quantum world. Consider two qubits, A and B, in states $|\psi\rangle_A$ and $|\psi\rangle_B$, as with the case above either qubit can be in state $|0\rangle$ or $|1\rangle$ or any superposition. The two qubits can therefore also be described by a linear combination of two qubit states given by

$$|\Psi\rangle = \alpha|00\rangle_{AB} + \beta|10\rangle_{AB} + \gamma|10\rangle_{AB} + \delta|11\rangle_{AB}, \tag{1.3}$$

normalised such that $|\alpha|^2 + |\beta|^2 + |\gamma|^2 + |\delta|^2 = 1$. Typically, for a pair of qubits, the system starts off uncorrelated and it is possible to describe the state of qubit A independent of qubit B, resulting in a product state $|\Psi\rangle = |\psi\rangle_A \otimes |\psi\rangle_B$. If, however, the qubits become correlated it is possible to create states where the qubits are no longer independent of each other. An example of such a state is given by

$$|\Psi^-\rangle = \frac{1}{\sqrt{2}}(|01\rangle - |10\rangle). \tag{1.4}$$

This inseparable state can not be produced by a product of two single qubit states $|\Psi^-\rangle \neq |\psi\rangle_A \otimes |\psi\rangle_B$ and is an example of a maximally entangled Bell state. Measurements upon such states lead to some remarkable consequences which truly highlight the bizarre nature of the quantum world. For example consider two observers, Alice and Bob far apart conducting measurements on each of the qubits after being prepared in the above state. Both will measure $|0\rangle$ or $|1\rangle$ with a 50 % probability, however every time the Alice measures $|0\rangle$ Bob will measure $|1\rangle$ and vice-versa. Further to this, as long as Alice and Bob conduct their measurements in the same basis the outcome remains the same and is not dependent on the basis chosen. This perfect anti-correlation in the outcomes of the measurements presents an interesting problem as quantum mechanics tells us that each qubit is in a superposition until it is measured, therefore if quantum mechanics is to be believed the result of the measurement of qubit A instantly impacts the state of qubit B. Intuitively one may think that this instantaneous effect presents a method of faster than light signalling between Alice and Bob, however, this is not possible as the outcome of first measurement will always be random and requires a classical communication channel between Alice and Bob to determine the basis used to be able to transfer genuine information. Nonetheless this concept of a non-local influence on the qubit famously troubled Einstein with him describing it as "spooky action at a distance". This led him to believe that our description

of quantum mechanics was incomplete and to introduce the concept of local hidden variables to describe this phenomenon [14].

This remained a contentious topic until John Bell in the 1960s derived inequalities for a series of measurements conducted in different bases on an entangled pair defining the constraints of any hidden variable theory [15]. The theorem states that for any local hidden variables the following inequality must hold [16]

$$1 + P(\vec{b}, \vec{c}) \geq |P(\vec{a}, \vec{b}) - P(\vec{a}, \vec{c})|, \tag{1.5}$$

where $P(\vec{i}, \vec{j})$ is the correlation probability of spin measurements along $\vec{i}$ and $\vec{j}$ for qubit A and B. To test this inequality Alice and Bob can set their detectors to one of the three orientations to measure the qubit's state. Let us consider what happens when $\vec{a}$ is orientated along $\vec{x}$, $\vec{b}$ along $\vec{y}$ and $\vec{c}$ to be $(\vec{x} + \vec{y})/\sqrt{2}$. From quantum mechanics we can find that $P(\vec{i}, \vec{j}) = -\vec{i} \cdot \vec{j}$ which for our chosen orientations gives correlation probabilities of $P(\vec{a}, \vec{b}) = 0$ and $P(\vec{a}, \vec{c}) = P(\vec{b}, \vec{c}) = -0.707$ violating the inequality. Several experiments have been performed to test variants of this inequality and have found violations [17, 18], therefore confirming the behaviour of entangled particles to be non-local. These experiments however do not necessarily prove the quantum mechanical description to be correct, but rather prove entanglement violates local realism.

1.1.2 Realisation

Utilising the tools of superposition and entanglement quantum computers can solve classically computationally demanding problems using sophisticated quantum algorithms such as Shor's algorithm for factorising large numbers [6] or Grover's search algorithm [19], with the former offering an exponential speed up in comparison to classical computation. The criteria

for the successful implementation of a quantum computer are known as the DiVincenzo criteria given by [20]:

- a scalable physical system with well characterised qubits,
- the ability to initialise the qubit's quantum state,
- long coherence times in comparison to gate operation time..
- a universal set of quantum gates,
- the ability to measure qubit's state.

Satisfying these criteria has seen several candidate two-level systems proposed most notably, ions [21], superconducting circuits [22] and Rydberg atoms [23].

1.2 State of the Art

Significant technological advancements have been realised using ions and superconductors as a quantum architecture. Ion technologies have shown the highest fidelities achieving single qubit gate fidelities of $\mathcal{F} > 0.9999$ and two qubit gate fidelities of $\mathcal{F} > 0.999$ [24, 25] with single qubit coherence times of over a second observed [26]. A key issue in these studies is the trade off between gate speed and achieved fidelities, with the fore-mentioned results requiring gate times of 10-50 μs. A recent study has however overcome this limitation achieving a two-qubit gate with a gate speed of $\tau = 1.6$ μs and a fidelity of $\mathcal{F} = 0.998$ [27]. This demonstrated gate speed is over an order of magnitude increase compared to previous high fidelity studies and represents a significant advancement taking fast ion gates close to realms of fault-tolerant quantum computing $\mathcal{F} > 0.9999$. Recent progress has seen a 5-qubit processor developed and used to perform a 3-qubit Groover search [28, 29].

Similarly superconducting circuits have achieved single gate fidelities of $\mathcal{F} = 0.9992$ and two-qubit fidelities of $\mathcal{F} = 0.994$ using gate durations of 10's of ns [30]. This success has seen development of several commercial quantum computers in search of achieving quantum supremacy [31], with Intel, IBM and Google having built 49 [32], 50 [33] and 72 [34] qubit processors respectively based on superconducting technology and Rigetti in the midst of developing a 128 qubit chip [35]. Advancements as such have already seen commercial use with IBM already offering cloud based access to quantum computers with architectures containing up to 20 qubits. A key challenge for current systems is scalability with high fidelity operations currently only being performed on small numbers of qubits.

Neutral atoms can overcome this limitation with scalable trapping easily implemented through microscopic dipole traps [36] or optical lattices [37], allowing large 2D arrays of neutral atoms to be realised [38, 39]. Previous limits due to probabilistic loading have been recently overcome using dynamically reconfigurable traps [40], which can be deterministically assembled atom-by-atom to create defect free arrays of up to $\sim$100 qubits with extension to arbitrary 3D geometries demonstrated [41, 42]. Further to this the hyperfine ground state of neutral atoms are excellent candidates for computational basis states of a qubit due to their long coherence times, with storages times exceeding a minute being observed [43].

Interactions between ground state neutral atoms separated by more than several angstroms are negligible. Therefore, provision of interactions to facilitate multi-qubit gates and entanglement is experimentally challenging. This has been overcome using mobile optical tweezers to overlap pairs of atoms and exploit spin exchange interactions to generate entanglement [44]. An alternative method of providing interactions between neutral atoms uses Rydberg atoms, where large dipolar interactions act over much longer ranges than ground state atoms [23, 45].

Property	n-scaling
Binding Energy	n^{-2}
Adjacent State Energy	n^{-3}
Radiative Lifetime	n^{3}
Orbital Radius	n^{2}
Dipole Moment $\langle n'l'm_l'\|\mu\|nlm_l\rangle$	n^{2}

Table 1.1: Scaling properties of Rydberg atoms.

1.3 Rydberg Atoms

Rydberg atoms are atoms which have been excited to high principal quantum number, n. These states have large orbital radii which lead to a number of exaggerated properties, most importantly in the context of this work a dipole moment, μ which scales as $\mu \propto n^2$ which leads to strong interaction potentials. Further to this, Rydberg atoms have long radiative lifetimes typically on the order of $\tau > 100$ μs, with even longer durations found at cryogenic temperatures making them ideal for quantum gate protocols. This far exceeds the timescale of gate operations which are typically less than a μs long allowing high fidelity operations. A summary of these properties and their scaling with n is shown in Table 1.1.

These properties form an excellent platform for implementing quantum gates with the large dipole moment giving rise to a mechanism known as dipole blockade [46]. In this regime the large dipole interactions between Rydberg atoms results in an energy shift such that excitation of more than one atom within a distance known as the blockade radius is inhibited. The mechanisms behind this will be further explained in Sec. 3.4, however importantly in the context of neutral atom quantum information the Rydberg blockade can be facilitated over distances as large as 10 μm, much greater than the required separation for ground state interactions. As each atom within the blockade radius is equally likely to be excited to the Rydberg state, Rydberg blockade can also be used to create an entangled symmetric state which exhibits a collective $\sqrt{N}$ enhancement in coupling [46]. This mechanism can

be used to effectively implement fast two-qubit gates [23, 45] in comparison to ion based experiments and perform efficient processing of quantum algorithms such as Grover's search algorithm [47, 48]. Further to this the strong interactions of Rydberg atoms have also seen a great deal of focus within quantum simulation and have been used to perform simulations of quantum magetism [49–52].

1.3.1 Recent Experimental Advances

Evidence of suppression of Rydberg excitations and collective behaviour has been demonstrated in several experiments using large samples of cold atoms [53–56], however use in quantum gate protocols require using single pairs of atoms. Progression to experiments utilising Rydberg atoms in quantum gates has seen rapid progression in recent years beginning with the successful demonstration of sub-Poissonian loading of single atoms [57] through collisional blockade [58]. Since then major milestones towards blockade between two atoms have included demonstration of resolvable qubit rotations of two atoms within the blockade radius [59] and coherent single atom excitation to the Rydberg state [60, 61]. Experimental verification of blockade between two atoms was first achieved in 2008 by the group of Mark Saffman in Wisconsin using individual addressing [62] and by the group of Antoine Browaeys in Paris using global addressing [63]. This was quickly followed with demonstration of ground state entanglement through mapping the entangled Rydberg state to the ground state [64, 65] and via a CNOT gate [66, 67]. Progression since these results has seen post corrected ground state fidelities of up to $\mathcal{F} = 0.81$ achieved [68]. Table 1.2 summarises landmark achievements in ground state entanglement fidelities prior to the main results presented in this thesis.

Species	Method	Deterministic	Post Selected	Ref
^{87}Rb	Blockade	0.46	0.75 ± 0.07	[64]
^{87}Rb	Blockade	0.48 ± 0.07	0.58	[66]
^{87}Rb	Blockade	0.58 ± 0.04	0.71 ± 0.05	[67]
^{133}Cs	Blockade	0.73 ± 0.05	0.79 ± 0.05	[38]
^{87}Rb	Spin Exchange	0.44	0.63 ± 0.02	[44]
^{133}Cs	Dressing	0.6 ± 0.03	0.81± 0.02	[68]
^{87}Rb/^{85}Rb	Blockade	0.59 ± 0.03	-	[69]

Table 1.2: Experimentally achieved entanglement fidelities between two neutral atoms, error bars shown where they were available in literature.

1.3.2 A Hybrid Quantum System

These current advancements are, however, far below the required fidelity $\mathcal{F} > 0.9999$ for fault tolerant quantum computing and significantly behind progress in ion [25] and superconducting circuit [30] entanglement fidelities. A possible solution to overcome this could be to integrate two quantum technologies into a hybrid system with the strong microwave transitions between adjacent Rydberg states offering strong coupling to a superconductung microwave resonator [70, 71]. A potential proposal for such a scheme is outlined in [71], where a neutral atom is trapped above the electric field antinode of a coplanar waveguide resonator (CPW) and offers a route to entangle neutral atoms with the microwave cavity field. Strong coupling with a CPW also offers the potential to generate entanglement over mm scales between atoms trapped at different antinodes [72] which due to the characteristic of blockade can be extended to ensembles

The objective of the experiment presented in this thesis looks towards eventually establishing a hybrid quantum system similar to the one described above. The work presented in this thesis comprises of the building blocks towards this experiment and therefore attention to the design for future integration of cryogenic systems needs to be considered.

1.4 Thesis Layout

This thesis is divided into 5 parts and is structured as follows: Part I introduces the concept of quantum information and how Rydberg atoms can be used to implement a neutral atom gate. Part II describes the basic properties of Rydberg atoms and describes the relevant theory and calculations for the qubit operations and excitation to the Rydberg state $69S_{1/2}$. Part III provides a focus on the experiment design and single atom cooling and trapping. Part IV presents qubit rotations between the hyperfine ground states and to the Rydberg state and measurement of their dephasing as well as demonstration of Rydberg blockade and high fidelity ground state entanglement. Finally Part V provides an outlook on the achieved results examining possible routes to improve the experiment and future planned work beyond this thesis.

Part I

- Chapter 2 builds on the topics covered in this introduction and introduces quantum gate rotations.

Part II

- Chapter 3 introduces the relevant properties of Rydberg atoms which make them ideal for quantum gates as well as examining the underlying mechanisms which lead to Rydberg blockade.
- Chapter 4 contains theory behind two-photon transitions utilised in this thesis and presents calculations of expected results.

Part III

- Chapter 5 describes the experimental setup from initial design considerations to a source of cold atoms for optical transport.

- Chapter 6 presents single atom trapping setup as well as single atom characterisations.

Part IV

- Chapter 7 presents demonstration of fast optical rotations between the hyperfine ground states of caesium with further measurements using Ramsey spectroscopy to show long ground state coherence times.
- Chapter 8 presents demonstration of two photon excitation the Rydberg state and examines possible causes of dephasing.
- Chapter 9 presents demonstration of Rydberg blockade and mapping of the resulting symmetric entangled state towards the other qubit ground state to deterministically create a Bell state.

Part V

- Chapter 10 summarises the main results of this thesis and provides an outlook and future direction of the experiment.

1.5 Publications

1.5.1 Arising from this work

- C.J. Picken *et al.*, *Entanglement of neutral-atom qubits with long ground-Rydberg coherence times*, Quantum Science and Technology **4**, 01501. (2019).

- C.J. Picken *et al.*, *Single atom imaging with an sCMOS camera*, App. Phys. Lett. **111**, 164102 (2017).

1.5.2 Other publications relating to this work

- R. Legaie *et al.*, *Sub-kHz excitation lasers for Quantum Information Processing with Rydberg atoms*, J. Opt. Soc. Am. B **35**, 892 (2018).

1.5.3 Role of Author

The work presented in this thesis represents the progression of an empty laboratory to a workspace capable of creating deterministic entanglement between neutral atoms over a period of three years. Such an accomplishment could, not of, course been achieved through the work of the author alone. The work presented runs co-currently with the PhD work of Rémy Legaie with both students working under the supervision of Dr Jonathan Pritchard and with Katie M^{c}Donnell joining the team for the final year. R. Legaie undertook development of the ultra low expansion reference cavity and laser systems for Rydberg excitation while the author undertook development of the vacuum system, optical transport design and single atom trapping. K. M^{c}Donnell developed the Qubit B laser used for ground state rotations. The author then led the work on coherent qubit operations and entanglement with all data presented in this thesis taken by the author.

Chapter 2

Qubit Rotations and Gates

Quantum information and computing rely on the ability to manipulate a qubit's quantum state and to perform gate operations on qubits. This chapter presents an introduction to the visualisation of such rotations and how they can be used to create on demand entanglement.

2.1 Single Qubit Rotations

To understand qubit operations it is useful to introduce a visual representation known as the Bloch sphere. As $|\alpha|^2 + |\beta|^2 = 1$, Eq. 1.1 can be re-written as [9]

$$|\psi\rangle = \cos\left(\frac{\theta}{2}\right)|0\rangle + e^{i\phi}\sin\left(\frac{\theta}{2}\right)|1\rangle = \begin{pmatrix} \cos\left(\frac{\theta}{2}\right) \\ e^{i\phi}\sin\left(\frac{\theta}{2}\right) \end{pmatrix}, \tag{2.1}$$

where θ and ϕ represent coordinates on this three dimensional sphere represented by the Bloch vector $(\cos\phi\sin\theta, \sin\phi\sin\theta, \cos\theta)$. The state of a single qubit can lie anywhere on this sphere, as shown in Fig 2.1.

Quantum gate operations are represented by rotations around this sphere and can be described by 2×2 matrices with the only constraint being that gate matrix U must be unitary such that $U^\dagger U = I$, where $U^\dagger$ is the adjoint

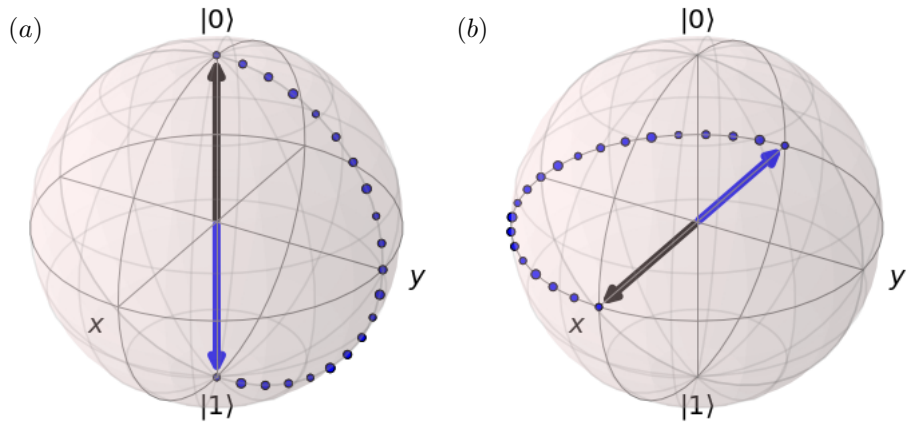

Figure 2.1: Qubit rotations on the Bloch sphere showing (a) a X-gate performing the transformation $|\psi\rangle = |0\rangle \rightarrow |\psi\rangle = |0\rangle$ and (b) a Z-gate rotating around the z-axis of the Bloch sphere $|\psi\rangle = \frac{1}{\sqrt{2}}(|0\rangle + |1\rangle) \rightarrow |\psi\rangle = \frac{1}{\sqrt{2}}(|0\rangle - |1\rangle)$ performing a global transform of phase.

of U and $I = \begin{pmatrix} 1 & 0 \\ 0 & 1 \end{pmatrix}$ is the 2×2 identity matrix. Some of the elementary gate operations required in quantum information are given by the Pauli matrices [73]

$$X = \begin{pmatrix} 0 & 1 \\ 1 & 0 \end{pmatrix}, \quad Y = \begin{pmatrix} 0 & -i \\ i & 0 \end{pmatrix}, \quad Z = \begin{pmatrix} 1 & 0 \\ 0 & -1 \end{pmatrix}. \tag{2.2}$$

Exponentiating these relations yields the rotation operators

$$U_X(\theta) = e^{-i\frac{\theta}{2}X} = \begin{pmatrix} \cos\left(\frac{\theta}{2}\right) & -i\sin\left(\frac{\theta}{2}\right) \\ -i\sin\left(\frac{\theta}{2}\right) & \cos\left(\frac{\theta}{2}\right) \end{pmatrix}, \tag{2.3}$$

$$U_Y(\theta) = e^{-i\frac{\theta}{2}Y} = \begin{pmatrix} \cos\left(\frac{\theta}{2}\right) & -\sin\left(\frac{\theta}{2}\right) \\ \sin\left(\frac{\theta}{2}\right) & \cos\left(\frac{\theta}{2}\right) \end{pmatrix}, \tag{2.4}$$

$$U_Z(\theta) = e^{-i\frac{\theta}{2}Z} = \begin{pmatrix} e^{-i\frac{\theta}{2}} & 0 \\ 0 & e^{i\frac{\theta}{2}} \end{pmatrix}. \tag{2.5}$$

Where the evolution of the state vector is given by $|\psi'\rangle = U_i(\theta)|\psi\rangle$, examples of such rotations are shown in Fig 2.1 showing an (a) X-gate and (b) Z-gate

or phase gate. The X-gate acts to invert the quantum state such that

$$X|\psi\rangle = \begin{pmatrix} 0 & 1 \\ 1 & 0 \end{pmatrix} \begin{pmatrix} \alpha \\ \beta \end{pmatrix} = \begin{pmatrix} \beta \\ \alpha \end{pmatrix}, \tag{2.6}$$

which is the quantum equivalent of a classical NOT gate inverting the quantum logic and is known as a bit-flip. The Z-gate rotates the state vector around the z-axis and results in a flip in the sign, representing a change in the qubit's phase. Another useful rotation is given by

$$H = \frac{1}{\sqrt{2}} \begin{pmatrix} 1 & 1 \\ 1 & -1 \end{pmatrix}, \tag{2.7}$$

and is known as a Hadamard transformation. This operation transforms between the bases $|0\rangle$,$|1\rangle$ and $|+\rangle$,$|-\rangle$ where $|\pm\rangle = \frac{1}{\sqrt{2}}(|0\rangle \pm |1\rangle)$ [3] and plays a crucial role in generating entanglement between two qubits.

2.2 Two-qubit Gates

The use of single qubit gates by themselves is very limited, however with certain two-qubit gates form a universal set of quantum gates for computation [9]. Two-qubit gates allow implementation of controlled operations and form the quantum equivalent of classical counterparts such as a NAND gate. These two-qubit operations comprise of a control and target qubit. A popular example of a two-qubit gate that lies at the heart of quantum computation is a Controlled NOT (C_N) gate. The gate matrix for this operation, expressed in the computational basis {00,01,10,11} where the left index indicates the

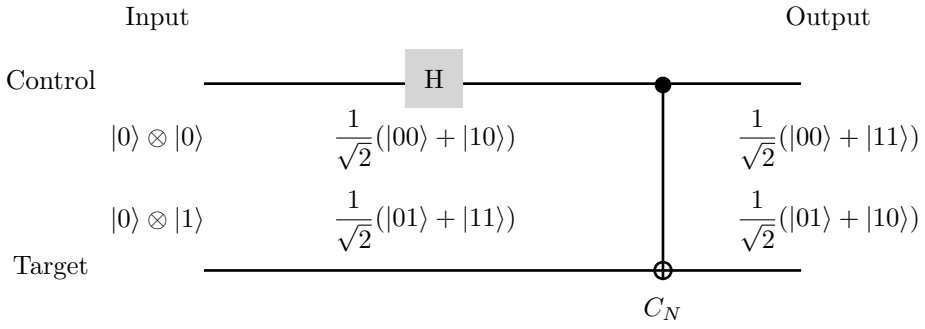

Figure 2.2: Creation of maximally entangled Bell states using a Hadamard and C_N gate, depending on input state all four entangled Bell states can be created using only two gates.

control qubit is given by

$$U_{C_N} = \begin{pmatrix} 1 & 0 & 0 & 0 \\ 0 & 1 & 0 & 0 \\ 0 & 0 & 0 & 1 \\ 0 & 0 & 1 & 0 \end{pmatrix}. \tag{2.8}$$

From this one can see that the action of the C_N gate upon the target is entirely dependent upon the state of the control; if the control is in state $|0\rangle$ the target qubit remains unchanged however if the control is in state $|1\rangle$ the target qubit undergoes a bit-flip. Applying a Hadamard gate to the control qubit before implementing the C_N gate, as shown in Fig. 2.2 can be used to generate any of the four maximally entangled Bell states

$$|\Phi^{\pm}\rangle = \frac{1}{\sqrt{2}}(|00\rangle \pm |11\rangle), \quad |\Psi^{\pm}\rangle = \frac{1}{\sqrt{2}}(|01\rangle \pm |10\rangle), \tag{2.9}$$

providing a platform for deterministic entanglement.

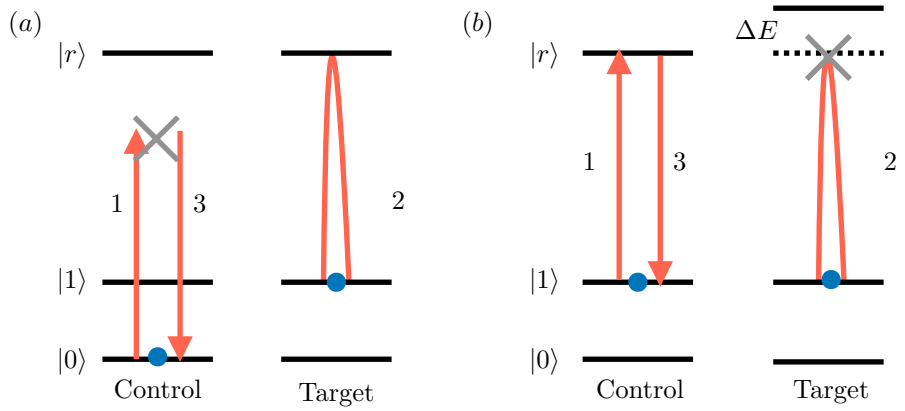

Figure 2.3: Example of a C_Z gate using Rydberg blockade (numbers indicate rotation order) (a) initial state $|01\rangle$, the control atom is not couple to the Rydberg state and the target is able to undergo a full rotation to the Rydberg state and back to $|1\rangle$ accumulating a π phase shift. (b) Initial state $|11\rangle$, the first rotation excites the control atom to Rydberg state which blockades excitation of the target with the second rotation after application of the third rotation the control is returned to $|1\rangle$ and accumulates a π phase shift.

2.3 A Rydberg Quantum Gate

An example of a Rydberg mediated gate is a Controlled-Z (C_Z) or controlled phase gate which is depicted in Fig 2.3 with a pulse sequence. Consider two atoms initially being in the state $|01\rangle$, in this situation the control atom is not coupled to the Rydberg state $|r\rangle$ and the target atom is free to undergo a full rotation to $|r\rangle$ and back to $|1\rangle$ and will accumulate a π phase shift. If the initial two atom state is $|11\rangle$, upon the first pulse the control atom is rotated to the Rydberg state. As the target qubit is within the blockade radius the energy shift from the dipole-dipole interaction blocks excitation so no phase shift is acquired in the target qubit. The third pulse returns the control to $|1\rangle$ and a phase shift accumulated. Thus one can see that for all initial two atom states aside $|00\rangle$ there is a π phase shift accumulated. The evolution

matrix for this gate is given by

$$U_{C_Z} = \begin{pmatrix} 1 & 0 & 0 & 0 \\ 0 & -1 & 0 & 0 \\ 0 & 0 & -1 & 0 \\ 0 & 0 & 0 & -1 \end{pmatrix}, \tag{2.10}$$

which can readily be turned into a C_N gate with a Hadamard rotation on the target atom before and after the C_Z gate [23].

2.4 Summary

A two-level quantum system can be used to provide a qubit basis such as the hyperfine ground states of a neutral alkali atom. Through single and certain two-qubit operations a universal set of quantum gates for computation can be realised. In order to implement two-qubit gates interactions between qubits are typically required, this can be realised through the dipole interactions of Rydberg atoms. Further to this the Rydberg blockade can be used to implement a C-NOT gate which when coupled with a Hadamard rotation can be used to provide on demand ground state entanglement.

Part II

Theory of Atom-Atom and Atom-Light Interactions

Chapter 3

Properties of Rydberg Atoms

The exaggerated properties of Rydberg atoms makes them ideal candidates for neutral atom quantum gates [23]. This chapter summarises some of the fundamental properties of Rydberg atoms and long range Rydberg-Rydberg atom interactions relevant for the work presented in this thesis. A more detailed introduction to Rydberg atoms can be found in [74, 75]

3.1 Alkali Rydberg Atoms

Alkali atoms only have one valence electron and can be described by the Bohr atom picture of an electron orbiting a positive core with a $1/r$ Coulomb potential at long range. The relationship of the binding energy of this electron to the quantum numbers n, orbital angular momentum l and total angular momentum j is given by

$$E_{n,l,j} = -\frac{\mathrm{Ry}}{(n-\delta_{n,l,j})^2}, \tag{3.1}$$

where Ry is the mass-corrected Rydberg constant and $\delta_{n,l,j}$ is the quantum defect. This defect arises for low lying angular momentum states $l \leq 3$ as their orbits penetrate through the electron cloud around the nucleus, thus

Parameter	Value
δ_0	4.04935665
δ_2	0.2377037

Table 3.1: Quantum defects parameters for $nS_{1/2}$ values taken from [79]

the properties of Rydberg states are dependent upon the effective quantum number $n_{\text{eff}} = n - \delta_{n,l,j}$. The quantum defect $\delta_{n,l,j}$ is given by the expansion

$$\delta_{n,l,j} = \delta_0 + \frac{\delta_2}{(n-\delta_0)^2} + \frac{\delta_4}{(n-\delta_0)^4} + ... \quad . \tag{3.2}$$

The quantum defect of low angular momentum states of caesium has been measured thorough precision spectroscopy [76–79]. Values obtained for the $S_{1/2}$ state used for calculations are presented in Table 3.1

3.2 Radial Matrix Elements

Rydberg atoms have a large average orbital radius which scales as $\langle r \rangle \propto n^2 a_0$, where a_0 is the Bohr radius. This gives rise to very large dipole couplings between neighbouring states $|n, l, j, m_j\rangle$ and $|n', l', j', m'_j\rangle$ where $l' = l \pm 1$ as there is strong overlap between the wavefunctions and large electric dipole moment $\boldsymbol{\mu} = -e\boldsymbol{r}$. The dipole matrix element is given by $\langle n, l, j, m_j|\boldsymbol{\mu}|n', l', j', m'_j\rangle$, and by using the Alkali Rydberg Calculator (ARC) [75] the matrix element between $69S_{1/2}$ and $69P_{3/2}$ is found to be $\sim 2800\ ea_0$. For comparison the ground state coupling between $6S_{1/2}$ and $6P_{3/2}$ is $\sim 3\ ea_0$, highlighting the much enhanced interaction strengths of Rydberg states.

3.3 Rydberg State Lifetimes

Another feature of Rydberg atoms that make them ideal for quantum gates is their relatively long lifetime which can be on the order of hundreds of

Parameter	Value
n_{eff}	64.951
τ_{s}	1.293
α	3.001
A	0.123
B	7.295 $\times 10^4$
C	2.517
D	4.375
$69S_{1/2}$ τ_{eff}(300 K)	134 μs
$69S_{1/2}$ τ_{eff}(4 K)	349 μs

Table 3.2: Parameters used in Rydberg state lifetime calculations constants are taken from [80]

μs. This lifetime is dependent upon not only radiative decay rate due to spontaneous emission Γ_0, but also due to transitions to near lying Rydberg states induced via black-body radiation Γ_{BBR}. The summation of these two decay rates presents the effective lifetime [80]

$$\frac{1}{\tau_{\text{eff}}} = \Gamma_0 + \Gamma_{\text{BBR}}. \tag{3.3}$$

The radiative decay can be calculated from the Einstein-A coefficient $\mathcal{A}(nl \rightarrow n'l')$ and summation over all the possible decay pathways for $E_{nl} > E_{n'l'}$. Black-body induced transitions, however, can result in transition to higher lying states and are highly dependent upon the temperature and transition frequency. Numerical calculations have been performed calculating these decays to extrapolate a semi-empirical form for alkali-Rydberg state lifetimes [80],

$$\tau_{\text{eff}} = \left(\frac{1}{\tau_{\text{s}} n_{\text{eff}}^{\alpha}} + \frac{A}{n_{\text{eff}}^{D}} \frac{21.4}{\exp(B/n_{\text{eff}}^{C} T) - 1} \right)^{-1} \text{(ns)}. \tag{3.4}$$

This thesis explores excitation to the Rydberg state $69S_{1/2}$ the relevant constants for the above expression regarding this state state are shown in Table 3.2. Computing the above relation using these parameters gives a room temperature lifetime of $\tau_{\text{eff}}(300\text{ K}) = 134$ μs. The importance of considering

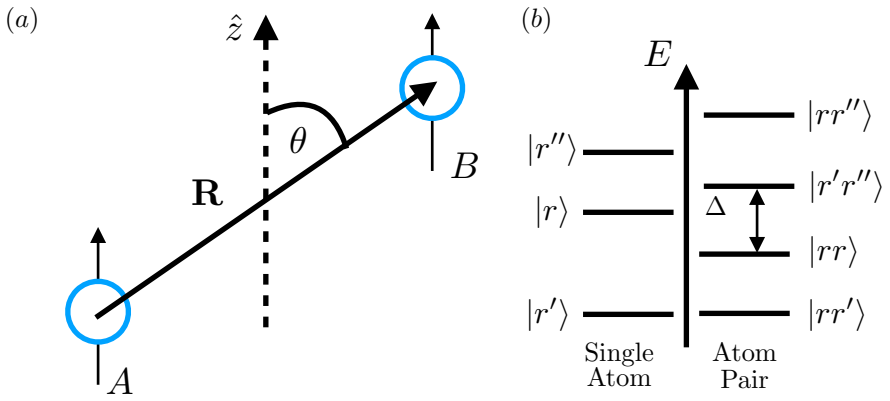

Figure 3.1: (a) Two Rydberg atoms with dipoles $\boldsymbol{\mu}_A$ and $\boldsymbol{\mu}_B$ separated by $\boldsymbol{R}$ with an angle θ. (b) Single atom basis compared to the two atom pair-state basis. The predominant dipole-dipole interaction channel is between $|rr\rangle$ and $|r'r''\rangle$, where the energy defect Δ is small.

black-body induced transitions is clearly illustrated when comparing to the lifetime at 4 K $\tau_{\text{eff}}(4\text{ K}) = 349$ μs demonstrating a significant contrast in the expected Rydberg lifetimes. However these times still far exceed the excited state lifetime of the D_2 line in caesium of $\tau = 30$ ns [81] presenting the ability to perform experiments on much longer timescales on Rydberg states compared to lower lying states.

3.4 Dipole-Dipole Interactions

The Rydberg blockade arises when the Rydberg-Rabi coupling is much smaller than the Rydberg-Rydberg interaction occurring between two closely separated atoms. First however we must examine the dipole-dipole interaction which leads to this. Consider two atoms, A and B, in the Rydberg state $|r\rangle$ separated by a distance $\mathbf{R}$ as depicted in Fig. 3.1(a), with dipole moments $\boldsymbol{\mu}_A$ and $\boldsymbol{\mu}_B$ for transitions to adjacent Rydberg states $|r'\rangle$ and $|r''\rangle$ respectively. Each atom has a radiating electric dipole field arising from the oscillating dipole which in turn can interact with with the other atom and exchange a virtual photon. This interaction energy in atomic units is given

by [82]

$$V_{dd}(R) = \frac{\boldsymbol{\mu}_A \cdot \boldsymbol{\mu}_B - 3(\boldsymbol{\mu}_A \cdot \boldsymbol{n})(\boldsymbol{\mu}_B \cdot \boldsymbol{n})}{R^3}, \tag{3.5}$$

where $\boldsymbol{n}$ is a unit vector pointing in the direction of $\boldsymbol{R}$. This can be rewritten in a spherical basis using $\boldsymbol{n} = \sin\theta\boldsymbol{\epsilon}_x + \cos\theta\boldsymbol{\epsilon}_y$ to obtain the dipole operators μ_q, which are given by

$$\mu_{-1} = \frac{1}{\sqrt{2}}(\hat{\mu}_x - i\hat{\mu}_y), \tag{3.6}$$

$$\mu_0 = \mu_z, \tag{3.7}$$

$$\mu_{+1} = \frac{1}{\sqrt{2}}(\hat{\mu}_x + i\hat{\mu}_y), \tag{3.8}$$

where $\hat{\mu} = -e\boldsymbol{r} \cdot \boldsymbol{\epsilon}$ and $\boldsymbol{\epsilon}$ is the polarisation unit vector. These operators govern the possible change in magnetic quantum number with μ_0 conserving such that $\Delta m_j = 0$ and μ_{+1} or μ_{-1} allowing $\Delta m_j = -1$ and $\Delta m_j = +1$ respectively. Now $V_{dd}(R)$ can be rewritten as [83]

$$\begin{aligned} V_{dd}(R) = \frac{1}{R^3}[&\mathcal{A}_1(\theta)(\mu_{A,-1}\mu_{B,+1} + \mu_{A,+1}\mu_{B,-1} + 2\mu_{A,0}\mu_{B,0}) \\ &+ \mathcal{A}_2(\theta)(\mu_{A,-1}\mu_{B,0} - \mu_{A,+1}\mu_{B,0} + \mu_{A,0}\mu_{B,-1} - \mu_{A,0}\mu_{B,+1}) \\ &- \mathcal{A}_3(\theta)(\mu_{A,-1}\mu_{B,-1} + \mu_{A,+1}\mu_{B,+1})], \end{aligned} \tag{3.9}$$

where $\mu_{i,q}$ corresponds to the atom number $i = \{A, B\}$ and $q = \{-1, 0, 1\}$ the respective dipole operator. The angular pre-factors in the above relation are $\mathcal{A}_1(\theta) = 1 - 3\cos^2\theta/2$, $\mathcal{A}_2(\theta) = 3\sin\theta\cos\theta/\sqrt{2}$ and $\mathcal{A}_3(\theta) = 3\sin^2\theta/2$, and dictate the total change in magnetic quantum number $M = m_{jA} + m_{jB}$ from the dipole interaction which are $\Delta M_j = 0$, $\Delta M_j = 1$ and $\Delta M_j = 2$ for the respective pre-factors. Therefore, one can see that an angular dependence arises for the interaction strength.

Understanding the energy shift that arises from this interaction requires moving from a single atom basis to pair-states where the two atom state is expressed as $|\psi_A\psi_B\rangle$. The energies of these pair-states are simply the ad-

dition of the single atom energies such that $E_{|rr'\rangle} = E_r + E_{r'}$. Strong dipole interactions occur between pair-states where the energy difference between the pair-states is small; consider the states shown in Fig. 3.1(b): there is a dipole-dipole interaction between the initial state $|rr\rangle$ and $|r'r''\rangle$ from which an energy defect arises

$$\Delta = E_{|r'r''\rangle} - E_{|rr\rangle}. \tag{3.10}$$

Considering this to be the predominant interaction channel the Hamiltonian of the system is given by

$$\mathcal{H} = \begin{pmatrix} 0 & V_{dd}(R) \\ V_{dd}(R) & \Delta \end{pmatrix}, \tag{3.11}$$

which can then be diagonalised to obtain the eigenvalues

$$\lambda_{\pm} = \frac{\Delta \pm \sqrt{\Delta^2 + 4V_{dd}(R)^2}}{2}. \tag{3.12}$$

The above relation now depicts the pair state energy in terms of the separation between the two atoms. Two interesting limits arise from this [74]:

- $V_{dd}(R) \gg \Delta$: this limit is known as the short range resonant dipole-dipole regime, where there are attractive and repulsive potentials which result in a energy shift related to atomic separation. The strength of this interaction is given by

$$\Delta E = \pm V_{dd}(R) = \pm \frac{C_3}{R^3}, \tag{3.13}$$

  in this regime the interaction is dependent upon the atom separation with a $1/R^3$ asymptote and the dispersion coefficient C_3 which scales as n_{eff}^4. Electric fields can be used to manipulate pair-state energies to reduce the energy defect to operate in this resonant regime [83].

- $V_{dd}(R) \ll \Delta$: this limit is known as the long range Van der Waals

regime where the interaction scales as

$$\Delta E = \frac{|V_{dd}(R)|^2}{\Delta} = -\frac{C_6}{R^6}. \tag{3.14}$$

In this regime the interaction is dependent upon the atom separation with a $1/R^6$ asymptote and the dispersion coefficient C_6 scales as n_{eff}^{11}. Of noticeable difference from the other interaction regime is that the sign of the shift is now entirely dependent upon the energy defect.

The crossover between these regimes is known as the van der Waals radius and occurs when $V_{dd}(R) = \Delta$. Substituting into Eq. 3.14 and rearranging one obtains $R_{\text{vdW}} = \sqrt[6]{C_6/\Delta}$. For the excitation considered in this experiment the dominant interaction occurs from $|69S_{1/2}69S_{1/2}\rangle \leftrightarrow |68P_{3/2}69P_{3/2}\rangle$ where the energy defect at infinite separation is $\Delta/2\pi = 0.75$ GHz. The C_6 coefficient can be computed from the Alkali Rydberg Calculator (ARC) [75] giving $C_6 = 573$ GHz·μm^6. Using these values gives a van der Waals radius of $R_{\text{vdW}} = 3$ μm. For the experiment presented in this thesis the separation of the atoms is $R > 5$ μm, hence interactions presented in this work occur in the long range van der Waals regime. In this regime for the S states considered the angular variation in dipole interaction strength is strongly suppressed due to the spherical charge distribution of the l=0 state, whilst higher angular momentum states are highly anisotropic.

3.5 Rydberg Blockade

Now that the mechanisms behind the van der Waals energy shift have been explained, we will consider two atoms in close proximity to each other addressed by equal coupling fields Ω to the Rydberg state $|r\rangle$ as shown in Fig. 3.2. As discussed in the previous section a position dependent energy shift arises due to strong dipole-dipole interactions between the atoms; con-

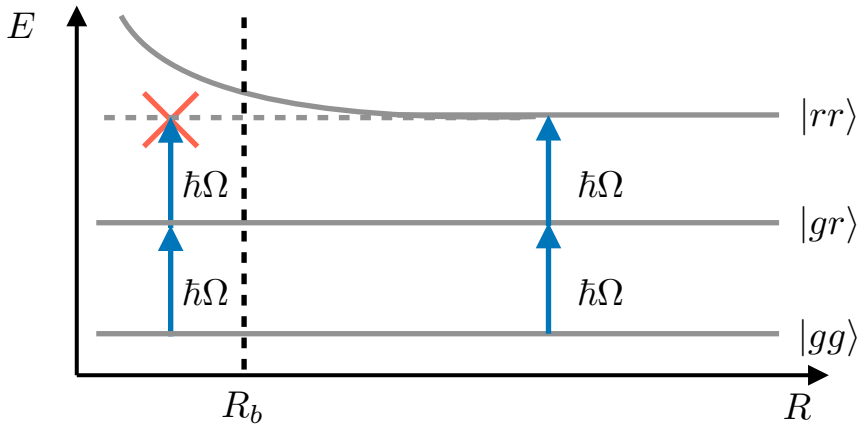

Figure 3.2: Energy shift between two closely separated atoms, when blockade conditions are met excitation to the doubly excited state $|rr\rangle$is inhibited.

sider the case where one atom is excited to $|r\rangle$. The energy required for the other atom to also be excited to $|r\rangle$ is now dependent on its proximity to the original atom. When far apart the energy shift is negligible and it can be excited to the Rydberg state, conversely when the energy shift is greater than coupling field $\Delta E \gg \hbar\Omega$ excitation of the second atom to the Rydberg state $|rr\rangle$ is inhibited. This phenomenon is known as the Rydberg blockade and occurs when both atoms are within what is known as the blockade radius which is given by

$$R_b = \sqrt[6]{\frac{|C_6|}{\Omega}}, \tag{3.15}$$

which scales as $n_{\text{eff}}^{1.83}$. To see this effect it is imperative to use a high principal quantum number. For example the radius for a $\Omega/2\pi$ =1 MHz coupling field to $40S_{1/2}$ is $R_b \sim 3$ μm which in the context of quantum information is experimentally challenging to implement as it is desirable to have single site addressability with minimal cross-talk, which would require sub-μm addressing beams. In comparison for $69S_{1/2}$ one obtains $R_b = 9.1$ μm which is easily achieved and offers scalability to large arrays.

Further to the suppression of the doubly excited state $|rr\rangle$, the Rydberg blockade offers a route to the creation of an entangled symmetric state. Consider the two atoms separated by a small enough distance that block-

ade conditions are met ($R < R_b$). When the coupling field Ω to the Rydberg state is applied both atoms are equally likely to be excited to the Rydberg state creating a superposition where one or the other can be in the Rydberg state

$$|\mathcal{W}\rangle = \frac{1}{\sqrt{2}}(|rg\rangle + |gr\rangle). \tag{3.16}$$

The coupling to the entangled symmetric state exhibits a $\sqrt{2}\Omega$ enhancement [46] in the Rabi frequency compared to the single atom case. This extends to N atoms where the coupling is $\sqrt{N}\Omega$. Evidence of this enhanced coupling has been observed in several experiments [55, 60, 63] and represents strong evidence of Rydberg entanglement.

3.6 Summary

Rydberg atoms offer the potential to explore long range interactions through strong dipole-dipole couplings in addition to state lifetimes exceeding $\tau > 100$ μs, making them ideal candidates for implementing quantum operations of two or more qubits [23]. Further to this the Rydberg blockade offers a route to the generation of entanglement between neutral atoms [60, 63].

Chapter 4

Two-Photon Raman Transitions for Qubit Rotations

This thesis research requires tools providing excitation to Rydberg states and rotations between the hyperfine ground states. As the single photon electric dipole matrix elements between the ground and Rydberg states are weak and would require larges amounts of UV power it is less challenging to use two-photon transitions. This also presents the opportunity to orientate excitation into an almost Doppler free configuration. Similarly transitions between the hyperfine ground states have weak magnetic dipole matrix elements therefore access to fast operations also requires two-photon transitions. The two relevant level schemes are depicted in Fig. 4.1 with Rydberg excitation using a ladder configuration and the ground state rotations using a lambda scheme. Both systems navigate to the desired state via an intermediate excited state $|e\rangle$ which has a short radiative lifetime, coherent operation in both setups requires working at a large detuning Δ to minimise spontaneous emission. The physics behind both transitions is relatively similar therefore this chapter will only consider the ladder scheme in depth and summarise the results of the lambda scheme.

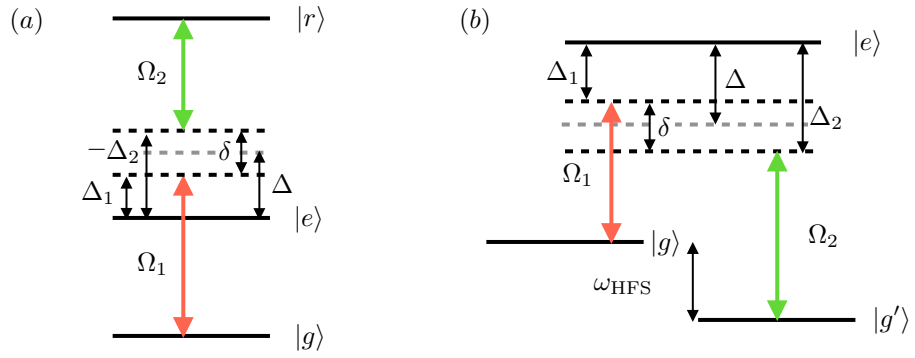

Figure 4.1: Raman transition schemes used in this experiment (a) ladder system and (b) lambda system.

4.1 Three-level Ladder System

We consider a three-level ladder system as shown in Fig. 4.1 with states $|g\rangle, |e\rangle$ and $|r\rangle$. They are addressed by two monochromatic light fields at frequency ω_1 and ω_2 coupling to $|g\rangle \rightarrow |e\rangle$ and $|e\rangle \rightarrow |r\rangle$ respectively. The relative detuning of each field is $\Delta_1 = \omega_1 - (\omega_e - \omega_g)$ and $\Delta_2 = \omega_2 - (\omega_r - \omega_e)$. The Hamiltonian for the system is given by $\mathcal{H} = \mathcal{H}_0 + \mathcal{H}_{al}$ where the bare Hamiltonian is

$$\mathcal{H}_0 = \hbar\omega_g|g\rangle\langle g| + \hbar\omega_e|e\rangle\langle e| + \hbar\omega_r|r\rangle\langle r|, \tag{4.1}$$

and the atom-light interaction can be expressed as an oscillating electric dipole perturbation given by $\mathcal{H}_{al} = -\hat{\boldsymbol{\mu}} \cdot \boldsymbol{\mathcal{E}}$ where the electric field is a plane wave and under the dipole approximation is given by $\boldsymbol{\mathcal{E}} = \boldsymbol{\epsilon}(\mathcal{E}_0 e^{-i\omega t}/2 + c.c.)$. Under the rotating wave approximation [84] this atom light interaction is given by

$$\mathcal{H}_{al} = \frac{\hbar\Omega_1}{2}(e^{-i\omega_1 t}|e\rangle\langle g| + e^{i\omega_1 t}|g\rangle\langle e|) + \frac{\hbar\Omega_2}{2}(e^{i\omega_2 t}|e\rangle\langle r| + e^{-i\omega_2 t}|r\rangle\langle e|), \tag{4.2}$$

where we have introduced the Rabi frequency which for electric dipole transitions is given by

$$\Omega = \frac{-\hat{\boldsymbol{\mu}} \cdot \boldsymbol{\mathcal{E}}}{\hbar} = \frac{\mathcal{E}_0}{\hbar}\langle i|e\boldsymbol{r} \cdot \boldsymbol{\epsilon}|j\rangle. \tag{4.3}$$

The two coupling fields thus equate to $\Omega_1 = \boldsymbol{d}_{eg}\mathcal{E}_{0,1}/\hbar$ and $\Omega_2 = \boldsymbol{d}_{er}\mathcal{E}_{0,2}/\hbar$, where $\boldsymbol{d}_{ij} = \langle i|e\boldsymbol{r}\cdot\boldsymbol{\epsilon}|j\rangle$ is the dipole matrix element for a transition from $|i\rangle$ to $|j\rangle$. In the basis where the states are represented by normalised orthogonal column vectors given by

$$|g\rangle = \begin{pmatrix} 1 \\ 0 \\ 0 \end{pmatrix}, \quad |e\rangle = \begin{pmatrix} 0 \\ 1 \\ 0 \end{pmatrix}, \quad |r\rangle = \begin{pmatrix} 0 \\ 0 \\ 1 \end{pmatrix}, \tag{4.4}$$

this results in a Hamiltonian matrix of the form

$$\mathcal{H}_\Xi = \frac{\hbar}{2}\begin{pmatrix} 2\omega_g & \Omega_1 e^{i\omega_1 t} & 0 \\ \Omega_1 e^{-i\omega_1 t} & 2\omega_e & \Omega_2 e^{i\omega_2 t} \\ 0 & \Omega_2 e^{-i\omega_2 t} & 2\omega_r \end{pmatrix}. \tag{4.5}$$

This can then be inserted into the time dependent Schrödinger equation

$$i\hbar\partial|\psi\rangle/\partial t = \mathcal{H}|\psi\rangle, \tag{4.6}$$

for the amplitudes c_i of the wave function $|\psi(t)\rangle = c_g(t)|g\rangle + c_e(t)|e\rangle + c_r(t)|r\rangle$ to obtain three coupled differential equations

$$\dot{c}_g = -i\omega_g c_g - \frac{i\Omega_1}{2}e^{i\omega_1 t}c_e, \tag{4.7}$$

$$\dot{c}_e = -\frac{i\Omega_1}{2}e^{-i\omega_1 t}c_g - i\omega_e c_e - \frac{i\Omega_2}{2}e^{i\omega_2 t}c_r, \tag{4.8}$$

$$\dot{c}_r = -\frac{i\Omega_2}{2}e^{-i\omega_2 t}c_e - i\omega_r c_r. \tag{4.9}$$

This expression can then be rotated into the frame of averaged frequencies using the following transformations: $c_g(t) = c'_g(t)e^{-i(-\delta/2+\omega_g)t}$, $c_e(t) =$

$c'_e(t)e^{-i(-\delta/2+\omega_g+\omega_1)t}$ and $c_r(t) = c'_r(t)e^{-i(-\delta/2+\omega_g+\omega_1+\omega_2)t}$ [85] where $\delta = \Delta_1 + \Delta_2$ and $\Delta = (\Delta_1 - \Delta_2)/2$ giving

$$\dot{c}'_g = -i\delta/2c'_g - \frac{i\Omega_1}{2}c'_e, \tag{4.10}$$

$$\dot{c}'_e = -\frac{i\Omega_1}{2}c'_g + i\Delta c'_e - \frac{i\Omega_2}{2}c'_r, \tag{4.11}$$

$$\dot{c}'_r = -\frac{i\Omega_2}{2}c'_e + \frac{i\delta}{2}c'_r. \tag{4.12}$$

These expressions can then be used to obtain the effective Hamiltonian in the rotating frame of the form

$$\mathcal{H}_\Xi = \frac{\hbar}{2}\begin{pmatrix} \delta & \Omega_1 & 0 \\ \Omega_1 & -2\Delta & \Omega_2 \\ 0 & \Omega_2 & -\delta \end{pmatrix}. \tag{4.13}$$

Adiabatic Elimination

To minimise spontaneous emission from the intermediate state it is desirable to operate at large a detuning relative to $|e\rangle$. In the regime where the coupling is much smaller than this detuning $\Omega_{1,2} < |\Delta_{1,2}|$ it can be assumed that the population of c'_e is stationary, therefore it can be assumed that $\dot{c}'_e = 0$. Rearranging Eq. 4.8 for $\dot{c}'_e = 0$ gives

$$c'_e = \frac{\Omega_1 c'_g + \Omega_2 c'_r}{2\Delta}. \tag{4.14}$$

Inserting this back into the amplitude equations gives

$$\dot{c}'_g = -i(\delta/2 + \frac{|\Omega_1|^2}{4\Delta})c'_g - i\frac{\Omega_1\Omega_2}{4\Delta}c'_r, \tag{4.15}$$

$$\dot{c}'_r = -i\frac{\Omega_1\Omega_2}{4\Delta}c'_g + i(\delta/2 - \frac{|\Omega_2|^2}{4\Delta})c'_r, \tag{4.16}$$

where the intermediate state has now been eliminated and the three level system is now represented by an effective two-level system with Rabi frequency

$$\Omega_R = \frac{\Omega_1 \Omega_2}{2\Delta}, \tag{4.17}$$

and AC Stark shift terms

$$\Delta^g_{AC} = \frac{|\Omega_1|^2}{4\Delta}, \quad \Delta^r_{AC} = \frac{|\Omega_2|^2}{4\Delta}, \tag{4.18}$$

for the states $|g\rangle$ and $|r\rangle$ respectively.

Making the transformation $c'_{g,r} = c''_{g,r} e^{-i(\Delta_{\text{eff}}/2 - \delta/2 + \Delta^r_{AC})t}$, and introducing $\Delta_{eff} = \delta + \Delta^g_{AC} + \Delta^r_{AC}$ reduces this to the form

$$\dot{c}''_g = -i\Delta_{eff}/2 c''_g - i\Omega_R/2 c''_r, \tag{4.19}$$

$$\dot{c}''_r = -i\Omega_R/2 c''_g + i\Delta_{eff}/2 c''_r, \tag{4.20}$$

with a corresponding effective two-level Hamiltonian

$$\mathcal{H}^{eff}_{\Xi} = \frac{\hbar}{2} \begin{pmatrix} \Delta_{eff} & \Omega_R \\ \Omega_R & -\Delta_{eff} \end{pmatrix}. \tag{4.21}$$

This Hamiltonian is equivalent to that for the well known expression for Rabi oscillations in a simple two-level system [84]. Conditions for perfect transfer requires $\Delta_{eff} = 0$, however due to the the AC stark shifts arising from the the excitations fields this does not correspond to $\Delta_1 = -\Delta_2$ and resonance is found when $\delta = -(\Delta^g_{AC} + \Delta^r_{AC})$ is satisfied. Conditioning the initial populations to $c''_g(0) = 1$ ($c''_r(0) = 0$) and rearranging Eq. 4.19 and 4.20 shows that the Rydberg state population evolves as

$$|c_r(t)|^2 = \frac{\Omega_R^2}{\tilde{\Omega}^2} \sin^2(\frac{\tilde{\Omega} t}{2}), \tag{4.22}$$

where $\tilde{\Omega}$ is the effective Rabi frequency given by $\tilde{\Omega}^2 = \Omega_R^2 + \delta^2$. From this

relation we see that on resonance i.e $\tilde{\Omega} = \Omega$ a pulse area of $\Omega t = \pi$ results in a complete transfer to the upper state, this is known as a π-rotation and can be used to implement an X-Gate. Fig. 4.2 shows the evolution of the upper state population over time in what are known as Rabi oscillations as the population coherently evolves between the ground and Rydberg states. Also depicted in the figure is the numerical solution to this evolution using the time dependent Schrödinger equation with the effective two-level Hamiltonian derived in Eq. 4.21 showing good agreement with the analytical expression. However due to dissipative effects such as spontaneous emission the oscillation can begin to decohere and become damped as shown by the red data in Fig. 4.2 where an exaggerated damping due to spontaneous emission from the upper state has been included using the Optical Bloch Equations (OBEs). Inclusion of such dissipative effects is found to have an analytical expression given by [86, 87]

$$P_r(t) = \frac{\Omega_R^2}{2\Omega_R^2 + (1/\tau)^2}\left[1 - e^{-3t/4\tau}\left(\cos(\tilde{\Omega}'t) + \frac{3}{4\tau\tilde{\Omega}'}\sin(\tilde{\Omega}'t)\right)\right], \quad (4.23)$$

where τ is a damping constant and $\tilde{\Omega}' = \sqrt{\Omega_r + 1/(16\tau^2)}$. The evolution of this expression is also shown in Fig. 4.2 and is in good agreement with the numerical representation. As previously stated a source of such a dissipative effect is spontaneous emission from the intermediate state, the probability this occurring over a π-rotation is given by $P_{\text{sc}} = \int_0^\pi |c_e'(t)|^2 \, \mathrm{d}t$ when $c_g' = \cos(\Omega_r t/2)$ and $c_r' = \sin(\Omega_r t/2)$ which yeilds

$$P_{\text{sc}} = \Gamma_e \frac{1}{\Omega_R}\left(\frac{\Omega_1^2}{8\Delta^2} + \frac{\Omega_2^2}{8\Delta^2}\right). \quad (4.24)$$

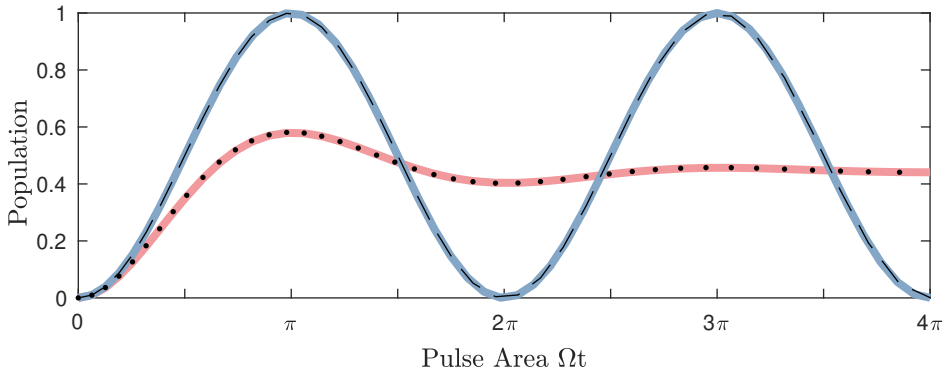

Figure 4.2: Evolution of the upper state population as a function of time by numerically solving the time dependent Schrödinger equation for the effective two-level Hamiltonian (blue line), dashed line represents evolution using Eq. 4.22 and evolution numerically solving the OBE's (red line) to include dissipative effects with the dotted line representing Eq. 4.23

4.2 Lambda System

The derivation above can also be used to find the Hamiltonian of the lambda system shown in Fig. 4.1(b) with some minor changes. The major difference between the systems is the redefinition of Δ_2 which is now $\tilde{\Delta}_2 = \omega_2 - (\omega_e - \omega_{g'})$, Δ_1 remains the same. This results in the same Hamiltonian as expressed in Eq. 4.13 with $\delta = \Delta_1 - \tilde{\Delta}_2$ and $\Delta = (\Delta_1 + \tilde{\Delta}_2)/2$. Another important difference between the two systems not considered in this expression is the light shift from the field upon the state it is not coupled to. In the ladder system this effect is negligible as states $|g\rangle$ and $|r\rangle$ are well separated. However in the case of the lambda system the separation can be small therefore there will be a light shift upon $|g\rangle(|g'\rangle)$ associated with the coupling Ω_2 (Ω_1). In the case of this experiment the splitting between the states $|g\rangle$ and $|g'\rangle$ corresponds to the hyperfine splitting of the ground state of caesium ω_{HFS}, such that the ground state AC stark shifts are given by

$$\Delta^{g}_{AC} = \frac{|\Omega_1|^2}{4\Delta} + \frac{|\Omega_2|^2}{4(\Delta - \omega_{\mathrm{HFS}})}, \tag{4.25}$$

$$\Delta^{g'}_{AC} = \frac{|\Omega_1|^2}{4(\Delta + \omega_{\mathrm{HFS}})} + \frac{|\Omega_2|^2}{4\Delta}, \tag{4.26}$$

highlighting the extra caution required when considering a lambda system.

4.3 Rabi Frequencies

Recalling that the Rabi coupling for a dipole transition between $|i\rangle$ and $|j\rangle$ is given by $\Omega = \boldsymbol{d}_{ij} \cdot \mathcal{E}/\hbar$ where $\boldsymbol{d} = \langle i|e\boldsymbol{r} \cdot \boldsymbol{\epsilon}|j\rangle$ is the dipole matrix element. Using Wigner-Eckart theorem the dipole matrix element can be calculated from the product of a reduced matrix element and a Wigner 3-j symbol [88] such that in the hyperfine basis the Rabi frequency is now given by

$$\Omega_{f,m_f \to f',m'_f} = \frac{\mathcal{E}}{\hbar}(-1)^{f-m_f} \begin{pmatrix} f & 1 & f' \\ -m_f & q & m'_f \end{pmatrix} \langle n'l'j'f'||er||nljf\rangle, \tag{4.27}$$

where $q = -1, 0, 1$ is the lasers polarisation corresponding to the transitions shown in Eq. 3.6-3.8. The term within the rounded brackets is the Wigner 3j symbol and vanishes if $m'_f \neq m_f - q$. The reduced matrix element $\langle n'l'j'f'||e\hat{r}||nljf\rangle$ can be decomposed into a Wigner 6-j symbol and another reduced matrix element dependent only upon the fine structure basis [88].

$$\begin{aligned}\langle n'l'j'f'||er||nljf\rangle = (-1)^{j+I+f'+1}\sqrt{(2f+1)(2f'+1)} \\ \times \begin{Bmatrix} f & 1 & f' \\ j' & I & j \end{Bmatrix} \langle n'l'j'||er||nlj\rangle,\end{aligned} \tag{4.28}$$

where the term in the curly brackets is the Wigner 6j symbol, the reduced matrix element can now be calculated from the Einstein A coefficient

$$\mathcal{A}(nlj \to nl'j') = \frac{\omega_0^3}{2\pi\epsilon_0\hbar c^3}\frac{|\langle n'l'j'||er||nlj\rangle|^2}{2j'+1}, \tag{4.29}$$

For the transitions considered in this work the via the intermediate state $|e\rangle = 6P_{3/2}$ the reduced matrix element is found to be $\langle J = 3/2||e\boldsymbol{r} \cdot \boldsymbol{\epsilon}||J = 1/2\rangle = 4.4786ea_0$ [81]. However due to the unresolved hyperfine structure of the

Rydberg state $|j', m'_j\rangle$ coupling from the intermediate state $|f, m_f\rangle$ requires decomposing $|j'I'\rangle$ into $|f', m'_f\rangle$

$$|j'I; m'_j m_i\rangle = \sum_{f', m'_f} C^{fm'_f}_{j'm'_j Im_I} |j'I; f'm'_f\rangle, \tag{4.30}$$

where $C^{fm'_f}_{j'm'_j Im_I}$ is the Clebsh-Gordon coefficient which is given by

$$C^{fm'_f}_{j'm'_j Im_I} = (-1)^{j'-I+m'_f} \sqrt{2f+1} \begin{pmatrix} j' & I & f \\ m'_j & m_I & -m'_f \end{pmatrix}. \tag{4.31}$$

Finally combing these relations and introducing angular momentum selection rules $m'_f = m_f - q$ and $m_I = m_f - q - m'_j$ the coupling between the intermediate state and Rydberg state is given by a summation over the excited Rydberg f' states

$$\begin{aligned} \Omega_{f,m_f \to j', m'_j} = \frac{\mathcal{E}}{\hbar} \sum_{f'} C^{f'(m_f - q)}_{j'm'_j I(m_f - q - m'_j)} (-1)^{f - m_f + j + I + f' + 1} \sqrt{(2f+1)(2f'+1)} \\ \times \begin{pmatrix} f & 1 & f' \\ -m_f & q & m'_f \end{pmatrix} \begin{Bmatrix} f & 1 & f' \\ j' & I & j \end{Bmatrix} \langle n'\ell' j' || er || n\ell j \rangle. \end{aligned} \tag{4.32}$$

4.3.1 Multi-level Atoms

The previous relations can now be used to calculate two-photon Rabi frequencies, Stark shifts and scattering probabilities, however the hyperfine splitting of the intermediate state must be accounted for. This is done through summing over all dipole allowed excitation pathways via the intermediate state f_e, such that the two photon Rabi frequency is given by

$$\Omega_R = \sum_{fe} \frac{\Omega_{f,m_f \to f', m'_f} \Omega_{f', m'_f \to j, m_j}}{2(\Delta + \Delta_{f_e})}, \tag{4.33}$$

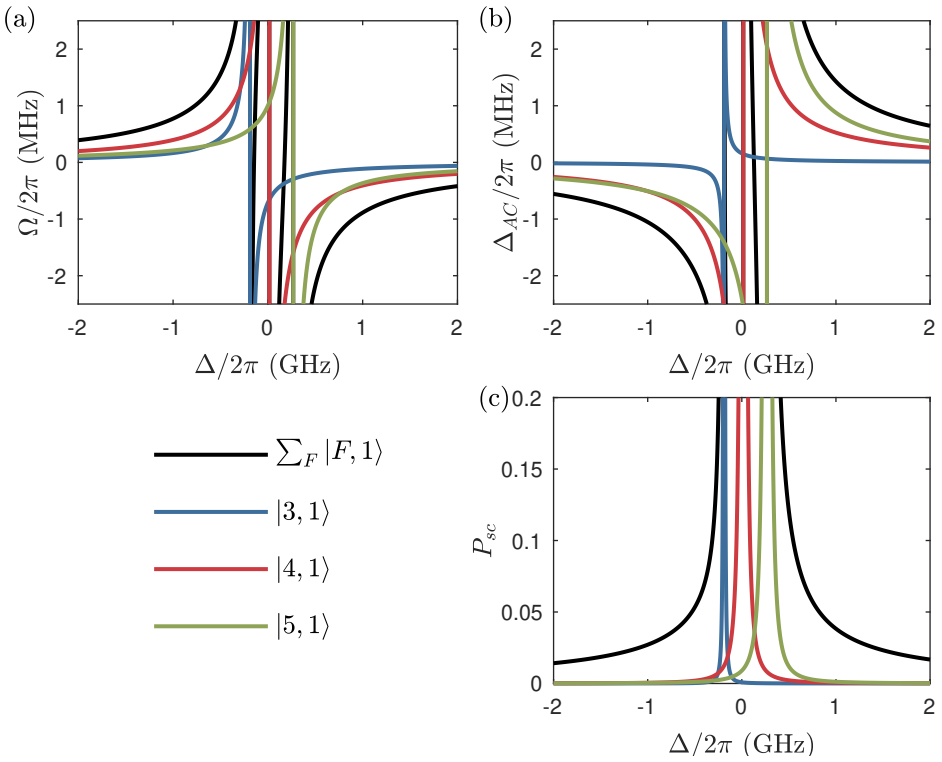

Figure 4.3: Calculation of the two-photon (a) Rabi Frequency (b) AC stark shift and (c) scattering probability as a function of detuning from the intermediate state. Transition is from the clock state of caesium $|4,0\rangle \rightarrow |69S_{1/2}, m_j = 1/2\rangle$ for a $\sigma^+\sigma^-$ transition. The different contributing hyperfine levels are shown as well as the summation in black.

where Δ_{fe} is the relevant hyperfine levels detuning from the centre of mass of the intermediate state. Fig. 4.3(a) shows the calculated Rabi frequency as a function of detuning from the intermediate state for a two photon transition from the clock state of caesium $|4,0\rangle \rightarrow |69S_{1/2}, m_j = 1/2\rangle$ with the first photon being σ^+ polarised coupling to $|3,1\rangle, |4,1\rangle$ and $|5,1\rangle$ and the second photon being σ^-. This is similarly done for the Stark shift and scattering probability as shown in Fig. 4.3(b) and (c). The calculation uses parameters similar to those accessible within the laboratory using powers of 2 μW and 90 mW with waists of 14 μm and 18 μm for the first and second photon respectively. What is further highlighted from these calculations is the necessity to work at a large detuning to minimise scattering on the intermediate level, with less than $\sim$ 800 MHz being susceptible to high scattering probabilities,

Parameter	Value
$\Delta/2\pi$	+1.13 GHz
$\lvert\Omega_R/2\pi\rvert$	0.77 MHz
Δ_{AC}	+1.23 MHz
P_{sc}	0.03

Table 4.1: Calculated two-photon properties for a detuning of $\Delta/2\pi = +1.13$ GHz from the centre of $6P_{3/2}$

however relatively fast Rabi frequencies are still accessible below this. Table 4.1 summaries the expected results for a detuning of $\Delta/2\pi = +1.13$ GHz from the centre of $6P_{3/2}$ as will be later experimentally implemented in Chapter 8.

4.4 Summary

Two-photon transitions allow fast optical rotations to be performed to the Rydberg state with relatively modest power requirements compared to single photon transitions, as well as the possibility to implement almost Doppler free configurations. Similarly two photon transitions overcome the weak magnetic dipole transition for ground state rotations. Implementing these transitions requires operating at a large detuning from an intermediate state, in the case of this experiment $6P_{3/2}$, to reduce scattering events from the intermediate level. Calculation of couplings between states requires summation over all possible excitation pathways via $6P_{3/2}$ and estimated parameters have been obtained for Rydberg excitation.

Part III

The Experiment

Chapter 5

Experimental Setup

This chapter provides an overview of the experimental setup from the initial dual chamber design to optical transport between the chambers.

5.1 Vacuum Chamber

The foundation of any cold atom experiment is the vacuum chamber providing ultra high vacuum (UHV) pressures (10^{-9}-10^{-12} mbar) and the necessary optical access. The key to a successful experiment is thorough planning of this important piece of apparatus.

5.1.1 Experimental Considerations

The work presented in this thesis comprises the building blocks towards a five year project and thus the eventual goals of this project must be considered in the design of the experiment. Future work seeks to establish coupling between a superconducting microwave resonator and trapped atomic ensembles. This presents several challenges not normally considered in atomic physics experiments. For example, superconducting resonators operate at cyrogenic temperatures and the highest critical temperature for a metal is 9.2 K for

Niobium [89], therefore a cryogenic environment is required.

Trapping single atoms in a dipole trap requires small trapping volumes to achieve high two body loss rates necessary to access the single atom regime [57]. Furthermore, imaging of single atoms requires high numerical aperture (NA) access to achieve the required high photon collection efficiency from the sample. Although methods exist to achieve reasonable NA at long working distances [90], an effective approach is to use lenses housed in the vacuum chamber close to the atoms to provide the high NA for imaging and the tight foci required for single atom loading [91, 92].

5.1.2 Design

Working at cryogenic temperatures restricts the experiment to operate with two chambers, as the atomic species used would stick to the walls of the chamber in the cryogenic region, the science chamber. The non-cryogenic magneto-optical trap (MOT) chamber is designed to allow optical axis for a 3D MOT with SAES caesium alkali metal dispensers used to supply the atoms. Initially the dispensers were housed in a CF16 Tee however it was found that this seriously prevented efficient loading of the MOT. To rectify this the dispensers were moved to inside the MOT chamber facing the centre from above. A 3 L/s ion pump is used to keep this chamber under vacuum and maintains a pressure of $P \leq 10^{-9}$ mbar.

The MOT chamber is separated from the science chamber through a differential pumping tube to provide independent pressure in both chambers. The tube is 4 mm in diameter and has a length of 10 mm to provide a differential pressure of over an order of magnitude. The diameter of the differential pumping tube is limited to 4 mm in order to provide sufficient optical axis for optical transport. A rendered CAD drawing of the vacuum system is shown in Fig. 5.1

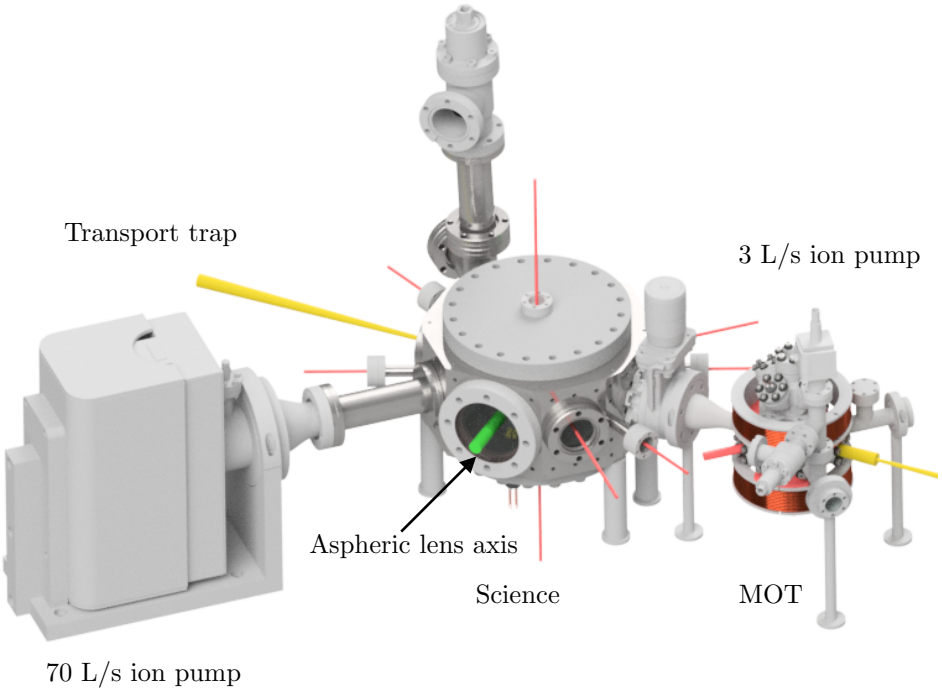

Figure 5.1: Rendered CAD drawing of vacuum system, the cooling/imaging beams are shown in red and the optical transport dipole beam path shown in yellow.

In order to achieve high photon collection efficiencies for single atom imaging and achieve diffraction limited foci for trapping and site addressability two high NA aspheric lenses (Geltech 355561) [91] $f = 10$ mm are located within the science chamber, offering a working distance of around 7 mm and NA=0.45 at 852 nm. These lenses were custom designed for the Rydberg experiment at Institut d'Optique led by Antoine Browaeys and further details can be found in [91, 93]. The lenses are held in a stainless steel (316L) custom designed mount allowing access in 3D for imaging/cooling beams, Fig. 5.2(a). To ensure the lenses sit flush with the mount a PEEK washer is placed between the lenses and the lip of the holder, this is then held in place with a stainless steel nut. This assembly is shown in Fig. 5.2(b). PEEK is used as it does not outgas at the temperatures used for baking the chamber, 150 °C. This mount restricts optical axis and prevents the horizontal mo-

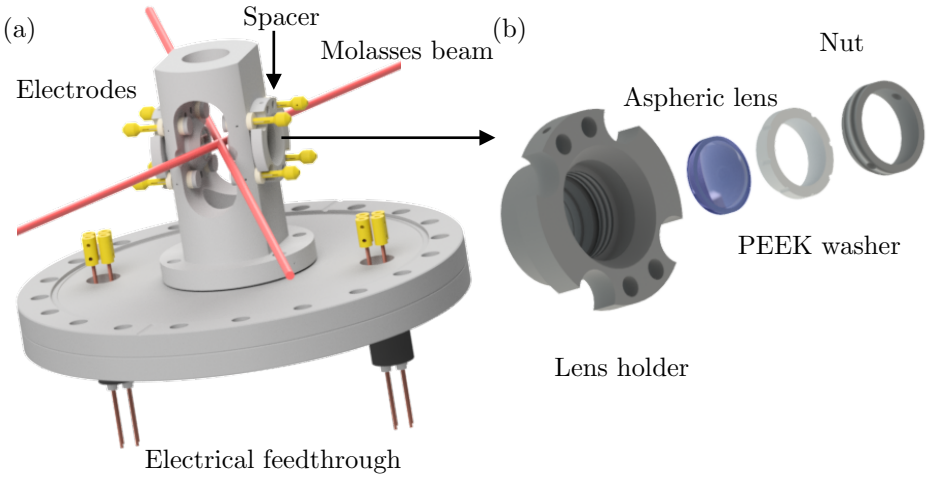

Figure 5.2: (a) Lens mount inside science chamber, vertical molasses beam not shown (b) Lens holder assembly, PEEK washer ensures lens holder sits flush and stainless steel nut used to lock in place.

lasses beams for single atom cooling and readout being orthogonal, requiring an angle of 35°. Prior to baking the chamber it is necessary to ensure that the focal planes of both lenses are equivalent. This is achieved by inputting a well collimated beam at $\lambda = 1064$ nm into the lenses and controlling the separation between them until the output is also well collimated. The separation is controlled with a set of stainless steel spacers and adjusting their thickness until the the desired output is achieved. The minimum thickness alteration that can made to the spacers is around 50 μm.

Due to the high sensitivity of Rydberg states to external fields further considerations have to be made in the design. The close proximity of the trapping sites to the lens surface requires the lenses to be coated in a layer of indium tin oxide (ITO) to suppress background electric fields. Further control over the electric field environment is achieved via 8 electrodes shown in Fig. 5.2(a).

Control of magnetic field environment is provided by 3 pairs of square shim coils in Helmholtz configuration designed to provided ~ 1 G/A. This is sufficient to cancel residual magnetic fields for sub-Doppler cooling and to provide large enough bias fields for optical pumping. However larger fields are re-

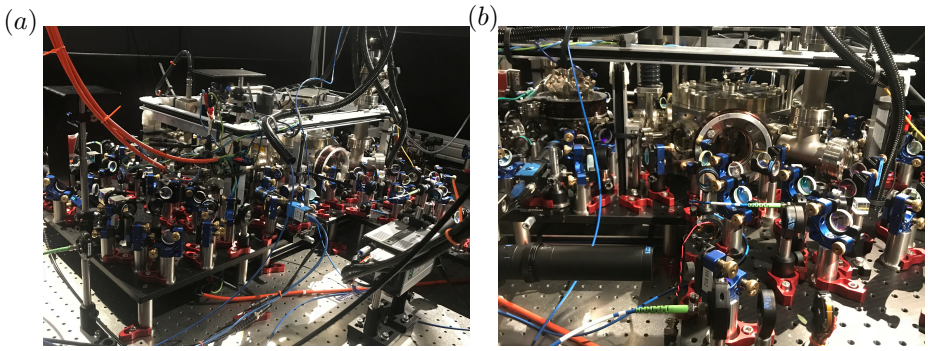

Figure 5.3: (a) Complete chamber assembly with shim coils and (b) along the aspheric lens axis with extra bias coils mounted on the chamber window.

quired along the aspheric lens axis to provide large separations between the hyperfine magnetic sub-levels for qubit rotations, this is achieved through an additional pair of circular bias coils mounted on the science chamber viewport to provide an additional ~ 1.3 G/A. A photo of the complete setup with the shim and bias fields is shown in Fig. 5.3.

5.2 Laser Cooling

Since the advent of laser cooling of atoms [94–96] in the mid 1980s, preparation of cold atomic samples is now readily achieved in laboratories across the world. The basis of such experiments usually comes in the form of a MOT [97], comprising 3 orthogonal pairs of counter-propagating beams and a pair of anti-Helmholtz coils. The coils provide a magnetic quadrupole field where there is zero field in the centre is surrounded by a linear gradient in all directions. The laser beams intersect at the centre of this field and are red detuned from an atomic resonance ω_0, such that as an atom is moving away from the centre it is Zeeman shifted into resonance with the laser beam in the opposite direction of the atoms displacement from the trap centre, creating a localised trap for the atoms. Cooling is achieved by the viscous force applied upon the atoms due to the Doppler effect. Atoms counter-propagating to the

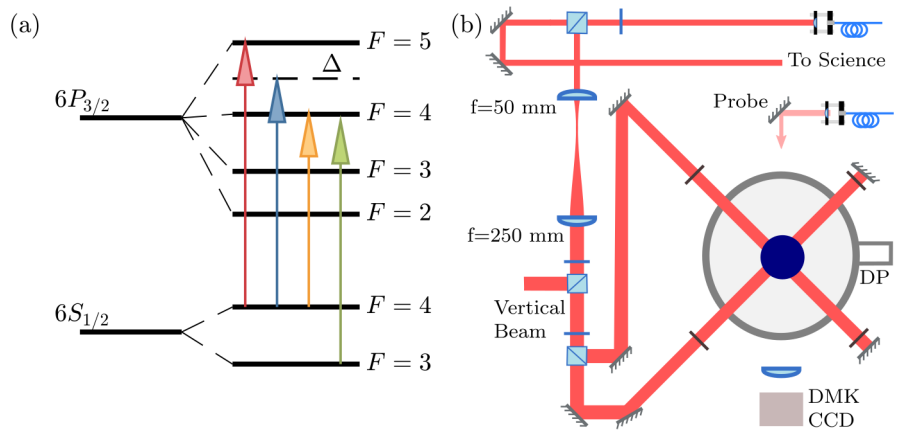

Figure 5.4: (a) Energy level of Caesium D_2 line and relevant transitions used for probe (red), cooling (blue), optical pumping (yellow) and repump (green). (b) Setup for MOT loading an imaging. DP = Differential Pumping Tube.

red detuned laser are Doppler shifted into resonance which slows and cools the atoms. The temperature limit of this cooling mechanism is known as the Doppler limit and is given by [94]

$$T_D = \frac{\hbar\Gamma}{2k_b}, \tag{5.1}$$

where Γ is the natural line-width of the cooling transition used, h is Planck's constant and k_B is the Boltzmann constant. For caesium this corresponds to a temperature of $T_D = 125\ \mu$K where $\Gamma/2\pi = 5.23$ MHz [81] for the D_2 line. However in reality much colder temperatures are observed via sub-Doppler cooling mechanisms [96] cooling atoms to about ten times the recoil limit [84]

$$T_r = \frac{\hbar^2 k^2}{m k_b}, \tag{5.2}$$

for cooling on the D_2 line of caesium this equates to $T_r \approx 200$ nK.

5.2.1 Cooling Lasers

Two lasers are required for laser cooling on the experiment; the master cooling laser which provides light for cooling, optical pumping and probe beam,

and the repump laser which is used to pump atoms out of the dark $F = 3$ state. A level diagram of caesium and the transitions driven by these lasers is shown in Fig. 5.4(a). Both lasers are home-made external cavity diode lasers (ECDL) [98] and use the same 150 mW laser diode (Thorlabs: L850P150). The master cooling laser is locked to the $F = 4 \rightarrow F' = 5$ atomic transition via polarisation spectroscopy [99], shifted by 400 MHz through a double passed 200 MHz AOM. Light for the probe and optical pumping are then picked off via polarising beam splitters (PBSs) and passed through independent AOMs to shift the desired frequency allowing control of detuning. The master source is then passed through a tapered amplifier (TA) to increase the available power for trapping, cooling and to offer flexibility for future experiments. This then passes through another double passed 200 MHz AOM to bring the light back into resonance. The repump laser is also locked using polarisation spectroscopy however it is locked onto the $F' = 2 - 4$ cross over feature and shifted by a double passed 88 MHz AOM to bring it into resonance with the $F = 3 \rightarrow F' = 4$ transition.

5.2.2 MOT

The MOT cooling and repump light are combined on a 50:50 non-polarising beamsplitter with the same polarisation and coupled into a single mode fibre and brought over to the experiment table. They are then split on a PBS which allows the power balance between the MOT chamber and science chamber to be controlled with a $\lambda/2$ waveplate. The MOT beams are then expanded using a 1:5 telescope to a $1/e^2$ beam intensity radius (waist) of 4.7 mm, this size of the beam is limited by the clear aperture of the MOT windows (25.4 mm). Further splitting of the cooling beam with PBS's allows the cooling light to be balanced between three pairs of retro-reflected beams, as shown in Fig. 5.4(b). The MOT is loaded directly from background vapour which is provided by applying a current of 3.1 A through a SAES getter.

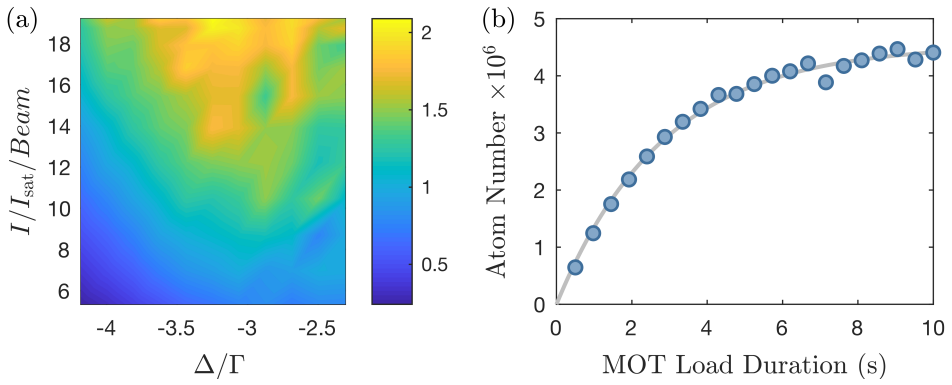

Figure 5.5: (a) Atom number vs cooling intensity and detuning finding an optimal detuning of $\Delta \sim -3\Gamma$, I/I_{sat} corresponds to the intensity per beam. (b) MOT load curve (single shot) obtaining a fill time $\tau_L = 2.8$ s and an equilibrium number of $N_{eq} = 4.5 \pm 0.1 \times 10^6$.

The anti-Helmholtz coils provide a magnetic field gradient of 1.11 G/cm/A and fast switching the coils enabled through a water cooled FET circuit. It is found that optimal loading of the MOT occurs when a gradient of 13-14 G/cm is applied.

The number of atoms and the size of the atomic cloud is measured using a weak resonant probe beam to absorption image onto a CCD camera (DMK 335G445). To characterise the loading of the MOT the detuning and intensity of the cooling beams are investigated over 1 s loading durations. The results of this investigation are presented in Fig. 5.5(a). It is found that the optimal detuning for loading atoms into the trap is $\sim -3\Gamma$.

After loading for a period of time t, the MOT will reach an equilibrium number N_{eq}, the relation between this and the number loaded is is given by [100],

$$N(t) = N_{eq}\exp(1 - t/\tau_L), \tag{5.3}$$

where τ_L is the fill time constant. After loading the MOT for different durations this is fitted to the data in Fig. 5.5(b) obtaining a fill time $\tau_L = 2.8$ s and an equilibrium number of $N_{eq} = 4.5 \pm 0.1 \times 10^6$. Increasing the dispenser current could yield larger atom numbers however for the purpose of

this experiment loading 10^5atoms/s is sufficient.

5.2.3 Optical Molasses

The cooling mechanism responsible for loading the 3D MOT typically cools the atoms to $T \approx 300$ μK further cooling to sub-Doppler temperatures is achieved through an optical molasses stage following trapping at null field. This sub-Doppler phenomenon is due to the varying potential an atom experience in the presence of polarisation gradients created by counter-propagating circularly polarised fields [96] and is known as polarisation gradient cooling (PGC). Fig. 5.6(a) shows how the temperature rapidly changes during the PGC period from around 300 μK to less than 10 μK within 5 ms. The temperature reached from this method is directly related to a dimensionless light-shift parameter $\Omega^2/|\Delta|\Gamma$ [101]

$$\frac{k_B T}{\hbar\Gamma} = C_{\sigma^+,\sigma^-}\frac{\Omega^2}{|\Delta|\Gamma} + C_0, \tag{5.4}$$

where $\Omega = \Gamma\sqrt{I/2I_{\text{sat}}}$ is the Rabi frequency and I_{sat} the saturation intensity. This relation is investigated through temperature measurements made for different molasses parameters. The MOT is loaded for 1 s following this the magnetic field gradient is switched off and the detuning and intensity are then ramped over a period of 2 ms to the desired value and cooled for a further 10 ms. The light is then extinguished to allow the cloud to expand for a variable time t, before the imaging pulse is applied. Measuring for different time-of-flight durations allows the temperature to be extracted as the atom cloud's expansion is dependent upon the temperature

$$\sigma_x(t)^2 = \sigma_x(0)^2 + \frac{k_B T}{m}t^2, \tag{5.5}$$

where σ_x is the standard deviation of a gaussian fit to the cloud. The temperature is then determined from the gradient of t^2 vs σ_x^2. Fig. 5.6(b) shows the

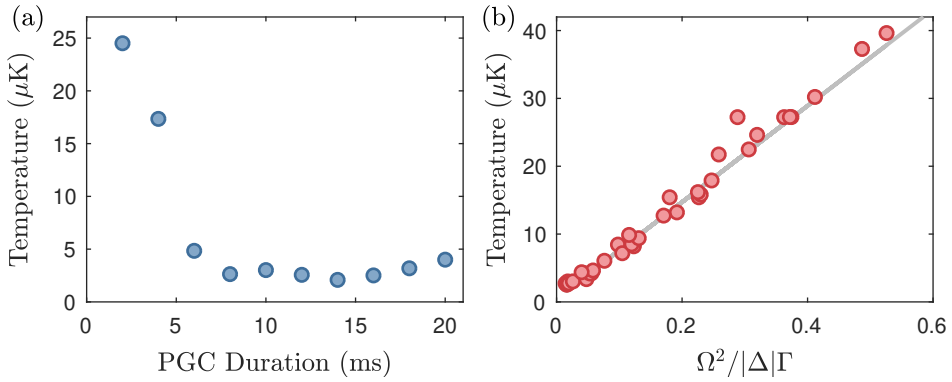

Figure 5.6: (a) Temperature vs molasses duration, at t=0 the temperature of the cloud is $T \sim 350$ μK. (b) Temperature compared to the dimensionless light shift obtaining a minimum temperature of $T = 2.5 \pm 0.2$ μK, corresponding to a molasses detuning of $\Delta/2\pi = -15\Gamma$ and molasses intensity per beam of $I/I_{\text{sat}} = 0.5$ mW/cm^2, the fit yields $C_{\sigma^+,\sigma^-} = 0.28$

results from the experiment described above to extract $C_{\sigma^+,\sigma^-} = 0.28$ with the minimum obtained temperature $T = 2.5 \pm 0.2$ μK in close agreement with results obtained in [102].

5.3 Optical Transport

The MOT described in the previous section provides a source of cold atoms for the experiment, however these atoms are still required to be transported 30 cm through to the science chamber. This is achieved via an optical dipole trap and a mechanical translation stage.

5.3.1 Dipole Traps

The interaction between an electric field and an atom induces a dipole moment. The dipole potential arising from this interaction is dependent upon the intensity of the field and the detuning of the interacting fields. For a red (blue) detuned beam the atom is drawn and trapped in the regions of high (low) intensity. Red detuned traps are therefore simple to implement with the focus of a gaussian beam offering confinement in 3D. In the limit of

the rotating wave approximation [84] this conservative trapping potential is given by [36]

$$U_{\mathrm{dip}}(\mathbf{r}) = \frac{3\pi c^2}{2\omega_0^3}\frac{\Gamma}{\Delta}I(\mathbf{r}), \tag{5.6}$$

where ω_0 is the angular frequency of the atomic resonance and the scattering rate from the trapping field is given by

$$\Gamma_{\mathrm{sc}}(\mathbf{r}) = \frac{3\pi c^2}{2\hbar\omega_0^3}\left(\frac{\Gamma}{\Delta}\right)^2 I(\mathbf{r}). \tag{5.7}$$

What is imperative from the relations above is that $U_{\mathrm{dip}} \propto I/\Delta$ and $\Gamma_{\mathrm{sc}} \propto I/\Delta^2$, it is therefore advantageous to use light far detuned from the transition frequency, this however results in a reduction in trapping potential but can be compensated by increasing the laser power.

For a focused beam the atom experiences a spatially varying potential due to the intensity distribution of a Gaussian beam [36]

$$I(r,z) = \frac{I_0}{1+z^2/z_r^2}\exp\left(-2\frac{r^2}{w^2(z)}\right), \tag{5.8}$$

where for a Gaussian beam $I_0 = 2P/\pi w_0^2$. In the axial direction the waist evolves as $w(z) = w_0(1+(z/z_{\mathrm{R}}))^{1/2}$ where w_0 is the $1/e^2$ intensity radius of the waist and the Rayleigh range is $z_{\mathrm{R}} = \pi w_0^2/\lambda$. Thus the trapping potential takes the form

$$U(r,z) = \frac{U_0}{1+z^2/z_{\mathrm{R}}^2}\exp\left(-2\frac{r^2}{w^2(z)}\right), \tag{5.9}$$

where U_0 can be obtained by evaluating Eq. 5.6 for the peak intensity I_0,

In reality atoms have more than two levels so it is necessary to expand this expression to considered the effective detuning's from the D_1 line ($6S_{1/2} \rightarrow 6P_{1/2}$), Δ_{D1} and the D_2 line ($6S_{1/2} \rightarrow 6P_{3/2}$), Δ_{D2} [36]

$$U_0 = \frac{3\pi c^2}{2}\left(\frac{1}{3}\frac{\Gamma_{\mathrm{D1}}}{\omega_{\mathrm{D1}}^3\Delta_{\mathrm{D1}}} + \frac{2}{3}\frac{\Gamma_{\mathrm{D2}}}{\omega_{\mathrm{D2}}^3\Delta_{\mathrm{D2}}}\right)I_0. \tag{5.10}$$

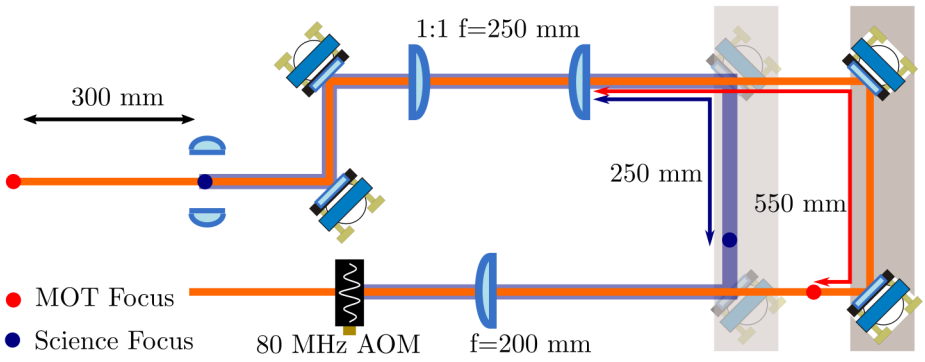

Figure 5.7: Optical setup for dipole trapping; the position of the waist behind the 1:1 telescope is controlled by the position of the two mirrors on the translation state with the position before the relay lens being reflected in the chamber. For ease of illustration the beam expander is not shown.

Due to the Gaussian profile the trapping in this potential is anisotropic with confinement in the radial direction (r) being much stronger than that in the axial direction (z). As the atoms are cooled and loaded into the trap it can be expected that they sit at the bottom of the potential where it is approximately a harmonic potential with axial and radial trapping frequencies

$$\omega_z = \sqrt{\frac{2U_0}{mz_r^2}}, \quad \omega_r = \sqrt{\frac{4U_0}{m\omega_0^2}}. \tag{5.11}$$

5.3.2 Experimental Implementation

The dipole trap used in this experiment requires a waist that can be translated from the MOT chamber to the science chamber to transport the atoms, which is achieved using a mechanical stage. Light is sourced from a 10 W 1064 nm Nd:YAG laser. After passing through an AOM for switching the beam is expanded by a telescope $f_1 = -30$ mm, $f_2 = 300$ mm to 1.9 mm. This is then focused down to a 40 μm spot by a $f = 200$ mm lens. Two mirrors on the translation stage form a folded path and control the position of this focus before a 1:1 $f = 250$ mm relay telescope which then images this waist into the vacuum chamber. This allows the waist, and therefore the

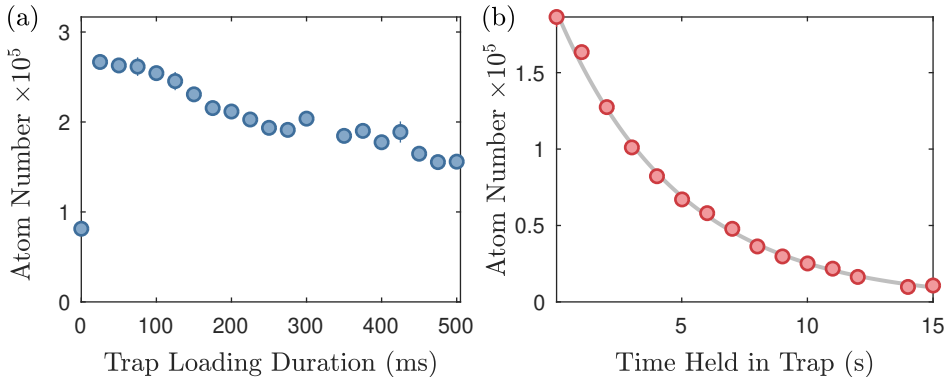

Figure 5.8: (a) Dipole trap loading vs overlap period with the MOT (b) trap lifetime yielding a $1/e$ lifetime of 4.9 s

trapping potential to be kept constant when moving the focus position from the MOT position to the centre of the science chamber. A schematic of the setup is shown in Fig. 5.7.

In order to perform fast and efficient optical transport the axial trapping frequency must be fast compared to the timescale of the transport. Initial attempts to implement transport on the experiment found serious limitations due to a weak axial frequency $\omega_r < 3$ Hz due to thermal lensing when trying to use focus adjustable lenses as in [103]. This resulted in a 20 μm increase is spot size compared to target specification. The setup here is designed for a target waist of $w_0 = 40$ μm to achieve $w_z/2\pi \approx 9$ Hz.

Loading the dipole trap is simply achieved by turning the trapping potential on after the MOT has loaded. It is found a period of 50 ms overlapping the dipole beam with the MOT beams is sufficient to load the trap obtaining over 10^5 atoms before collisions within the trap cause the number loaded to decay, Fig. 5.8(a). Following loading a polarisation gradient step ensues cooling the trapped atoms down to 10 μK. This temperature is slightly more than obtained from molasses and is due to adjusting parameters to maximise number loaded over temperature with spatially varying AC stark shifts making it hard to satisfy both parameters.

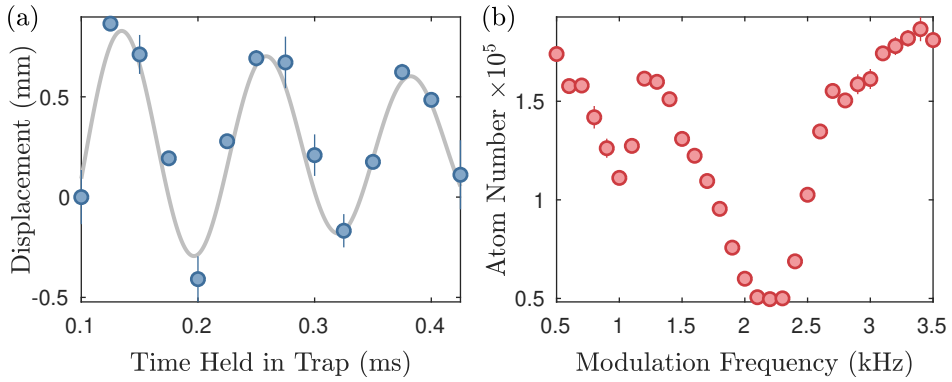

Figure 5.9: Trap frequency measurements (a) axial $\omega_z/2\pi = 8.1 \pm 0.1$ Hz (b) radial $\omega_r/2\pi = 1.1$ kHz.

Trap Lifetime

The lifetime of the trap is measured through varying the time the trap is held after loading and cooling before imaging. In Fig. 5.8(b) this data is fit to an exponential decay finding a $1/e$ decay time of 4.9 s. This lifetime is found to be predominantly limited by collisions with background gasses as pumping into $F = 3$ to reduce the two body loss rate does not result in any improvement [36, 104].

Trap Frequencies

The axial frequency is measured by using the translation stage to change the focus of the dipole trap slightly off the centre of the MOT when loading. This causes the loaded atoms to slosh around the bottom of the potential at the angular frequency ω_z recording the position of cloud as a function of the time held which allows the axial frequency to be extracted. Data from this measurement are shown in Fig. 5.9(a) and fitted to a damped sine wave obtaining $\omega_z/2\pi = 8.0 \pm 0.1$ Hz. After factoring in losses through the AOM and transmission through lenses and the vacuum windows 6.8 W of power is available at the atoms in the MOT chamber. Since the power is known the trap waist can know be extrapolated obtaining $w_0 = 43$ μm and therefore $U_0 = 600$ μK.

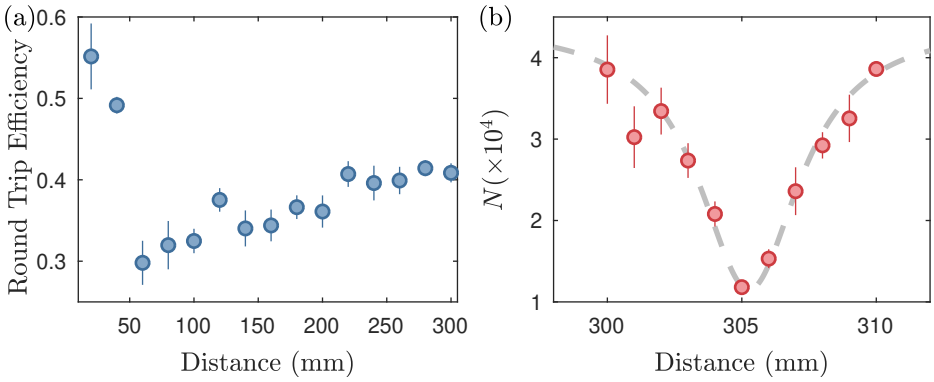

Figure 5.10: (a) Round trap efficiency using $v_{\max} = 0.2$ m/s, $a_{\max} = 0.6$ m/s^2 and jerk=20 m/s^3 the dip in return efficiency occurs around the differential pumping tube. (b) Finding micro-trap location, a resonant probe is aligned through the aspheric lenses to located position of microtraps.)

The radial frequency can also be measured through modulating the trap intensity at $n\omega_r$, this causes parametric heating of the atoms and results in their loss from the trap. In order to do this the power in the trap has to be reduced so there is an overhead to modulate. The trap is reduced to 4 W (expected $\omega_r/2\pi = 1.1$ kHz using the waist obtained from the axial measurement) and the intensity is sinusoidally modulated for 100 cycles with an amplitude of 0.5 W, the frequency of this modulation is scanned and shown in Fig. 5.9(b). It can be seen that there are two regions of loss in this scan, these correspond to ω_r and $2\omega_r$ obtaining $\omega_r/2\pi = 1.1$ kHz. For 4 W of power this obtained frequency is in excellent agreement with what was obtained from the axial measurement

The slight discrepancy between the waists indicated from the trap frequency measurements and with target specification is suspected to arise from thermal lensing of the NBK-7 chamber windows.

5.3.3 Transport

Following loading and cooling of the trap the translation stage is triggered to move 150 mm (moving 300 mm due to the folded path). The stage controller

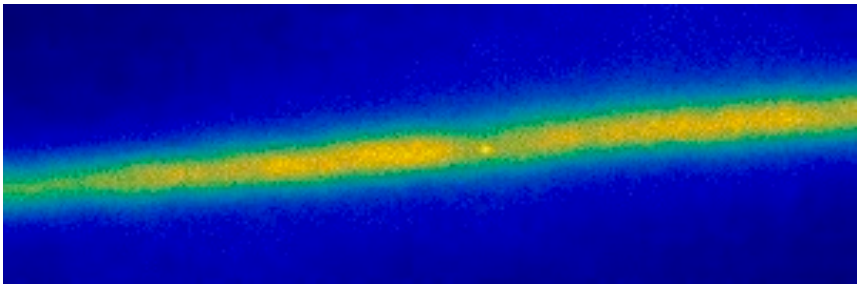

Figure 5.11: First image obtained of the transport trap and mircotrap overlapped, the mircotrap can be seen as a small region of localised density within the transport trap.)

allows input of an S-curve profile in velocity for motion with a set maximum velocity ($v_{\max}$), acceleration ($a_{\max}$) and jerk da/dt. Once initiated the stage moves at maximum jerk until maximum acceleration is reached, it then begins to decelerate smoothly with negative jerk to achieve maximum velocity. The opposite of this process then occurs to bring the stage to a stop. During the alignment phase this required operation with modest parameters ($v_{\max}$ = 0.2 m/s, $a_{\max} = 0.6$ m/s^2 and jerk=20 m/s^3) for adiabatic transport so that the atoms could survive a round trip without being heated out of the trap due to the motion, taking around 2 s for a one way trip. Fig. 5.10(a) shows the round trip efficiency obtained using this sequence with a constant trapping duration to remove lifetime effects. There is a reduction in efficiency around 50 mm which corresponds to the region of the differential pumping tube. The slight increase thereafter is attributed to the better background pressure in the science chamber.

Alignment of the transport axis so that it intercepts the MOT as well as the centre of the aspheric lenses proved to be a challenging issue. This ultimately required aligning the probe beam by the side of the aspheric lenses and monitoring the retention of the atoms that made the return journey to the MOT chamber as shown in Fig. 5.10(b). Once the probe was aligned upon the atoms (represented by maximising loss on return trip) a beam profiler was used to work out the trap height in the chamber. Over many iterations

this process finally yielded a signal on the single atom camera as shown in Fig. 5.11 where the mirco-trap has also been set up to intercept the trap as can be seen in the small region of high intensity in the image.

Upon achieving alignment it was found that single atom loading was not detrimentally affected through operating the stage at its maximum velocity and acceleration, $v_{\max} = 0.6$ m/s and $a_{\max} = 10$ m/s^2, reducing the optical transport time to 800 ms.

5.4 Summary

A cold atomic source is provided through a 3D MOT and due to experimental considerations this is housed in a separate chamber and requires the cold atoms to be optically transported via a dipole trap into the science region. High NA access is offered to the experiment through lenses housed in this chamber offering tight focuses required for single atom trapping and high collection efficiencies for imaging.

Chapter 6

Single Atom Trapping and Imaging

Single atom imaging requires both spatial and number resolution, where a finite number of scattered photons are collected by high numerical aperture (NA) optics in order to obtain a large collection efficiency from atoms in microscopic traps [90, 91, 105, 106], optical lattices [107] or magnetic traps [108]. This enables multiple readouts of the same atom with hyperfine resolved detection of atomic qubits [109] or counting of individual atoms in ensembles of over 100 atoms [110].

Due to the low photon numbers reaching the detector (typically ~ 10 photons/ms/atom), single atom detection has typically been performed by single photon counting modules (SPCMs) [57] or photomultiplier tubes (PMTs) [111] offering extremely low dark counts but only a single pixel. Therefore spatially resolved detection has until now been exclusively performed with electron-multiplying charge-coupled device (EMCCD) cameras [112] or a standard scientific CCD coupled with an intensifier [113].

This chapter presents the trapping, imaging and characterisation of single atoms. Imaging is achieved using a scientific complementary metal-oxide

semiconductor (sCMOS) camera. Unlike an (EM)CCD camera, each pixel is read out independently, removing clock induced charge noise and permitting higher readout speeds whilst offering a superior signal-to-noise-ratio (SNR) for intermediate incident photon rates. The work presented in the chapter resulted in the publication [114].

6.1 Camera SNR

Essential to performing imaging with single atom resolution is overcoming detector noise to discriminate the weak photon events from a single atom over the background count rate. The signal-to-noise ratio (SNR) of a camera is given by [115]

$$\mathrm{SNR} = \frac{nQE}{\sqrt{F_n^2 QE(n+n_b) + (\delta_{ro}/M)^2}}, \tag{6.1}$$

where n is the number of incident photons per pixel, n_b is the number of background photons per pixel, QE is the quantum efficiency, F_n the noise factor, M the multiplication factor and δ_{ro} is the camera readout noise. Other camera noise factors such as clock induced charge and dark noise have been considered negligible for the cameras and imaging timescales examined. From the above relation it can be seen that having a low readout noise coupled with a large QE is crucial to achieve high SNRs at low photon levels.

Standard scientific CCD detectors perform with SNRs close to that of an ideal detector for high photon numbers due to their near perfect noise factor, $F_n = 1$. However in the limit of few photons $\approx$ 10 photons/px, the SNR suffers due the high readout noise [116] $\delta_{ro} > 6e^-$. An EMCCD camera overcomes this constraint through an electron multiplying process which amplifies the signal up to $M \sim 1000$, allowing an effective readout noise $\delta_{ro}/\mathrm{M} < 1\mathrm{e}^-$ to be achieved [117]. This multiplication process results in an increased noise factor, $F_n = \sqrt{2}$, but makes it an incredibly powerful tool for low photon

imaging applications, such as imaging single atoms and ions.

Recent advances in sCMOS cameras have made it a contender in low light imaging. Each pixel is read out independently, enabling larger sensor sizes with a high speed FPGA to process readout [118, 119]. The use of ultra low noise MOSFETs reduces the readout noise to values [120] as low as $2e^-$. This ensures fast integrated readout times and since there is no additional amplification process a near perfect noise factor $F_n = 1$ is achieved, allowing the sCMOS to be competitive at intermediate photon levels of 10-100 photons/px.

The sCMOS camera used on the experiment is the Andor Zyla 5.5. In global shutter mode with 200 MHz readout speed, $\delta_{ro} = 2.2\ e^-$ rms with a maximum QE of 60%. Table 1 compares the SNRs for top of the line cameras using EMCCD and CCD technology as well as the Zyla. It can be seen when operating in the range of the best QE that the Zyla outperforms the other technologies for mid level photon events while still providing a competitive SNR for low level imaging. For caesium imaging, $\lambda = 852$ nm, $QE = 22\%$ giving a performance that is comparable to an EMCCD for 100 photons/px.

Detector	10 photons/px		100 photons/px		1000 photons/px	
	Best	852 nm	Best	852 nm	Best	852 nm
Zyla	1.8	0.8	7.4	4.2	24.4	14.7
EMCCD	2.1	1.7	6.7	5.2	21.2	16.6
CCD	0.7	0.2	5.4	1.8	24.7	11.5

Table 6.1: SNR comparison of different available camera technologies for both the best QE and the QE at 852 nm. The EMCCD considered is the Andor iXON Ultra 897 ($QE = 90\%, QE_{852} = 60\%, \delta_{ro} = 89$ e$^-$(17 MHz operation), $M = 1000, F_n = \sqrt{2}$) [117] and the CCD is the Hamamatsu Orca-R2 ($QE = 70\%, QE_{852} = 20\%, \delta_{ro} = 10$ e$^-$(fast scan mode), $F_n = 1$) [116].

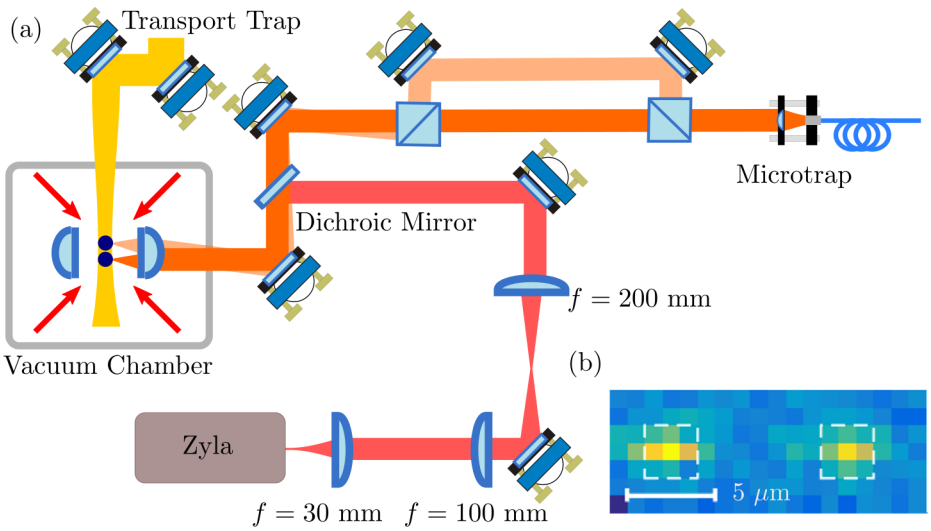

Figure 6.1: (a) Single atom imaging setup. Yellow = transport trap, orange = microtraps , red = fluoresced 852 nm light (b) Single shot image of two single atoms separated by 10 μm

6.2 Single Atom Loading

Following the optical transport described in the previous chapter the transport beam is overlapped with a pair of microscopic tweezer traps for a period of 60 ms with weak 3D cooling light, $I = I_{\text{sat}} = 2.7$ mW/cm^2 [81] per beam with a detuning $\Delta = -6\Gamma$ to load multiple atoms into each of the microscopic traps. The traps are formed using $\lambda = 1064$ nm using the optical layout shown in Fig. 6.1 with PBS's used to split and recombine light to provide two trapping sites. After loading atoms into the microscopic dipole traps, a 100 ms single atom loading stage is performed at a detuning of $\Delta = -8\Gamma$ and an intensity of $\sim$0.5 I_{sat} per beam. To remove light shifts associated with the trapping potential, cooling light is chopped out of phase with the trapping light at 1 MHz with a 35% duty cycle. Due to the small trapping volume single atom loading via collisional blockade [58] is achieved. In this regime light-assisted collisions (LACs) cause pairs of atoms to be lost from the trap.

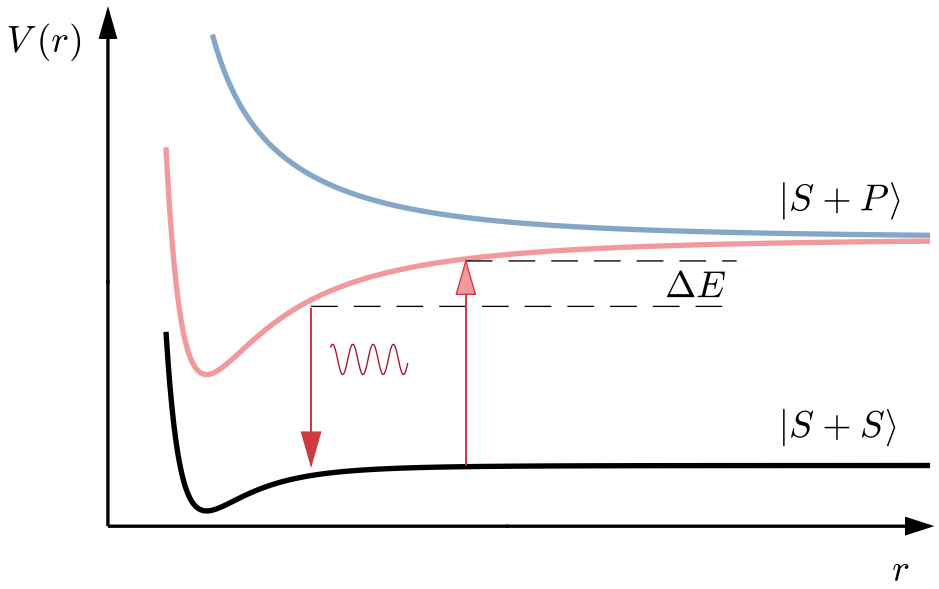

Figure 6.2: Schematic of Light Assisted Collision process, red- detuned light excites two ground state atoms into the excited molecular pairstate where attractive dipole-dipole interactions cause the atoms to accelerate towards each other rolling down the potential. Upon spontaneous emission this is transferred to an increase in kinetic energy causing the loss of both atoms from the trap.

6.2.1 Light Assisted Collisions

Consider two atoms with a ground and excited state molecular potentials $V_g(r)$ and $V_e(r)$ with an inter-nuclear atomic separation r. At long range there is a ground pair-state represented by $|S+S\rangle$ and the first excited state $|S+P\rangle$ separated by $\hbar\omega$. The ground state interaction is governed by a long range asymptote $V(r) = C_6/r^6$ and thus is weak and contribution can be neglected. The excited molecular state interacts via resonant dipolar interactions and has a long range of asymptote $V(r) = \hbar\omega \pm C_3/r^3$, resulting in either a repulsive or attractive potential [121, 122]. This results in a shift of the resonance dependent on the separation of the atoms and as illustrated in Fig. 6.2 a choice of detuning can excite into either the attractive or repulsive potential. We will concentrate on the attractive potential excited with red-detuned light. In this situation the atoms accelerate towards each other and

roll down the $|S + P\rangle$ potential curve before spontaneous emission returns to the excited atom to ground state gaining kinetic energy $\Delta E \gg \hbar U_0$ resulting in both atoms being lost from the trap. Therefore single atom loading is dependent on the stochastic process of the initial number of atoms loaded (odd reduces to single atom, even reduces to zero) resulting in an expected loading rate if 50% via this method. Near deterministic approaches have been shown achieving over 90% loading via blue detuned light on the D_1 transition. This is achieved through careful choice of the detuning to limit the kinetic energy gained to cause only one atom to be lost [112, 123]. Until recently, loading by this method generally took over 0.5 s, however a recent demonstration has shown to reduce this to 170 ms [124] offering a potential for near deterministic loading without compromising experiment duty cycle.

6.3 Single Atom Imaging

Light scattered by the atoms is collected by the aspheric lens described in Sec. 5.1.2 and separated from the microtrap beams using a dichroic mirror as shown in Fig. 6.1(a). The collected light is then focused by a $f = 200$ mm lens to create a confocal imaging setup where the beam is imaged onto the Zyla sensor chip through a relay telescope ($f_1 = 100$ mm, $f_2 = 30$ mm). This enables filtering in the Fourier plane using narrowband interference filters to block the 1064 nm light reaching the camera and transmit only the 852 nm light from the atoms, with a measured transmission of 83% at 852 nm. The combined detection efficiency of the imaging system including the filters is 3.5%. Zemax calculations give a paraxial magnification of -20.5 at the intermediate focus of the 200 mm lens, resulting in a total magnification of M=+0.62 between object plane in the chamber and the image plane on the Zyla; this corresponds to an effective pixel size of 1 μm. Calibration of the relay imaging using a USAF 1951 resolution test chart finds a sub-pixel point spread function of 0.7 ± 0.1 μm.

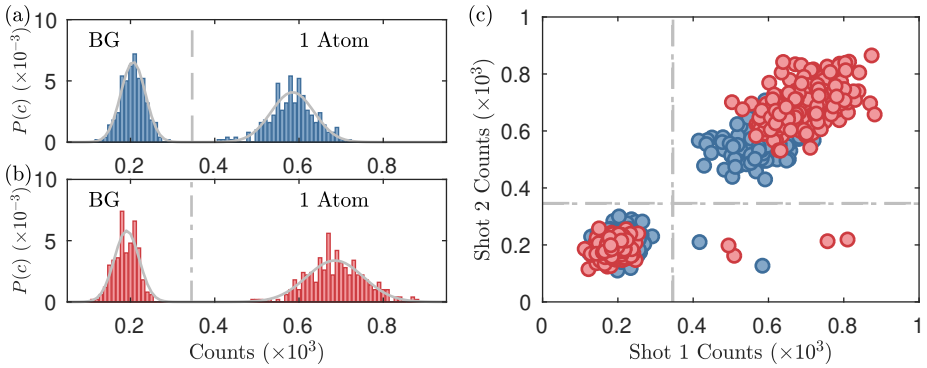

Figure 6.3: Probability distribution of the counts from 500 measurements recorded for (a) trap 1 and (b) trap 2 using a 40 ms exposure. (c) Correlation plot showing counts from the first image plotted against the counts for an image taken 50 ms later

In order to detect single atoms, a sufficient number of photons must be scattered in order to distinguish between scattered background light and the events due to the single atom. The photon scattering rate for a single atom is given by [84]

$$\Gamma_{\mathrm{sc}} = \frac{\Gamma}{2} \frac{I/I_{\mathrm{sat}}}{1 + I/I_{\mathrm{sat}} + 4(\Delta/\Gamma)^2}, \tag{6.2}$$

where Δ is the detuning and I the intensity. The above relation clearly shows that the largest scattering rate is achieved on resonance, however imaging on resonance causes heating and eventually the loss of the atom from the trap. Imaging in experiments is therefore performed with 0.5 I_{sat} of cooling power per beam at a detuning of $\Delta = -3\,\Gamma$, utilising the same out of phase chopped light pulses described above resulting in an effective photon scattering rate of $\Gamma_{\mathrm{sc}} = 450$ photons/ms, with an expected flux of 15 photons/ms incident on the camera. Fig. 6.1(b) show a typical image obtained imaging in this way using a total imaging time of 40 ms, showing two clearly resolved optical traps with a separation of 10 μm.

Single atom loading of the trap sites is verified through the emergence of a bimodal probability distribution for the number of counts detected within a 3×3 pixel region of interest centred on each trap following the LAC stage. Fig. 6.3(a,b) shows the probability distribution obtained from 500 repeated

measurements using the imaging parameters described above for each trap, which clearly reveals two well separated distributions corresponding to a Poisson distribution centred at a mean count rate μ_0 when no atom is loaded, and a second distribution centred at a mean μ_1 when an atom is present. The reduced count rate observed from atoms in trap 1 is due to a weak standing wave in the retro-reflected MOT beams creating a position-sensitive scattering rate.

Further evidence for single atom loading is obtained by comparing the results of imaging the same trap twice in a single measurement run. Fig. 6.3(c) shows correlations between counts in shot 1 and counts in a second shot taken 50 ms later, revealing two distinct clusters associated with having 0 (1) atoms present in both shots, and a small number of points in the lower right quadrant corresponding to an atom initially loaded in shot 1 but having been lost by shot 2. Collating the data in this way also clarifies the ability to retain the atom after readout, with $> 98\%$ retention probability for having an atom present in the second shot for both traps (dominated by collisional loss from background gas as shown below). With the LAC stage, we never observe counts corresponding to double load events confirming a robust single atom loading sequence.

In order to analyse the data, we approximate the Poisson count distributions with a large mean to a bimodal Gaussian distribution using the equation

$$P(c) = p_0 G(c, \mu_0, \sigma_0) + p_1 G(c, \mu_1, \sigma_1), \tag{6.3}$$

where p_i is the probability of loading zero or one atom and $G(c, \mu, \sigma) = 1/\sqrt{2\pi\sigma^2}\exp\{-(c-\mu)^2/(2\sigma^2)\}$ is a normalised Gaussian distribution. Fitting the data in Fig. 6.3 gives the parameters summarised in Table. 6.2, with both traps loading atoms $> 50\%$ of the time corresponding to sub-Poissonian loading as observed in other experiments [57].

For each measurement the count rate in the first shot is used to determine

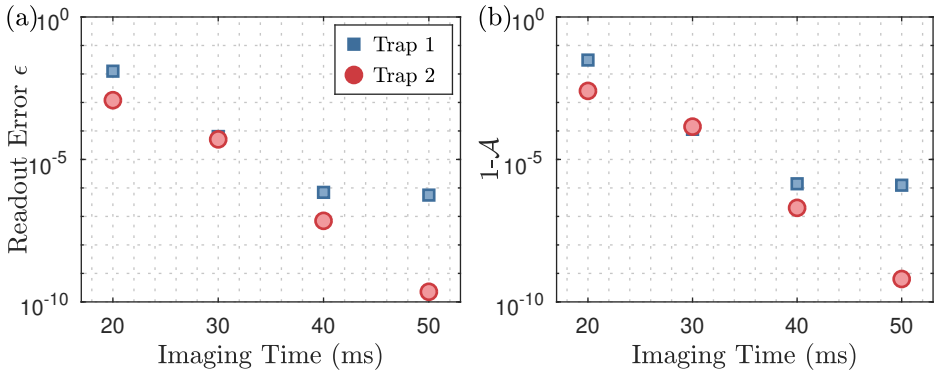

Figure 6.4: (a) Readout error and (b) Acceptance as a function of imaging duration.

if an atom is present in the trap by introducing a threshold value c_{min} above which an atom is assigned to the trap. Data in shot two is then analysed conditional upon detection in shot 1, either through fitting the resulting bimodal distribution to extract p_1 or again using a threshold method. The error ϵ associated with correctly labelling an atom in the trap is calculated using

$$\epsilon = \int_{c_{\text{min}}}^{\infty} p_0 G(c, \mu_0, \sigma_0) \mathrm{d}c = \frac{p_0}{2}\left[1 - \text{erf}\left(\frac{c_{\text{min}} - \mu_0}{\sqrt{2}\sigma_0}\right)\right], \tag{6.4}$$

whilst the acceptance $\mathcal{A}$ (defined as the fraction of single atom load events accepted using $c > c_{\text{min}}$) is given by

$$\mathcal{A} = \int_{c_{\text{min}}}^{\infty} G(c, \mu_1, \sigma_1) \mathrm{d}c = \frac{1}{2}\left[1 - \text{erf}\left(\frac{c_{\text{min}} - \mu_1}{\sqrt{2}\sigma_1}\right)\right]. \tag{6.5}$$

Fig. 2 shows cut-off values chosen to minimise the overlap volume between the two probability distributions corresponding to $c_{\text{min}} = 346, 345$ for trap 1 and 2 respectively. The corresponding error is $\epsilon < 8 \times 10^{-7}$ with an acceptance $\mathcal{A} > 99.99\%$ for both traps, giving high measurement fidelity.

Trap	μ_0	σ_0	μ_1	σ_1	$p_1(\%)$
1	206	29	586	51	52
2	191	29	685	67	57

Table 6.2: Fit parameters for data in Fig. 2 to Eq. 6.3.

Fig. 6.4 shows the evolution of ϵ and $\mathcal{A}$ as a function of imaging duration for both traps, showing that 40 ms provides an optimal readout time as for longer imaging durations heating in trap 1 limits readout fidelity.

6.4 Comparison to EMCCD hardware

The results above demonstrate that high fidelity state detection is achievable using sCMOS sensors despite the limited quantum efficiency compared to EMCCD cameras as summarised in Table 1, meaning simply scattering more photons and thus slightly increased heating to achieve the same number of photon detection events but still providing excellent performance. For experiments requiring fast repetition rate, readout time is also a consideration. Using the present hardware multiple images can be performed with a minimum separation of 10 ms for frame transfer, compared to 100 ms for a recent demonstration of non-destructive quantum state readout with an EMCCD camera [109], significantly reducing sensitivity to losses arising from background-gas collisions between detection events and enabling faster experiment cycle times. Another important factor however is cost, with the Andor Zyla providing comparable performance for less than a third of the cost of the popular Andor iXon EMCCD camera, making sCMOS highly competitive for single atom imaging applications.

To extend the current results to enable a hyperfine-resolved imaging for quantum state readout, it is necessary to scatter light from the upper hyperfine ground-state using a closed-transition and collect a sufficient number of photons to discriminate the counts above background before the atom undergoes a hyperfine changing transition due to off-resonant Raman processes or imperfect polarisation of light. Kwon *et al.* have demonstrated this for Rb, where with 2% conversion efficiency from photons to counts they observed non-destructive quantum state discrimination from 7500 photon scattering

events [109]. In the present Cs experiment we obtain an equivalent conversion efficiency of 2.1, 2.7 % for the two traps respectively, meaning similar results should be achievable.

Finally, due to the FPGA hardware integrated alongside the sCMOS sensor chip [120] it should be possible to perform high-speed single pixel readout and image processing on the camera itself [119], resulting in high-speed state detection and removing the need for frame transfer. Progress towards this goal is currently limited by the proprietary camera firmware, however in future customisable hardware will become more widely available.

6.5 Non-Destructive Hyperfine State Discrimination

The ability to image without a repump beam as in [109] is experimentally tested as a precursor to performing non-destructive hyperfine state discrimination. This experiment requires the addition of an optical pumping and probe beam (for further details see section 7.1-7.2) along the transport axis. Optical pumping with a circularly polarised beam to drive σ^+ transitions allows the atom to be initialised in $|F = 4, m_f = 4\rangle$. The probe beam is orientated with the same polarisation as the optical pumping and thus will drive the closed transition $|F = 4, m_f = 4\rangle \rightarrow |F = 5, m_f = 5\rangle$. The power in the probe beam corresponds to $1I_{\text{sat}}$ and is detuned from the Zeeman shifted closed transition by $\Delta = -\Gamma$. A second image using only the probe beam to scatter photons is then taken with a duration of 30 ms with an applied field along the quantisation axis of 3 G. It should be noted that for this experiment the probe beam remains on constantly during the second image while the trapping light is chopped. This is simply due to limitation in available chopping channels on the experiment.

The data is then analysed based on an atom being present or not in the first

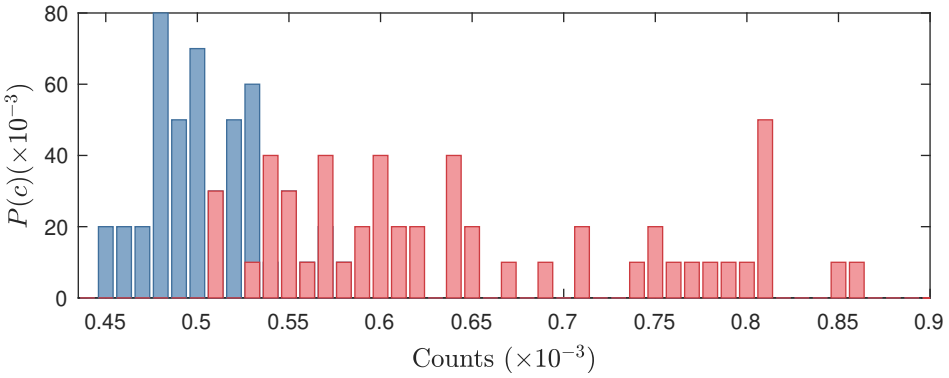

Figure 6.5: Readout using weak circularly polarised probe beam $I \sim I_{\text{sat}}/2$ detuned by $\Delta/2\pi = -\Gamma$ in the presence of a 3 G field to drive the cycling transition $|F = 4, m_f = 4\rangle \rightarrow |F' = 5, m_f = 5\rangle$, removing the need for repump light. Red counts correspond to incidences where the presence of an atom is detected in the first image and blue counts correspond to background scatter.

image. If an atom is not present in image 1 the counts registered on the camera for image 2 correspond to background scatter. If the atom is in the first image there is the potential to scatter light assuming optical pumping has worked effectively and the atom is still in $F = 4$. As can be seen in Fig. 6.5 there is a clear difference in counts reaching the camera between the two cases indicating the ability to distinguish between hyperfine states, however there is still a significant overlap in the distributions due to loss or decay to $F = 3$ during readout which would limit fidelity. This could be further improved by applying a larger bias field along the quantisation axis to further reduce off-resonant excitations which result in the atom becoming stuck in the dark state $F = 3$ as in [109] where an applied field of 20 G is used. Further to this, the uni-directional nature of the probe beam heats the atom and perhaps compromises retention therefore the addition of a mirror to retro-reflect will reduce heating during imaging.

Although limited these results show promising potential for future work with counts of over 300 above background being registered in the case of an atom being present, more than enough to discriminate with high fidelity.

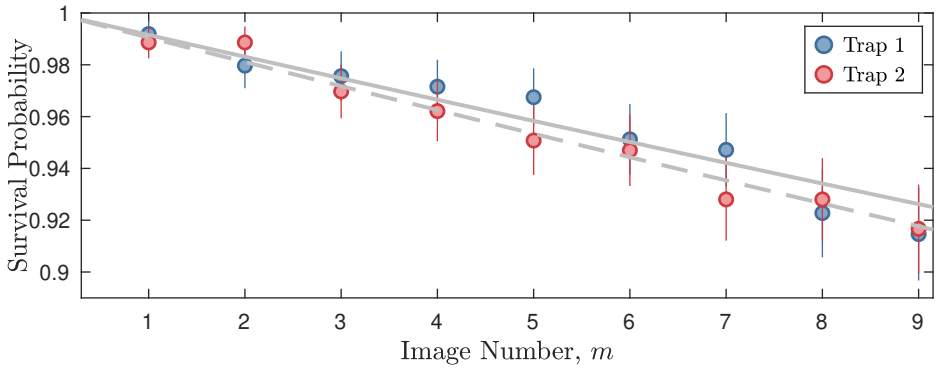

Figure 6.6: Single atom retention for multiple 40 ms measurements at -3Γ separated by 60 ms. The single shot retention α, is found to be $> 99\%$ for both traps when fitted to $P(m) = \alpha^m$. The total duration of this sequence following the initial detection image is 900 ms.

6.6 Characterisation of Single Atom Traps

6.6.1 Retention

Quantum gate operations not only require the ability to readout with high fidelity, but that the imaging process is non-destructive to avoid losing the atom from the trap corresponding to a high retention rate. To accurately determine the retention between measurements, 10 sequential imaging sequences each separated by 60 ms are performed. Following the 40 ms imaging pulse, the atoms are heated to 25 μK, so to aide retention a short 10 ms cooling cycle is added between images. It can be seen from Fig. 6.6 that the atom can be retained for many sequential images, from which a single shot retention $\alpha > 99\%$ in both traps is obtained from fitting data to $P = \alpha^m$, where m is the number of images and P is the survival probability. For comparison, measurement of the trap lifetime returns a $1/e$ lifetime $\tau = 8.7 \pm 0.2$ s (section 6.6.4) for both traps and a survival probability of 87% for trap 1 and 90% for trap 2 after 600 ms. These results indicate that the main limitation in the retention measurements is the background-limited lifetime of the atoms in the trap.

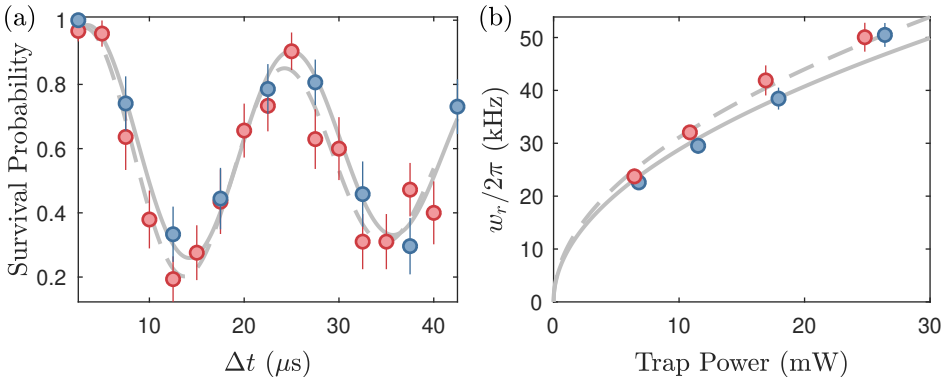

Figure 6.7: Double-drop method for trap frequency measurements. (a) Example oscillation observed in each trap for $t_1 = 20$ μs and $t_2 = 20$ μs fitting to a damped sine wave obtains $\omega_r/2\pi = 23.7 \pm 0.7, 23.2 \pm 0.9$ kHz (b) the obtained oscillation frequencies for various powers finding the waists to be $w_1 = 1.88 \pm 0.02$ μm and $w_1 = 1.81 \pm 0.01$ μm.

6.6.2 Trap Frequencies

As in the previous chapter measurement of the trap frequencies allows the waist to be determined and thus the trap depth. Due to the tighter focus the radial frequency is much higher than experienced in the transport trap making it harder to excite via parametric heating. Instead a different approach is used known as the double drop method [91, 125]. In this method the trap is dropped twice for durations t_1 and t_2 separated by a time Δt. The purpose of the first drop is to 'kick' the atom to increase it's oscillation amplitude at the bottom of the potential. The atom's survival of the second drop is then dependent on the delay between drops, revealing the oscillation frequency. The loss on the second drop entirely depends on the atoms location in the potential when the second drop occurs. if the atom is at the bottom of the trap it has a high probability of being lost as this is when the atom has it's maximum velocity. Likewise if the atom is at the extremity of it's oscillatory motion it is at its minimal velocity so is likely to survive. Due to the symmetric nature of the oscillation loss occurs at $2\omega_r$ when varying the delay between drops. Such an experiment is shown in Fig. 6.7(a) giving $\omega_r/2\pi = 23.7 \pm 0.7, 23.2 \pm 0.9$ kHz for the trap 1 and 2 respectively for 6.5 mW

of trapping power. This experiment is repeated for several trapping powers and the frequencies obtained shown in Fig. 6.7(b). Fitting this data finds the waists to be $w_1 = 1.88 \pm 0.02$ μm and $w_2 = 1.81 \pm 0.01$ μm. This discrepancy in spot size can be attributed to the slightly differing path length from the trap collimator to the aspheric lens for each trap.

6.6.3 Temperature

Temperature measurements on the single atom use the release-recapture method [126, 127] as time of flight measurements present several technical challenges without an image intensifier [113]. In this method the trap is turned off for a time Δt. The principle behind this is an atom with high energy is less likely to be recaptured by the trap after its free flight. Experiments are performed for several release durations and the temperature estimated from comparing the data to a Monte-Carlo simulation. The simulation is constructed as follows [127]; the atom within the trap has an initial position x_i and velocity v with standard deviations $\Delta x_i = \sqrt{k_B T/m\omega_i^2}$ and $\Delta v = \sqrt{k_B T/m}$. A random position-velocity vector is generated from these initial distributions assuming a Maxwell-Boltzmann distribution for temperature T. The trajectory and position of the atom is then calculated for a free flight time Δt, and the kinetic energy of the atom in the trap potential is then calculated. If this is greater than $U(r)$ the atom is removed from the trap. Many trajectories are simulated for each time step for different initial position-velocity vectors to construct an average survival probability. Comparison experiment data is performed through χ^2 minimisation to obtain a fit by repeating simulations for various temperatures.

Single atom cooling via PGC can typically cool the atom to around 10-20 μK [127, 128], as shown in Fig. 6.8(a). Further cooling can be achieved through an adiabatic lowering of the trapping potential following a scaling

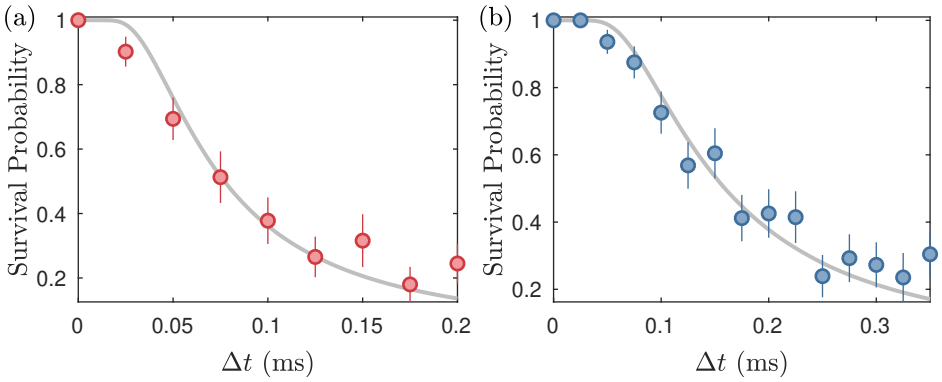

Figure 6.8: Release-recapture measurement (a) after cooling via PGC at $U_0 = 1.8$ mK reaching $T = 16 \pm 2$ μK and (b) after adiabatic lowering of the trapping potential from $U_i = 1.8$ mK to $U_0 = 300$ μK following PGC achieving a temperature of $T = 3.4 \pm 0.4$ μK

law given by [127]

$$T/\sqrt{U_0} = T_i/\sqrt{U_i}, \tag{6.6}$$

where T_i and U_i are the initial temperature and trap depth before potential is changed. Fig. 6.8(a) presents data where cooling is performed with PGC alone at a trap depth of $U_0 = 1.8$ mK where the cooling cycle is 10 ms long following the first image using a detuning of $\Delta = -5\Gamma$ and intensity of $I = 0.5I_{\text{sat}}$ per beam. A temperature of $T = 16 \pm 2$ μK is obtained through radiative cooling alone. Adiabatic ramping of the potential is performed after this PGC phase by lowering the intensity over 10 ms to reduce the trap potential from $U_i = 1.8$ mK to $U_0 = 300$ μK. Using an initial temperature of $T_i = 16$ μK the expression in Eq. 6.6 predicts that this should further cool the atoms to 6 μK. The resulting release-recapture measurement for this method is shown in Fig. 6.8(b) where a temperature of $T = 3.4 \pm 0.4$ μK is obtained in reasonable agreement with the predication yielded from the above relation. Further cooling to the vibrational ground state can be achieved through Raman sideband cooling [129–131] this also offers the ability to optically pump while cooling.

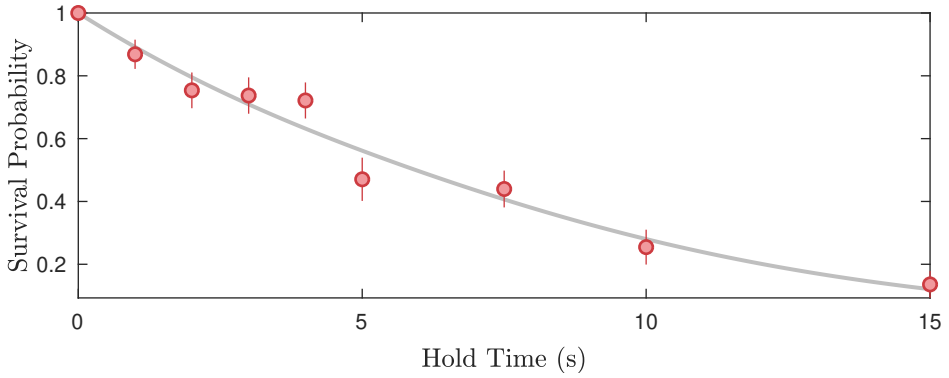

Figure 6.9: Single atom lifetime measurement, fitting to $P(t) = P_1(t) \cdot P_2(t)$ extracts a $1/e$ lifetime of $\tau = 8.7 \pm 0.2$ s and heating rate of $\alpha = 18 \pm 1$ μK/s)

6.6.4 Lifetime

Similar to the optical transport trap, the lifetime can be deduced from holding the atoms in the tweezers and monitoring the decay of the survival probability. As there is only one atom in the trap two body losses do not factor into the lifetime and trap loses will be primarily due to collisions with residual gases with an exponential decay in survival expected $P_1(t) = \exp(-t/\tau)$. However the atom can also escape the trap if it is heated sufficiently by the trapping beam during the hold time. Assuming this heating rate, α is linear over time the survival probability due to heating is [93]

$$P_2(t) = 1 - \exp\left(-\frac{U_0}{k_B(T_0 + \alpha t)}\right)\left(1 + \frac{U_0}{k_B(T_0 + \alpha t)} + \frac{U_0^2}{2k_B^2(T_0 + \alpha t)}\right) \quad (6.7)$$

where T_0 is the initial temperature. The data shown in Fig. 6.9 represents an experiment performed with a trap depth of U_0 =1 mK where the time the atom has been held in the trap is varied, the initial temperature in this instance is $T_0 = 15$ μK. Fitting this data with these constraints to $P(t) = P_1(t) \cdot P_2(t)$ gives a lifetime of $\tau = 8.7 \pm 0.2$ s and finds the heating rate to be $\alpha = 18 \pm 1$ μK/s. These results present an excellent basis for experiments to be performed with the lifetime far exceeding any gate sequence and a minimal heating rate.

6.7 Conclusion

Single atom imaging using an sCMOS camera with high fidelity has been demonstrated with the ability to perform atom detection with small error $\epsilon < 8 \times 10^{-7}$) and perform multiple non-destructing measurements with high retention $> 99\%$ in two spatially resolved optical traps. In addition to this imaging without repumper light has been demonstrated as a precursor to non destructive hyperfine discrimination. Despite the limited QE of the camera at the imaging wavelength the performance is comparable to experiments using costly EMCCD based detectors with a superior SNR possible at the intermediate photon count rates. This technology offers a viable, cost-effective alternative to other currently used techniques in low photon detection, and has the additional benefits of a larger sensor size and the ability to independently readout single pixels with the high-speed integrated FPGA hardware for performing scalable quantum state detection.

Further to this single atom characterisations have been carried out to calculate the single atom trapping frequencies, temperature and lifetime as well as initial experiments showing a future potential to perform non-destructive state readout. The results of these measurements indicate an excellent environment for performing qubit rotations with long coherence times hopefully possible due to the cold atomic temperature and low retention losses.

Part IV

Qubit Operations

Chapter 7

Ground State Operations on a Single Atom

Transitions between the hyperfine states of alkali atoms have routinely been carried out through the use of microwaves and, in fact, form the basis of frequency standards across the world [132]. Coherent oscillations using microwaves, however, are restricted to slow Rabi frequencies due to the inability to focus the microwave source to achieve desired intensities and the weak magnetic dipole matrix element. However, long coherence times are achievable with single atoms isolated in a dipole trap [133]. Optical couplings can achieve much faster rotations due to the much stronger electric dipole transitions and offer the ability to focus laser light down to small sizes to achieve addressability. Fast ground state rotations are therefore realisable through two photon transitions. Rabi flopping via this two photon process was demonstrated by the Saffman group in 2006 using single atoms in microscopic tweezers achieving $\Omega/2\pi = 1.36$ MHz and a dephasing time of 870 μs [59]. This measurement provides a benchmark for achievable performance by allowing optimisation of optical pumping and characterisation of the addressing beams.

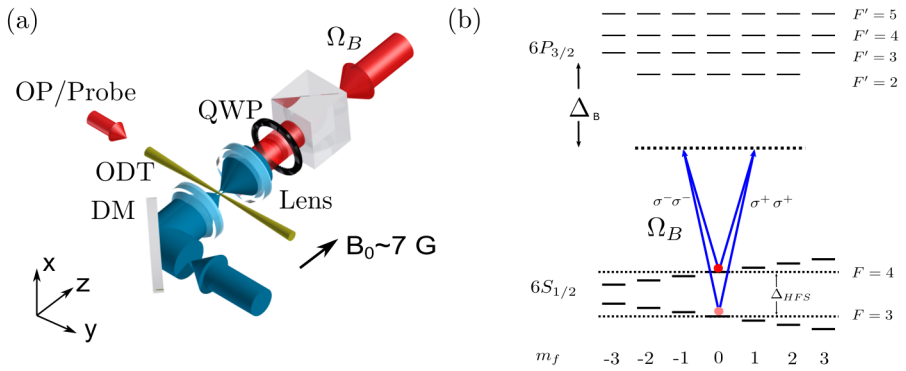

Figure 7.1: (a) Schematic of set-up for ground state rotations. An optical pumping and probe (blow-away) beam coupled into the same fibre are aligned along the y axis with a waist of around 500 μm. The Qubit B beam is focused to $w_B = 4.5$ μm and is circularly polarised and a bias field along y applied to drive σ^- transitions. (b) Level diagram for ground state rotations showing both possible orientations from the clock state. Rotations are performed with a large detuning to minimise scatter from the intermediate state $|\Delta|/2\pi >$ 30 GHz

7.1 Hyperfine Discrimination

Key to performing ground state rotations is the ability to determine what state the atom is in. This is performed through a destructive measurement where the single atom is exposed to light resonant on the $F = 4 \rightarrow F' = 5$ transition by a uni-directional blow-away beam that is directed down the y-axis perpendicular to the optical tweezers as shown in Fig. 7.1(a). When the atom is in the upper hyperfine state it is heated out of the trap, hence atoms that remain in the trap are in the state $|0\rangle = |6S_{1/2}, F = 3\rangle$. The beam has a waist of $w_{\mathrm{BA}} = 500$ μm and the power is 20 μW corresponding to $I \sim 2I_{sat}$. Effective fidelity in determination between the states is achieved with a lower trap depth $U_0 = 300$ μK which reduces the heating required to lose the atom from the trap. The trap is chopped on and off at 1 MHz to removed associated light shifts, however the blow-away beam remains on constantly.

Fig. 7.2 shows the results of state discrimination for when the atom is pumped into either hyperfine state. The survival probability when pumped into $F = 3$

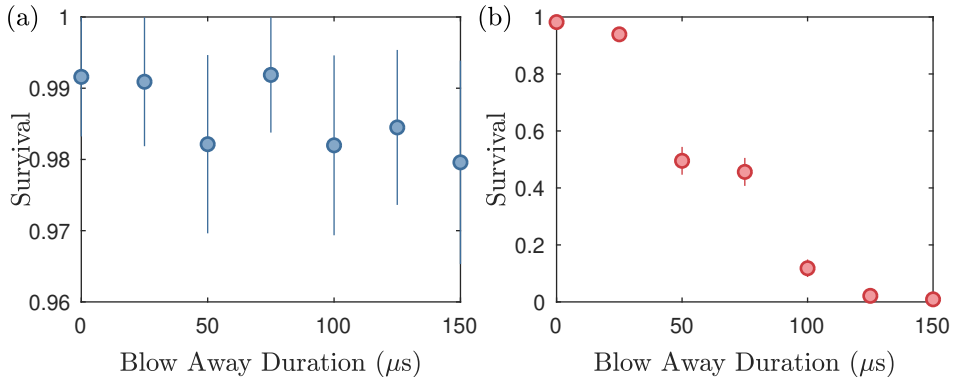

Figure 7.2: Atom Retention after state discrimination protocol for when (a) pumped into F=3 and (b) pumped into F=4.

approaches 1 and the error is found to be the result of a small retention error in the sequence not associated with the blow-away beam. In the case when the atom is pumped into $F = 4$ almost a complete loss of the atom is seen after 150 μs with a 1 % error that an atom in $F = 4$ survives the blow-away pulse. In order to prevent depumping from $F = 4$ into $F = 3$ due to leakage light from the blow-away beam it is necessary to use a mechanical shutter at all times out-with state discrimination protocol. It is found that this method is around 99% effective in determining hyperfine state.

This process could be adapted in the future to achieve non-destructive discrimination through using large bias fields, deep traps and high purity circularly polarised light to scatter photons on the cycling transition during readout as recently demonstrated in [109]. Results presented in section 6.5 show that this could possibly be implemented with the Zyla camera offering the necessary sensitivity, however current optical axis prevents implementing the necessary retro-reflecting mirror on the probe beam to reduce heating and perform with high fidelity.

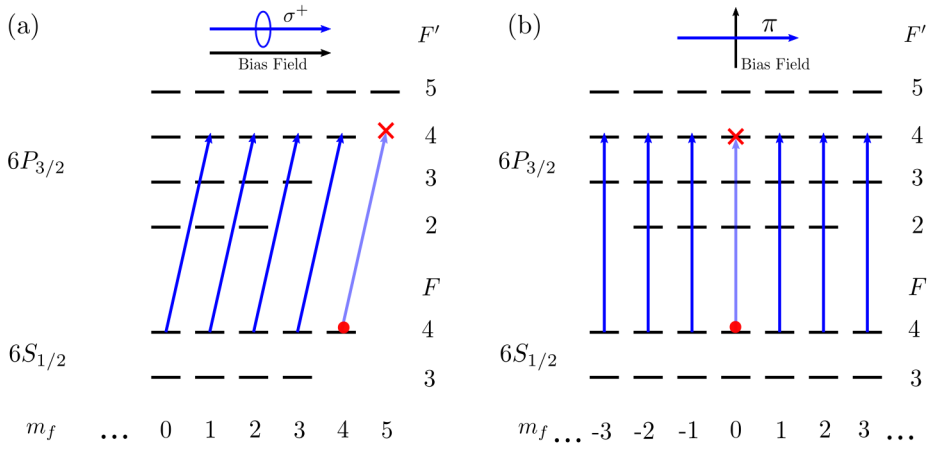

Figure 7.3: Available optical pumping schemes for the experiment, (a) stretched state and (b) clock state. In both schemes the atom will eventually spontaneously decay into a dark state not coupled by the light fields due to angular momentum selection rules.

7.2 Optical Pumping

The ability to readily initialise a qubit's quantum state is essential to quantum information processes [20]. For coherent operations this requires to not only pump into a discrete hyperfine state but also into a specific Zeeman magnetic sub-level. With the current laser systems there exist three states which can be readily initialised, utilising what is known as dark state pumping. They are the magnetically insensitive state $|F = 4, m_f = 0\rangle$, known as the the clock state and $|F = 4, m_f = \pm 4\rangle$, known as the stretched states Fig. 7.3.

Pumping into these states is achieved though a weak uni-directional beam derived from the cooling laser resonant on the $|6S_{1/2}, F = 4\rangle \rightarrow |6P_{3/2}, F' = 4\rangle$ transition along the same path as the blow-away beam with repump light sourced from the molasses beams used for imaging to prevent occupation of $F = 3$. The polarisation and bias field applied during pumping are dependent on desired target state.

The optical pumping beam passes through a Glann-Taylor polariser to achieve high-purity horizontally polarised light. Pumping into the clock state

is then achieved by applying a bias field along the y-axis (see Fig. 7.1a)) to drive π transitions. The π polarised light only drives transitions where $\Delta m_f = 0$, but the spontaneous decay is random $\Delta m_f = -1, 0, 1$. However the $|F, m_f = 0\rangle \rightarrow |F', m_f = 0\rangle$ transition is forbidden due to angular momentum selection rules creating a dark state to accumulate in as can be seen in Fig. 7.3(b). Stretched-state pumping requires the addition of a $\lambda/4$ waveplate and a bias field applied along the optical pumping axis to drive σ^+ or σ^- transition as in Fig. 7.3(a). Like clock state pumping a dark state is eventually reached where the light fields no longer couples to another state.

7.3 Ground State Rotation Laser System

The master laser used to drive ground state rotations -Qubit B- uses the same design as used for the cooling and repump lasers detailed previously. The laser is detuned $\Delta/2\pi$=-88 GHz from the $6S_{1/2} \rightarrow 6P_{3/2}$ transition and is passed through an Electro-Optic Modulator (EOM) to generate side-bands $\pm$4.6 GHz at half the ground state hyperfine splitting, $\omega_{HFS}/2\pi = 9.192631$ GHz [81]. Suppression of the carrier frequency and second order sidebands is achieved using an Haubrich-Dornseifer-Wynands interferometer [134] yielding > 95 % of the amplitude equally shared between the two first order side-bands. This is then passed through a 80 MHz AOM to enable fast switching of the light fields before coupling into a single mode polarization maintaining fibre taking the light over to the experiment.

7.3.1 Qubit B Alignment

Alignment of the Qubit B light is achieved through coupling the 1064 nm trapping light for the desired microtrap into a single mode fibre and optimising the collimator focus for the 1064 nm light. The 852 nm Qubit B light is then back-coupled along this beam path and then fine-tuned onto the target

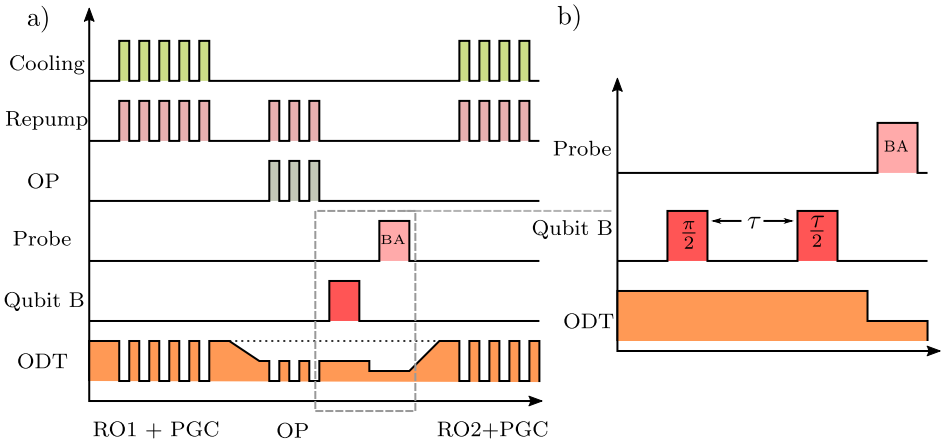

Figure 7.4: Pulse sequences used for ground state rotation for Cooling, Repump, Optical Pumping (OP), blow-away (BA) Probe and Optical Dipole Trap (ODT) from the verification readout (RO1) to measurement readout (RO2) (a) Standard sequence for experiment the dashed line on the ODT represents the sequence used in some experiments before full optimization (b) Example of the pulse sequence used for Ramsey interferometery where two $\pi/2$ pulses are separated by a time,τ.

atom by applying resonant light to cause loss of the atom from the trap. This method verifies that optimal alignment can be achieved by simply aligning the Qubit B focus onto the same pixel as the trapped atom on the camera. Imaging this on the camera and using the calculated magnification of the imaging system gives a waist of $w_B = 4.5 \times 4.3$ μm in the focal plane of the atoms.

7.4 Ground State Rotations

The trap depth is set to $U_0 = 2$ mK for imaging and loading. Following the first image to determine the presence of an atom, the atom is cooled via a PGC stage as outlined in section 6.6.3. The trap depth is then adiabatically lowered over a duration of 10 ms to $U_0 = 1$ mK where optical pumping into $|1\rangle = |4, 0\rangle$ is performed. This reduction in trap depth allows for better extinction of trapping light when chopping. Following completion of optical pumping the trap depth is then reduced again to $U_0 = 0.3$ mK over 10 ms to

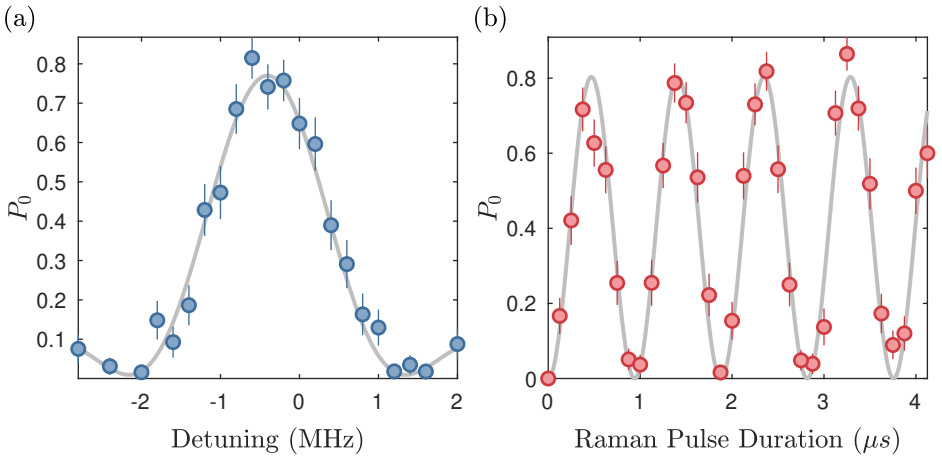

Figure 7.5: Raman ground state rotation of a single atom (a) Spectroscopy of the transition with the duration fixed to 500 ns data is fitted to Eq. 7.1 giving a resonance of -410 kHz (b) Flopping with the detuning fixed to resonance from the unshifted resonance (verified against GPS clock) obtaining $\Omega/2\pi = 1.06$ MHz

further cool the atom. All light to the experiment apart from the trapping light is then extinguished via mechanical shutters before applying the Qubit B pulse. The state detection protocol then follows with the blow-away beam applied for 0.5 ms. The trap is then ramped back to $U_0 = 2$ mK over a period of 10 ms and another PGC stage is initialised before the second image is taken. A schematic of the pulse sequence used is shown in Fig.7.4(a).

In order to obtain good coherence and prevent driving to other states it is necessary to lift the degeneracy of the m_f levels by a differential shift larger than the two-photon Rabi frequency. This is achieved by applying a bias field of 7 G along the quantisation axis, to drive either σ^+ or σ^- transitions depending on the handedness of the input circular polarisation. As the two addressing fields have not been separated and are contained in the same beam, the transitions that can be driven are restricted to $\Delta m_f = 0$, as shown in Fig. 7.1(b). The sign of the differential AC Stark shifts induced by the addressing light are dependent on the driving polarisation; σ^+ transitions counteract the shift from the applied magnetic field reducing the separation of m_f levels, therefore it is more constructive to use σ^- transitions.

Two photon spectroscopy of the transition is performed by applying the pulse for the expected π time and scanning the frequency of the microwave source used to generate the side-bands. Rabi flopping is then simply performed at resonance and scanning the pulse duration.

Fig. 7.5(a) depicts one of the first spectroscopy obtained in the laboratory before full optimisation of optical pumping using a pulse duration of t_π = 500 ns and a power of 45 μW. This is fitted to

$$P_0 = \frac{\Omega^2}{\Omega^2 + \delta^2} \sin^2 \left(\sqrt{\Omega^2 + \delta^2} \frac{t}{2} \right), \tag{7.1}$$

with the time constrained to the duration of the pulse, finding the shifted resonance due to the differential AC Stark shift to be $\delta_{\mathrm{AC}}/2\pi$ = -410 kHz. Fig. 7.5(b) shows the Rabi flop obtained upon sitting on this resonance and is fitted to Eq. 4.23 finding a flopping rate of $\Omega/2\pi$ = 1.06 MHz. Repeating these measurements for different driving powers allows the beam waist at the atom to be extrapolated, AC stark shift measurements obtain a waist of w_B =4.6±1 μm and Rabi flopping measurements indicate w_B =4.4 ± 0.4 μm in excellent agreement with each other and the predicted waist from imaging.

7.5 Optimisation of Clock State Pumping

Data in the previous section uses a 4 G bias field for optical pumping attaining a peak transfer of around 80 %, limited by the optical pumping preparation fidelity. Further optimisation is performed with an applied field of 1.5 G and scanning the shim fields for population transfer at the π time. The preparation fidelity can be calculated by comparing the optical pumping time to the the time it takes an atom to be depumped from the clock state with only the optical pumping light on [135]. The data from these measurements is presented in Fig. 7.6(a) and (b) fitting this data to $-A\mathrm{exp}(-\mathrm{t}/\tau)+\mathrm{B}$ time constants of τ_{DP} = 9 ms and τ_{OP} = 390 μs are obtained for the depumping

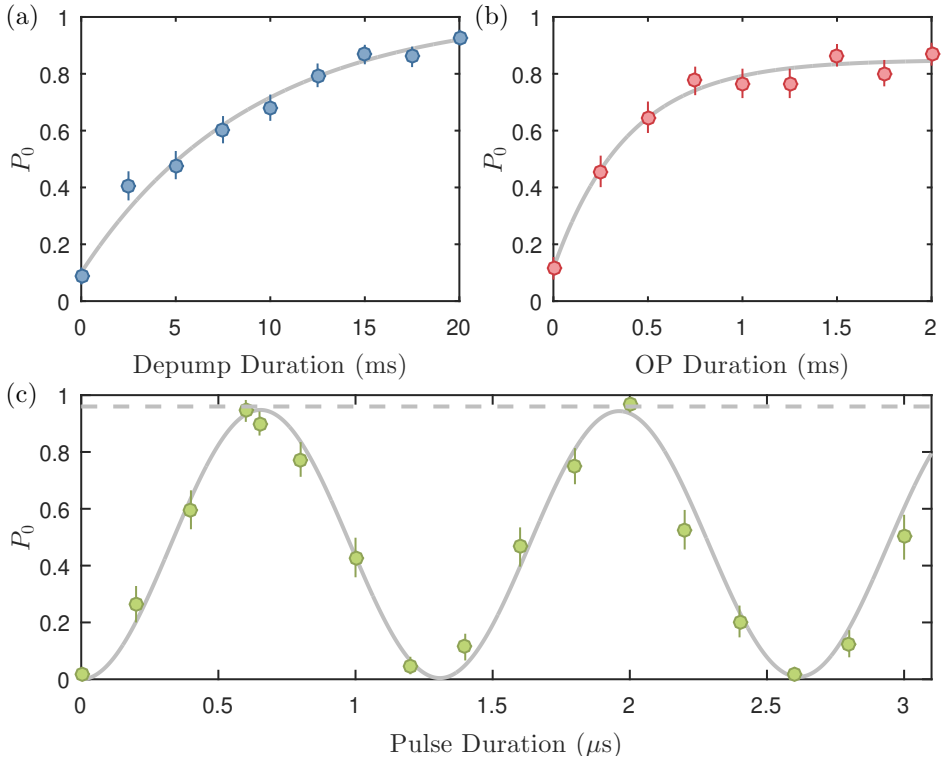

Figure 7.6: Optical Pumping Optimization, (a) depump duration and (b) optical pumping duration (c) Ground state Rabi Flop upon optical pumping optimization, dashed line indicates $\mathcal{F}_{\mathrm{OP}}$.

and pumping times respectively. The optical pumping fidelity is then found via the relation

$$\mathcal{F}_{\mathrm{OP}} = 1 - \frac{1}{\tau_{\mathrm{DP}}/\tau_{\mathrm{OP}}}, \tag{7.2}$$

giving $\mathcal{F}_{\mathrm{OP}} = 0.96$ for the optical pumping fidelity. A Rabi flop with these optimised settings and an optical pumping duration to 4 ms to ensure complete pumping is shown in Fig. 7.6(c). As can be seen a far greater contrast is obtained than previously with almost perfect transfer between the hyperfine states obtained, indicating good optical pumping fidelity.

Preparation fidelities could be further improved through optically pumping on the D_1 transition $6S_{1/2}, F = 4 \rightarrow 6P_{1/2}, F' = 4$ where there is less levels to off-resonantly couple to and a larger separation between hyperfine states, where fidelities $\mathcal{F}_{\mathrm{OP}} > 0.99$ have been observed [67].

7.6 Calibration of Applied Magnetic Fields

In order to accurately determine the applied field the atom experiences from the bias coils, transitions using magnetically sensitive states can be monitored as a function of applied current to the coils. Due to the configuration of the Raman beams, transitions are limited to $\Delta m_f = 0$, therefore performing transitions from $|4,4\rangle$ with a well defined field is not possible, and with $|4,0\rangle$ being magnetically insensitive both of the preparation states are not suitable for this measurement. Pumping into $F = 3$ or $F = 4$ using the repump or cooling light before applying a bias field randomly prepares across the sub-levels yielding preparation populations of 1/7 and 1/9 depending on the hyperfine state. This, however, does not present a large enough signal to measure accurately. Instead a new pumping scheme is implemented based on spontaneous emission. The atom is initially prepared in $|4,4\rangle$ using circularly polarised optical pumping light and a bias field along the OP axis with repump. Following preparation the repump light is extinguished and the optical pumping light remains on. In a well defined field depumping to F=3 should only occur due to off-resonant processes and should favourably populate $|3,2\rangle$ and $|3,3\rangle$. The time until the population has fully depumped into $F = 3$ is measured to be around 10 ms.

Implementing this scheme into the sequence requires a rotation of fields after optical pumping turning on the field along z-axis before turning off the field along the y-axis to remain pumped, otherwise the procedure remains the same. Spectroscopy is performed with a pulse duration of 1 μs and the detuning from resonance is now $\Delta/2\pi = 119$ GHz, the power of the Qubit B beam is 30 μW. As shown in Fig. 7.7(a) there is now two distinct peaks corresponding to the $|3,3\rangle \rightarrow |4,3\rangle$ and $|3,2\rangle \rightarrow |4,2\rangle$ transitions. Tracking the relative frequency shift between these peaks allows calibration of both the x-bias and x-shim field coils by comparing to theoretical expected values. The energy separation of the zeeman sub-levels from an applied magnetic

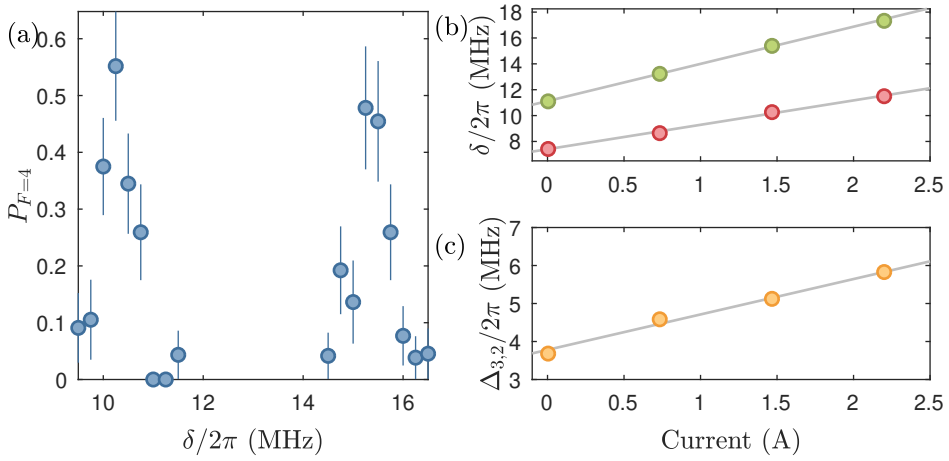

Figure 7.7: Applied magnetic field calibration (a) The two resonances for $|3,3\rangle \rightarrow |4,3\rangle$ and $|3,2\rangle \rightarrow |4,2\rangle$ transitions (b) The change in resonance frequency for the two transitions red points correspond to $|3,3\rangle \rightarrow |4,3\rangle$ and blue to $|3,2\rangle \rightarrow |4,2\rangle$ (c) The relative shift between the two transitions.

field is given by

$$\Delta E_{f,m_f} = m_f g_f \mu_B B \tag{7.3}$$

the differential shift is thus given by $\delta_B = \Delta E_{F=4,mf} - \Delta E_{F=3,mf}$. The Landé g-factor for the ground hyperfine states of caesium is $g_f = 0.25$ for $F = 4$ and $g_f = -0.25$ for $F = 3$ hence the $|3,2\rangle \rightarrow |4,2\rangle$ ($|3,3\rangle \rightarrow |4,3\rangle$) transition is expected to shift by 2.1 MHz/G (2.8 MHz/G). Thus the separation between the peaks should scale as 0.7 MHz/G. Analysing the data for different applied magnetic fields strengths finds that the x-bias coil provides 0.9 ± 0.1 G/A providing a bias field of 4.6±0.5 G with the maximal available current 4.97 A. Fig. 7.7 (b) and (c) show the calibration of the x-shim coil when the x-bias field is at maximum field. It is found that it provides 1.3 ± 0.1 G/A and at the maximum available current (2.2 A) provides a bias field of 2.9 ± 0.2 G. Therefore running both coils at full capacity, as has been done throughout the previous measurements yields an applied field of 7.5 ± 0.5 G.

7.7 Ground State Phase Accumulation

The accumulated phase of the Qubit can be measured using Ramsey interferometry. After the application of a $\pi/2$-pulse the atom is in a superposition state, the same as the Hadamard operation given in Eq. 2.7. Once in the superposition state it is free to rotate around the z axis of the Bloch sphere. The resulting state after a second $\pi/2$ pulse is therefore dependent on the phase accumulated. Changing the free evolution time, τ between the two pulses results in what are known as Ramsey fringes [84]. The frequency of these fringes corresponds to the detuning from resonance and differential shifts the atom experiences during the free evolution time

$$\omega_{\text{Ram}} = \delta + \delta_{L-S} + \delta_B, \tag{7.4}$$

where δ is the two-photon detuning, δ_{L-S} is the differential shift due to the trapping field and δ_B is the shift due to the quadratic Zeeman effect. Thus performing this experiment on resonance presents information of the trapping field and applied magnetic bias. The quadratic Zeeman shift of the $|4,0\rangle \rightarrow |3,0\rangle$ transition is 430 Hz/G^2 [81] for a 7.5 G field this corresponds to $\delta_B/2\pi$ =24.2 kHz. The differential AC Stark shift experienced due to the trapping light is small and is due to the different relative detunings from each hyperfine state and equates to [133]

$$\hbar\delta_{L-S} = U_0(\Delta_{\text{eff}}) - U_0(\Delta_{\text{eff}} + \omega_{\text{HFS}}). \tag{7.5}$$

The previously outlined experiment is performed on the single atom using a $t_\pi/2$ = 300 ns on resonance. This measurement was performed before full optimisation of the procedure and the trap depth for imaging, optical pumping and rotation is U_0 = 3.2 mK. This gives a differential shift of $\delta_{L-S}/2\pi$ =-8.92 kHz, therefore expect the Ramsey fringes to be $\omega'_{\text{Ram}}/2\pi$ = $\delta_{L-S} + \delta_B$ = 15.3 kHz. Fig. 7.8(a) shows the results from the measurement.

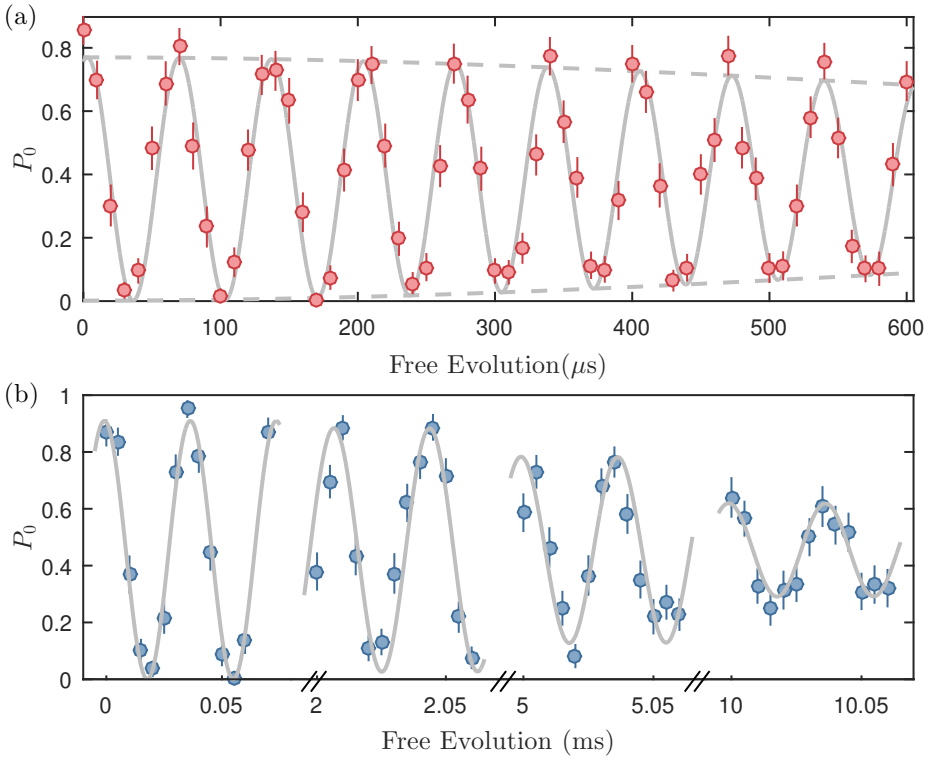

Figure 7.8: Ramsey interferometry of the ground state phase accumulation from inhomogeneous dephasing mechanisms for (a) $U_0 = 3.2$ mK, T≈60 μK and (b) $U_0 = 300$ μK, T=10μK. Fitting to Eq. 7.6 gives $\omega_{\mathrm{Ram}}/2\pi = 14.895 \pm 0.03$ kHz and $T_2^* = 1.36 \pm 0.2$ ms for the first dataset and $\omega_{\mathrm{Ram}}/2\pi$ =26 kHz and $T_2^* = 10 \pm 1$ ms for the second dataset.

To fit this data the method employed in [133] is followed and the data is fitted to

$$P_{3,\mathrm{Ram}} = B + A\left[1 + 0.95\left(\frac{t}{T_2^*}\right)^2\right]^{-3/2} \times \cos(\omega_{\mathrm{Ram}} t + \phi). \qquad (7.6)$$

Where A and B correspond to the initial amplitude and an offset respectively, ω_{Ram} is the frequency of the fringes and the T_2^* decay constant is the inhomogeneous dephasing time. From this fit the frequency of the oscillation is found to be $\omega_{\mathrm{Ram}}/2\pi = 14.9 \pm 0.03$ kHz, which is slightly smaller than expected for a phase accumulation due to the trapping field and quadratic Zeeman shift. However, it is still within the tolerance of the calibrated applied magnetic fields. The inhomogenous dephasing time is found to be $T_2^* = 1.4 \pm 0.2$ ms.

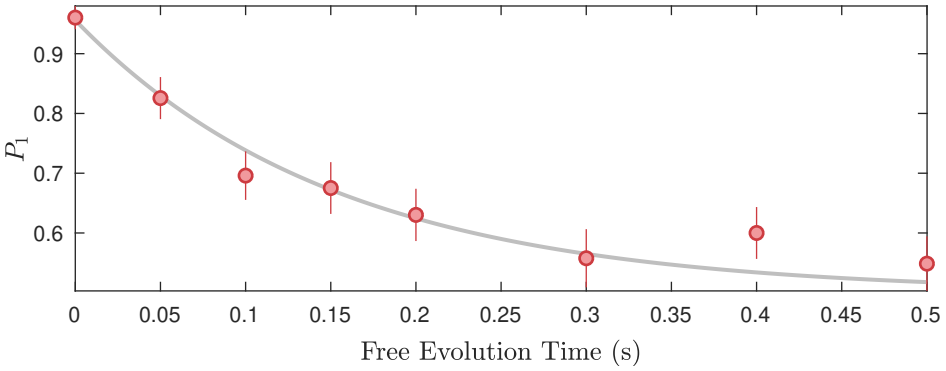

Figure 7.9: Ramsey Spin-Echo sequence to measure the irreversible dephasing of the qubit, fitting gives $T_2' = 150 \pm 20$ ms

The correlation between T_2^* and the atom temperature is given by [133],

$$T_2^* = 0.97 \frac{2\hbar}{\eta k_B T} \tag{7.7}$$

where η is a scaling factor from relating the hyperfine splitting and effective trapping laser detuning, $\omega_{\mathrm{HFS}}/\Delta_{\mathrm{eff}}$ for the laser parameters used this is calculated to be 1.57×10^{-4}. Using the fitted T_2^* and rearranging Eq. 7.7 the corresponding atom temperature is found to be 70 μK in good agreement with the expected temperature for the given trap depth (release-recapture measurements indicate a single atom temperature of $T \sim 60$ μK for the $U_0 = 3.2$ mK after optical pumping). Following further optimisation of the experiment, temperatures of 10 μK after optical pumping became realisable when adiabatically ramping the trap depth down to $U_0 = 300$ μK. The results from a Ramsey experiment using these parameters with $t_\pi/2 = 330$ ns are shown in Fig. 7.8(b). For such a low trap depth the differential shift from the trap beam is small ($\delta_{L-S}/2\pi$ =800 Hz) therefore the frequency of the Ramsey fringes is expected to be 24 kHz primarily due to the quadratic Zeeman effect. The ascertained frequency is found to be 26 kHz within the error of the field calibration and the dephasing time found to be $T_2^* = 10 \pm 1$ ms, in excellent agreement with Eq. 7.7 which predicts $T_2^* = 9.4$ ms for a temperature of $T = 10$ μK.

7.8 Homogenous Dephasing

The effects due inhomogeneous mechanisms can be recovered through the application of a π-pulse to reverse the decay in between the two $\pi/2$-pulses. This method is known as spin-echo [133] presents a measurement of the homogenous dephasing time T_2'. The measurement is performed with $U_0 = 300$ μK and with a single atom temperature of 10 μK. The $\pi = 675$ ns pulse is placed directly inbetween the $\pi/2$ pulse with the free evolution time either side corresponding to $t/2$. For no free evolution time this corresponds to a 2π-rotation on the qubit and results in the atom populating $F = 4$. As the free evolution time decreases this will eventually decrease to 0.5 as irreversible dephasing dominants. The results of this measurement are presented in Fig. 7.9 and fitting to $P_1 = A\mathrm{exp}(-\mathrm{t}/\mathrm{T}_2') + 0.5$, obtaining $T_2' = 150 \pm 20$ ms.

7.9 Conclusion

Fast optical Raman ground state rotations have been demonstrated on a single atom. This has allowed thorough optimisation and characterisation of optical pumping achieving a clock state pumping fidelity of $\mathcal{F}_{\mathrm{OP}} = 0.96$ as well as calibration of applied magnetic fields before attempting two photon transitions to the Rydberg state. Coherence times in excess of 10^4 times longer than the $\pi/2$ pulse in Ramsey spectroscopy have been observed with over 10^5 possible with recovery of homogenous dephasing mechanisms via a π pulse. The transitions demonstrated can be used in conjunction with the Rydberg lasers to demonstrate a mesoscopic gate as outlined in [136].

Chapter 8

Rydberg Rabi Flopping

Due to the weak dipole matrix elements excitation to the Rydberg state generally requires a two-photon excitation scheme, although single photon single photon excitation has been demonstrated [137]. Rotations to the Rydberg states require well stabilised lasers to minimise gate errors. This is achieved using a high finesse ultra low expansion (ULE) cavity to obtain sub-kHz linewidth with a measured linear frequency drift of $\sim$1 Hz/s [138] . Further details of the ULE system and lasers can be found in the thesis of R. Legaie whose PhD work ran cocurrently with the data presented in this thesis. This chapter presents work demonstrating excitation to the Rydberg state.

8.1 Rydberg State Detection

State detection of Rydberg atoms utilises the anti-trapping potential that a Rydberg atom experiences due to the dipole trapping beam. Rotations are performed in free space with no potential before the tweezers are restored to detect/recapture the atom. A key requirement for this to work effectively is that the Rydberg lifetime τ_{Ryd}, is large compared to the time it takes the atom to leave the trapping region τ_r. For $n > 50$ the error associated with this detection scheme is $e_{\mathrm{D}} = \tau_r/\tau_{\mathrm{Ryd}}$ [139]. As the Rydberg lifetimes scales

as $\tau_{\mathrm{Ryd}} \propto n^2$ it is desirable to work at high n to increase detection efficiency, however as will be shown in this chapter τ_r can also be controlled through the recapturing trap depth.

The measured quantity using this method is the probability of being in the ground state P_g it is inferred that the Rydberg population corresponds to $P_r = 1 - P_g$ however due to errors with detection, optical pumping efficiency (e_{OP}) and false-positives (e_{F}, atoms which are lost from the trap when the trapping potential is off not due to Rydberg excitation) this differs slightly to the actual Rydberg population, $\tilde{P}_r$ such that [139]

$$P_r = e_{\mathrm{F}} e_{\mathrm{OP}} + (1 - e_{\mathrm{OP}})\big[e_{\mathrm{F}}\tilde{P}_g + (1 - e_{\mathrm{D}} + e_{\mathrm{D}} e_{\mathrm{F}})\tilde{P}_r\big]. \tag{8.1}$$

Due to the cold atomic temperature, 10 μK and good background pressure the error associated with false positives is small (e_{F}<0.01). From the previous chapter it was found that the clock state preparation error is $e_{\mathrm{OP}} = 1 - \mathcal{F}_{\mathrm{OP}} = 0.04$. A measurement of the detection error will be presented later in this chapter. However as a guide the Parisian group of Antoine Browaeys obtain $e_D \approx 0.05$, factoring these errors in suggest that a measured Rydberg population of $P_r = 0.9$ should be possible.

8.2 Excitation Scheme

Excitation to the Rydberg state is achieved using the two photon ladder system outlined in Sec. 4.1, Parity rules restrict excitation to only a nS or nD state. Unlike the ground state rotations presented in the previous chapter, two separate excitation lasers are used; a 852 nm laser exciting from the ground state, $|g\rangle = |6S_{1/2}, F = 4\rangle$ to the intermediate state $|e\rangle = |6P_{3/2}, F = 5\rangle$ and a laser at 509 nm coupling $|e\rangle$ to the Rydberg state, $|r\rangle$. The lasers used to drive the Rydberg rotations are stabilised using a ULE

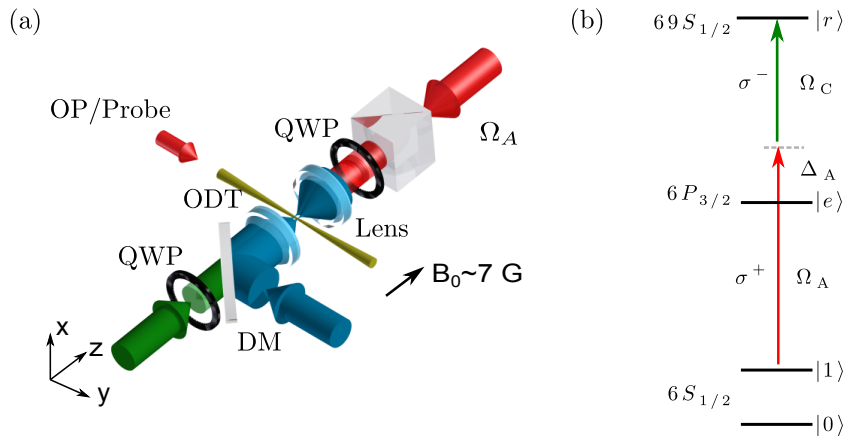

Figure 8.1: (a) Rydberg laser setup counter propagating beams minimises Doppler shifts, beams are focused to $w_A = 14.6$ μm for Qubit A and $w_B = 18$ μm for the Rydberg laser. (b) Excitation scheme to $69S_{1/2}$ using $\sigma^+\sigma^-$ configuration, the detuning from $F' = 5$ is $\Delta/2\pi = +871$ MHz.

cavity to obtain sub-kHz laser line-widths [138].

Light at 509 nm is sourced from two interchangeable lasers Rydberg A and B. The master source for these lasers is a 1018 nm AR-coated laser diode (Toptica LD1020-0400-2 and Sacher SAL-1030-060, respectively). This light is then passed through a tapered amplifier to obtain the necessary high power required for Rydberg excitation due to weak dipole matrix element for $|e\rangle \rightarrow |r\rangle$. This then passes through a home-built second harmonic generation cavity to generate light at 509 nm. When operating at peak capacity up to 125 mW of green light can be obtained on the experiment table. The 509 nm intensity is stabilised using a single pass 80 MHz AOM in conjunction with a homemade PID control circuit to modulate the dumped light in the first order of the diffracted light from the AOM. The source of light at 852 nm, Qubit A is obtained from an ECDL laser similar to that used to drive ground state rotations.

Due to the free spectral range of the ULE cavity,$\sim$ 1.5 GHz there are boundaries to accessible states, and the detuning from the intermediate state. The Qubit A laser is locked to a cavity mode detuned from $|6P_{3/2}, F = 5\rangle$ by $\Delta/2\pi = +1.03$ GHz. This is then shifted by a double-pass 80 MHz AOM to

$\Delta_A/2\pi = +870$ MHz

In order to minimise dephasing due to Doppler broadening mechanisms excitation is performed with two counter-propagating fields orientated as shown in Fig. 8.1(a). There still exists a small contribution due to Doppler broadening arising from the large difference in excitation wavelengths which yields an effective wavevector $\mathbf{k}_{\text{eff}} = |\mathbf{k_1} + \mathbf{k_2}|$.

The almost unresolvable hyperfine splitting of Rydberg states <100 kHz [140] requires exciation to be constructed on an m_j basis. The stretched states can be though as a $m_j = \pm 1/2$ with the clock state being a super-position of both. The work presented in this chapter considers excitation to the $|69S_{1/2}, m_j = 1/2\rangle$. The strongest coupling arises when prepared in the stretched state and exciting in $\sigma^+\sigma^-$ configuration, however preparation in the clock state offers more flexibility when introducing other rotations to generate ground state entanglement, the excitation scheme is shown in Fig. 8.1(b).

8.3 Alignment

The Qubit A beam uses the same beam path as the Qubit B beam presented in the previous chapter and alignment is easily controlled, the setup is shown in Fig. 8.1(a). The beam waist is increased to 14.6 μm by using an iris to aperture collimator, to achieve similar couplings for both single atom sites necessary for demonstration of blockade (see Chapter 9). Control of the Rydberg beam waist is however more challenging, this is due to the focal plane of 509 nm light lying 350 μm before the plane of the trapping light. To push to focal plane towards the trapping sites the 509 nm light is focused down to 120 μm, around 50 mm before the aspheric lens. This should provide a focus of around 10 μm at the single atoms but due to potential aberrations of the green light is expected to be bigger.

As the transition line-width for off resonant excitation is narrow and sensitive to Stark shifts, alignment of the Rydberg beam is performed on resonance with the molasses beams, which has a very broad resonance. This not only presents a straight forward alignment method but also once the resonant frequency for the Rydberg laser is found an expected range for the off-resonant resonance can easily be calculated. Alignment is performed with the dipole trap chopped out of phase with with the molasses beams, as in imaging, and Rydberg light applied. The alignment of the Rydberg beam is adjusted to maximise the loss from this process. It is found that fine tuning alignment is best achieved through moving the trapping site of the single atoms and monitoring the retention per pixel region to obtain the best Rydberg coupling.

8.4 Rydberg Rotations

The standard sequence for spectroscopy of the Rydberg state and performing rotations is outlined in Fig. 8.2. The single atom is released for a constant duration, typically 5-10 μs dependant upon the experiment although drop times of up to 17.5 μs can be achieved with a high retention probability > 0.95. In order to increase the Rydberg detection efficiency the recapture depth is 1 mK. The 509 nm field remains on for the entirety of the drop with the Qubit A beam pulsed on for the desired time before detection. This allows measurements to be made with only a dependency on the pulse area of Qubit A. Spectroscopy is performed with the pulse duration set to the expected π time with the sideband detuning of the green laser scanned. Once a resonance is found Rabi flopping is performed on resonance for varying pulse durations. The drift of the cavity lock is found to be 1 Hz/s [138] therefore as long as powers remain constant there is no need to repeat spectroscopy over the course of a days experiments. Fig. 8.3 (a) shows an example of such a Rabi flop from the stretched state obtaining a two photon Rabi frequency

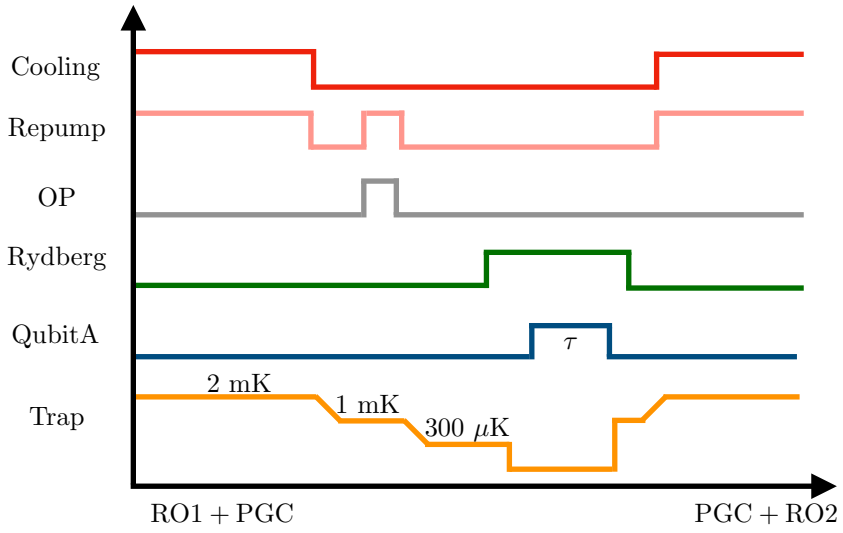

Figure 8.2: Rydberg excitation sequence after cooling the single atom is initialised in either $|4,0\rangle$ or $|4,4\rangle$ via optical pumping. The trap is then lowered to $U_0 = 300$ μK to further cool the atom before two photon excitation performed with the trap extinguished. Following the excitation beam the single atom is recaptured at $U_0 = 1$ mK to increase detection efficiency before ramping back to U_0 =2 mK for second readout.

$\Omega/2\pi = 0.69$ MHz, using 590 μW of Qubit A power and 92.5 mW of Rydberg. Taking this information and modiflying the calculations in section 4.3.1 it can be deduced that the waist of the Rydberg beam is $w_C \sim 18\mu$m.

Fig. 8.3(a) and (b) show Rabi flops $|69S, m_j = 1/2\rangle$ obtained from the stretched state $\Omega/2\pi = 0.69$ MHz, and clock state $\Omega/2\pi = 0.73$ MHz, respectively for relatively similar two photon Rabi frequencies. Between taking the stretched state and clock state data a faulty shutter was discovered causing intermittent optical pumping which explains the poorer contrast observed in the stretched state data. Both oscillations are susceptible to a fast decay $\tau = 2.9, 2.4$ ms however as this decay is symmetric it indicates that this is not due to spontaneous emission. Further verification is found by increasing the Qubit A power to perform a flop at faster frequency Fig. 8.3(c) where a similar decay time is observed $\tau = 2.9$ ruling out spontaneous emission. As the measurements are performed with counter-propagating beams and at

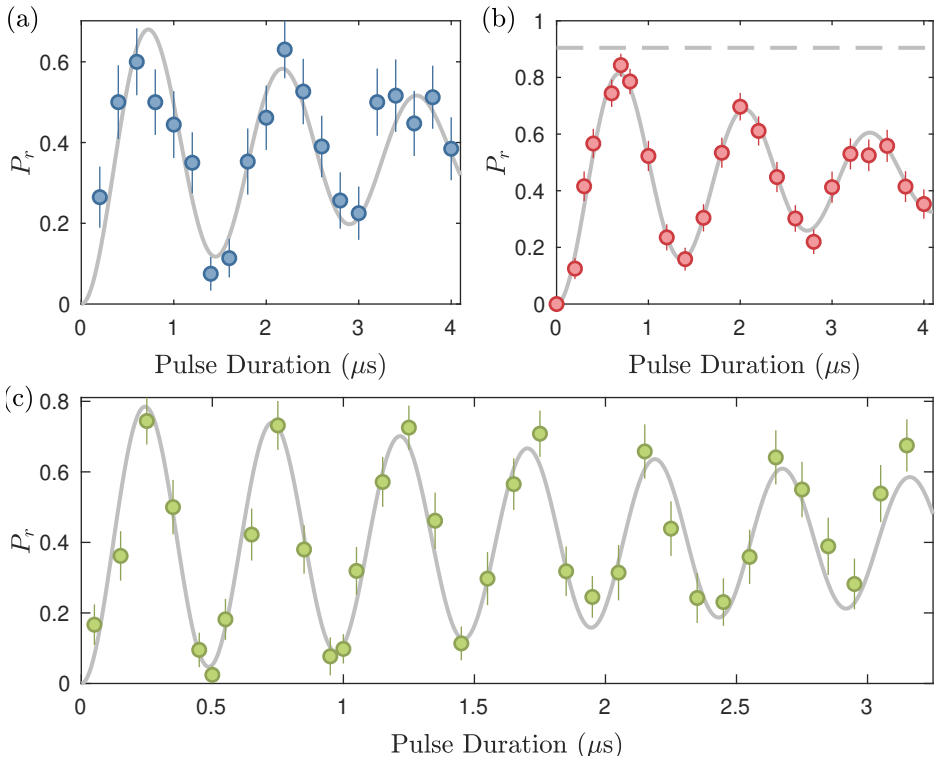

Figure 8.3: Rydberg Rabi Oscillations to $|69S, m_j = 1/2\rangle$ from, (a)$|4, 4\rangle$ obtaining $\Omega/2\pi = 0.69$ MHz$, \tau = 2.9$ μs (b)$|4, 0\rangle$ obtaining $\Omega/2\pi = 0.73$ MHz$, \tau = 2.4$ μs (c) $|4, 4\rangle$ obtaining $\Omega/2\pi = 2.06$ MHz$, \tau = 2.9$ μs.

$T = 10$ μK, Doppler broadening cannot be attributed to this. Similarly the Rydberg laser intensity is well-stabilised by a noise-eater to less than 1 % fluctuations and the Qubit A beam is found to have around a 2.5 % instability indicating intensity noise is not the issue either. Fluctuations in magnetic fields can also be ruled out as the $|4, 4\rangle \rightarrow |69S, m_j = 1/2\rangle$ transition has no differential Zeeman shift so one would expect a significant difference between excitation from the clock and stretched state if this was the case.

A recent publication has found that a consequence of ULE locks for Rydberg excitation is the creation of laser phase noise at around $2\pi \cdot 1$ MHz causing rapid decoherence of oscillations [139]. This has been further verified in [141] where light from the ULE cavity was used as a spectral filter to injection lock another laser diode, greatly reducing the associated laser phase noise from the lock, leading to oscillations with decay constants of up to $\tau = 27$ μs

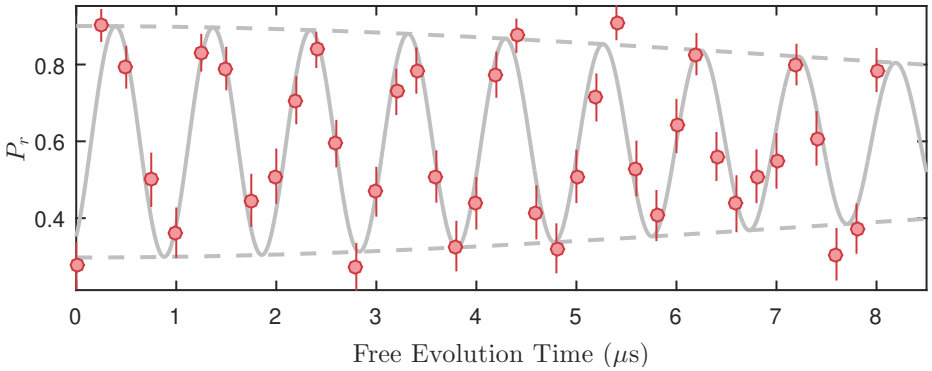

Figure 8.4: Ramsey interferometry for $|4,4\rangle \rightarrow |69S_{1/2}, m_j = 1/2\rangle$ using a $\tau\pi/2 = 400$ ns, obtaining $T_2^* = 15 \pm 4$ μs in reasonable agreement with the predicted Doppler limitation for $T = 10$ μK

being achieved. However despite this, gate operations generally require fast rotations therefore high fidelity operations can still be achieved without the need to address the laser phase noise on the experiment.

8.5 Measurement of T_2^*

Like the previous chapter an excellent measure of the ability to perform qubit operations is Ramsey interferometry, as the laser is off for the majority of the Ramsey sequence this should also help clarify if the dephasing observed is indeed laser-phase related. The inhomogenous dephasing time for Rydberg states has been found to have two contributing factors magnetic fields fluctuations $T_{2,B}^*$ and Doppler effects $T_{2,D}^*$ [23], as we observe no significant difference in clock state vs stretched state excitation we can consider our magnetic fields fluctuations to be negligible and the dominant factor to be due to Doppler effects. The Doppler limitation is given by [23]

$$T_{2,D}^* = \left(\frac{2\mathrm{m}}{k_B T}\right)^{1/2} \left(\frac{1}{k_{\mathrm{eff}}}\right), \tag{8.2}$$

for the experiment parameters and a temperature of 10 μK this calculation yields a decay time of around 11 μs indicating that if this is the dominant

factor the Ramsey spectroscopy should yield a similar result.

The spectroscopy is performed on the stretched state using two $\pi/2 = 400$ ns pulses separated by a variable duration. Fig. 8.4 shows the result of this measurement, what is immediately obvious from this data is the far superior damping compared to the oscillations presented in Fig. 8.3. This represents a strong indication that the previous issues are caused by laser phase noise. The data is fitted to an adaptation of Eq. 7.3 obtaining an oscillatory frequency of ω_{Ram} $\sim$1 MHz and T_2^*=14.8$\pm$4 μs, in good agreement with the predicted Doppler limited $T_{2,D}^*$. The time obtained is longer than what has been observed in other experiments [141] and can be primarily attributed to the cold temperature and heavier atomic species minimising Doppler effects. This demonstrates coherences far longer than required for Rydberg mediated gates. The obtained time can be used to estimate the attainable fidelity via Rydberg interactions for pulses separated by t [23]

$$\mathcal{F} = \frac{1}{2}(1 + \exp(-t^2/T_2^*)), \tag{8.3}$$

suggesting for a 500 ns gap time a fidelity $\mathcal{F} > 0.99$ should still be be realisable

8.6 Measurement of Rydberg State Detection Efficiency

As outlined in Sec. 8.1 the Rydberg state detection is dependant upon a number of factors. A dominant factor that can easily be controlled experimentally is the magnitude of the anti-trapping potential the Rydberg atom experiences, i.e the trap depth at recapture. To measure the detection efficiency at different potentials the atom is placed into the Rydberg state through the application of a π-pulse the trap is then applied for a varying

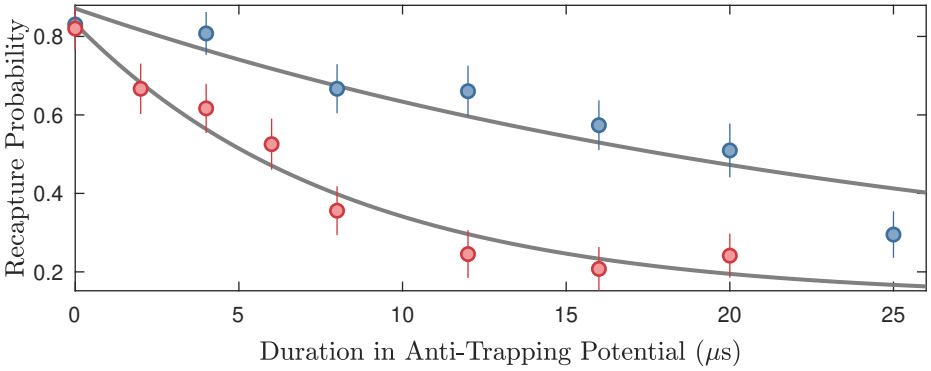

Figure 8.5: Measurement of Rydberg detection through applying a varying duration of the trapping potential following a π rotation to $|r\rangle$. After the potential is applied the state is returned to $|g\rangle$ though another π rotation and recaptured. Blue points correspond to $U_0 = 300$ μK and red points represent $U_0 = 1$ mK fitting to exponential decays $1/e$ time constants are obtained of $\tau = 25.7$ μs and $\tau = 8.2$ μs for the respective applied potential.

Parameter	Error
Clock State Pumping Error e_{OP}	0.04
Rydberg Detection Error e_{D}	0.06
False-Positive Error e_{F}	0.01

Table 8.1: Rydberg detection errors

duration before a second π- pulse is applied returning the atom to the ground state before recapture. Detection depths of $U_0 = 300$ μK and U_0 =1 mK are considered and the results presented in Fig. 8.5. The time τ_r is simply the $1/e$ decay constant from an exponential fit to the data obtaining durations of 25.7 and 8.2 μs respectively. The 300 K lifetime of $69S_{1/2}$ is $\tau_{\mathrm{Ryd}} = 134$ μs giving an estimated detection errors of e_{D} =0.2 and 0.06 demonstrating a significant advantage of performing Rydberg detection with deeper trapping potentials.

This result now allows the maximal expected population of P_r to be estimated with the experimental errors factored in, Table 8.1. Using Eq. 8.1 and setting $\tilde{P}_r = 1$ and $\tilde{P}_g = 0$ as would be expected at a π time absent of error and dephasing returns a measured population $P_r = 0.9$. This is in excellent agreement with the fitted amplitude to the clock state data in Fig. 8.3 of

0.9. The damping from laser phase noise prevents a population of 0.9 being measured with a population of only 0.84 observed by the π duration. Driving faster oscillations may overcome this effect and allow maximal Rydberg transfer however this may result in a compromise with spontaneous emission.

8.7 Conclusion

Coherent excitation to the Rydberg state has been achieved from the clock and stretched state. Although oscillations are quickly damped due to laser phase noise the ability to drive fast rotations with a dephasing time far exceeding that of a gate rotation has been shown though Ramsey interferometry achieving $T_2^* = 14$ μs around two orders of magnitude longer than the $\pi/2$ rotation used. Solutions to reduce the laser phase noise from the ULE lock have been shown in [141] with coherence times of 27 μs being observed in their Rabi Oscillations. However the T_2^* on this experiment still exceeds the time achieved in their setup by a factor of two indicating that a change is not required to drive gates where the laser atom interaction is short.

Chapter 9

Rydberg Blockade and Ground State Entanglement

The previous chapters demonstrate the ability to drive controlled rotations between the ground states and to Rydberg states with single atoms. This chapter now considers excitation with a second atom introduced within the blockade distance to create the entangled $|\mathcal{W}\rangle$ state. Mapping this state back down to the other hyperfine manifold allows deterministic ground state entanglement to be realised. The first experimental observations of the Rydberg blockade between two atoms were obtained by the Wisconsin [62] and Paris [63] group in 2009. Both experiments showed suppression of excitation to the doubly excited state $|rr\rangle \sim P_{rr}$ =30 % and 15 % for the respective experiments. Since then experiments have been developed which suppress the excitation of $|rr\rangle$ even further to $P_{rr} < 5$ % [141]

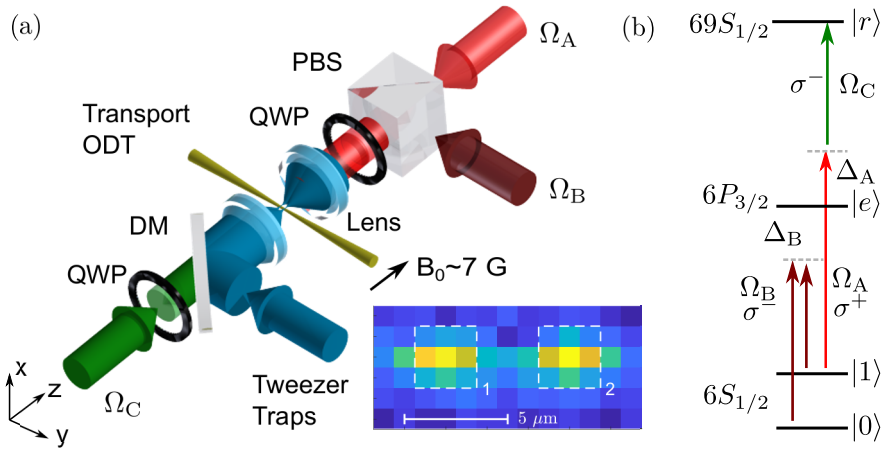

Figure 9.1: (a) Laser setup for blockade and ground state entanglement generation. Qubit A and B are orthogonally polarised and are focused to waists of $w_A = 14.6$ μm and $w_B = 20$ μm respectively. (b) Excitation scheme for ground state entanglement. The detuning for the ground state Raman lasers is now $\Delta_B/2\pi = 43$ GHz.

9.1 Collective Enhancement and Rydberg Blockade

The experimental procedure remains the same as the previous chapter all aside the introduction of the second atom with the setup and excitation pathway shown in Fig 9.1. The atoms can be separated down to a minimum spacing of 5 μm (pixels), any distance smaller than this results in large amounts of cross talk between the atom ROIs making discrimination difficult and hopping of atoms between traps is observed. The experiments presented in this chapter use a separation of 6 μm which is still well within the blockade radius for the driving frequencies characterised in the previous chapter. Recalling that $R_b = \sqrt[6]{C_6/\Omega}$, for $69S_{1/2}$ $C_6 = -573$ MHz$\cdot\mu$m^6 [75] and for a two photon Rabi frequency $\Omega/2\pi = 0.75$ MHz gives a blockade radius of 9.6 μm. For two-atom experiments there are four possible outcomes:

- P_{gg} the probability both atoms are in the ground state $|11\rangle$, both are recaptured.

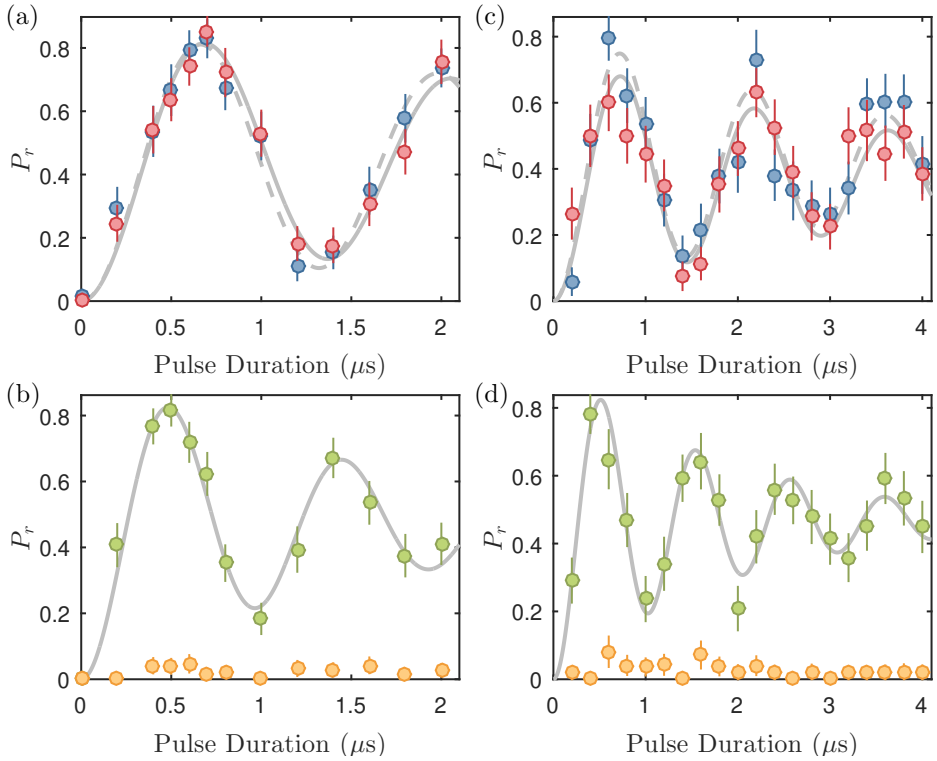

Figure 9.2: Two atom Rydberg Rabi flops, red and blue points represent trap one and two where only respective trap loaded, green points shows the two atom probability of one atom being excited to the Rydberg state $|1r\rangle + |r1\rangle$ and the yellow points correspond to population of the doubly excited state $|rr\rangle$. Single atom probabilities are shown in (a) and (c) for excitation from the clock and stretched state respectively and similarly for the two atom probabilities in (b) and (d). A clear collective enhancement in coupling is observed in the two atom probabilities $|1r\rangle + |r1\rangle$ compared to the single atom case as well as a high suppression of excitation to $|rr\rangle$, $P_{rr} < 0.05$.

- P_{rg},P_{gr} the probability one atom is in the Rydberg state and the other is in the ground state $|r1\rangle$,$|1r\rangle$, one atom is lost the other is recaptured.
- P_{rr} the probability both atoms are in the Rydberg state $|rr\rangle$, both are lost.

These are normalised such that $P_{gg} + P_{rg} + P_{gr} + P_{rr} = 1$. As the likelihood of atom loading for each trial is stochastic for 200 repeats of the experiment one obtains around 60 two-atom data measurements, with single atom data for each trap obtained in the instances where only one atom is loaded. Fig 9.2 presents experiments conducted from the clock (a)-(b)

and stretched state (c)-(d). The single atom trails obtain Rabi frequencies of $\Omega_r/2\pi = 0.73 \pm 0.01, 0.69 \pm 0.01$ MHz and a clear enhancement in coupling in the two atom data is observed $\Omega_r'/2\pi = 1.04 \pm 0.02, 0.97 \pm 0.01$ MHz. The ratio of these couplings gives $\Omega_r'/\Omega_r = 1.42 \pm 0.03, 1.41 \pm 0.02 \approx \sqrt{2}$ in excellent agreement with the predicted theory. Further evidence of blockade is seen with an almost complete suppression of excitation to the doubly excited state $|rr\rangle$ with $P_{rr} < 5$ %.

9.2 Ground State Entanglement

The entangled $|\mathcal{W}\rangle$ state created by blockade is short lived therefore it is preferential to map this entanglement down to the long lived hyperfine ground states. Achieving this requires re-introducing the Qubit B rotation laser used in Chapter 7 to drive ground state rotations. This laser has now been coupled into a separate fibre and is combined with Qubit A on a PBS before the chamber as shown in Fig 9.1(a) and is focused to a waist of $w_B = 20$ μm at the atoms with a detuning of $\Delta_B/2\pi = -43$ GHz from the $6P_{3/2}$ transition. As Qubit A and B have orthogonal polarisations they drive σ^+ and σ^- transition respectively as shown in Fig 9.1(b).

Ground state entanglement is created by the following sequence; following preparation in $|1\rangle = |F = 4, m_f = 0\rangle$ a π-pulse at the $\sqrt{2}$-enhanced Rabi frequency to the symmetric state $|\mathcal{W}\rangle$ is applied using the Rydberg rotation lasers creating the state $|\mathcal{W}\rangle = \frac{1}{\sqrt{2}}(|1r\rangle + |r1\rangle)$. This is then followed by a π-pulse using the ground state Raman laser creating $|\psi\rangle = \frac{1}{\sqrt{2}}(|0r\rangle + |r0\rangle)$. Finally another π-pulse is applied using the Rydberg lasers at the single atom Rabi frequency to create the maximumly entangled Bell state

$$|\Psi^+\rangle = \frac{1}{\sqrt{2}}(|01\rangle + |10\rangle). \tag{9.1}$$

This pulse sequence is summarised and shown in Fig 9.3(a).

9.2.1 Parity Oscillations

Transferring this $|\mathcal{W}\rangle$ state to the ground state similarly yields a population of 50 % in P_{01} and P_{10}. However this can not be distinguished from a statistical mixture through population measurement alone. Evidence of entanglement requires direct measurement of the off-diagonal coherences of the density matrix ρ, which has the following form

$$\rho = |\psi\rangle\langle\psi| = \begin{pmatrix} P_{|00\rangle} & \rho_{00,01} & \rho_{00,10} & \rho_{00,11} \\ \rho^*_{00,01} & P_{|01\rangle} & \rho_{01,10} & \rho_{01,11} \\ \rho^*_{00,10} & \rho^*_{01,10} & P_{|10\rangle} & \rho_{10,11} \\ \rho^*_{00,11} & \rho^*_{01,11} & \rho^*_{10,11} & P_{|11\rangle} \end{pmatrix}. \tag{9.2}$$

For the perfectly prepared Bell state in Eq. 9.1 this should read

$$\rho = \begin{pmatrix} 0 & 0 & 0 & 0 \\ 0 & 0.5 & 0.5 & 0 \\ 0 & 0.5 & 0.5 & 0 \\ 0 & 0 & 0 & 0 \end{pmatrix}. \tag{9.3}$$

The fidelity of this state is equal to $\mathcal{F} = \langle\Psi^+|\rho|\Psi^+\rangle = (P_{01} + P_{10})/\sqrt{2} + \mathcal{R}(\rho_{01,10})$. Measurement of the the off-diagonal coherences can be performed through preparing $|\Psi^+\rangle$ and applying a global ground-state rotation pulse to extract the parity which is defined as

$$\Pi = P_{00} + P_{11} - P_{01} - P_{10}. \tag{9.4}$$

Upon application of the analysis pulse with an area θ and phase ϕ the parity is equal to [142]

$$\begin{aligned} \Pi(\theta) = P\cos^2\theta - 2\mathcal{R}(\rho_{00,11}e^{i2\phi})\sin^2\theta + 2\mathcal{R}(\rho_{01,10})\sin^2\theta \\ + Im\left[(\rho_{00,10} - \rho_{01,11} + \rho_{00,01} - \rho_{10,11})e^{i\phi}\right]\sin 2\theta, \end{aligned} \tag{9.5}$$

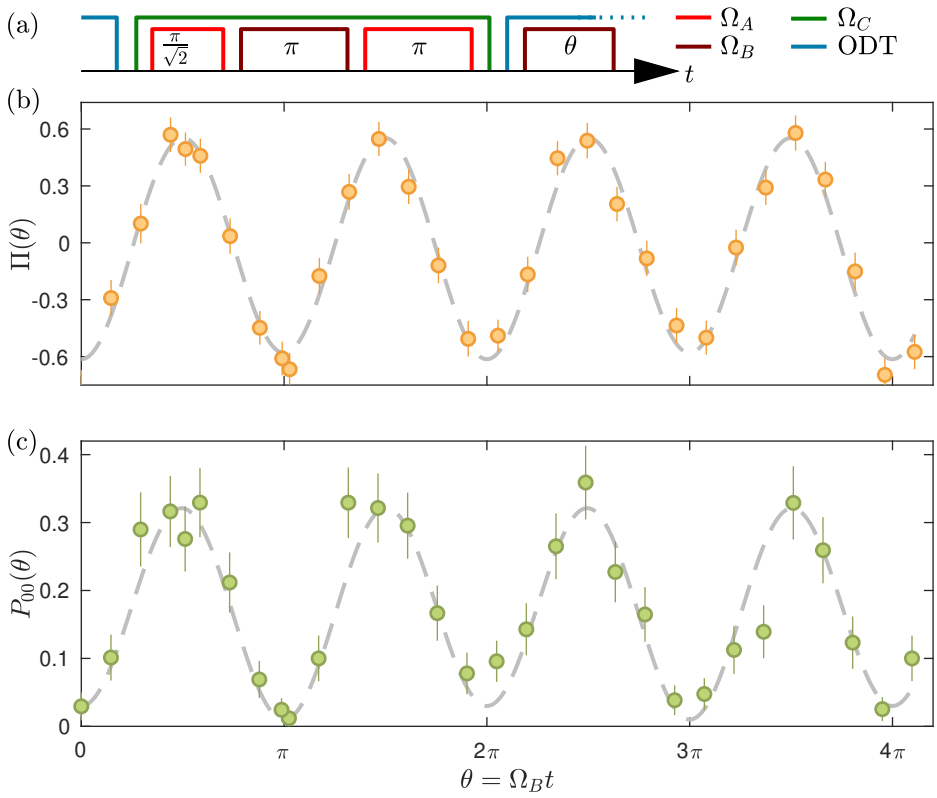

Figure 9.3: (a) Pulse sequence to generate Bell state via Rydberg blockade. (b) Parity oscillation at the expected 2Ω showing evidence of off-diagonal coherence. (c) Evolution of the observing atoms in $|00\rangle$ state during analysis pulse.

thus an analysis pulse with an area of $\theta = \pi/2$ reduces this to $\Pi(\pi/2) = 2\mathcal{R}(\rho_{01,10}) - 2\mathcal{R}(\rho_{00,11}e^{i2\phi})$ allowing the off-diagonal coherences be extrapolated. As the atoms are addressed simultaneously there is no direct control over ϕ and it is assumed that the phase is random and averages out over the course of the experiment. This procedure also does not account for losses which need to be considered as will be shown below.

The Bell state is prepared using the sequence described earlier and shown in Fig 9.3(a), the powers of the rotation lasers at the atoms are $P_A = 2$ μW, $P_B = 200$ μW and $P_C = 90$ mW for the Qubit A, Qubit B and 509 nm Rydberg lasers respectively. This corresponds to pulse durations for the respective rotations of $\pi_R/\sqrt{2} = 500$ ns, $\pi_G = 700$ ns and $\pi_R = 700$ ns with

the entanglement sequence completed within 2 μs to allow for pulse padding due to differing trigger delays. Following the completion of the entanglement preparation the atoms are recaptured at $U_0 = 300$ μK and the Raman laser analysis pulse applied with a variable pulse area $\theta = \Omega_B t$ to perform parity oscillations. This is then followed by a blow away pulse to determine the atomic states and find the two atom populations, similarly to the blockade measurements four different population probabilities are obtained P_{00}, P_{11}, P_{01} and P_{10}.

Fig 9.3(b) shows the resulting parity oscillation which exhibits a strong oscillation at $2\Omega_R$ and is fitted to $\Pi(\theta) = P_0 + A\cos\Omega_B + B\cos 2\Omega_B$. In the case of a perfectly prepared Bell state this would correspond to fitted amplitudes of $A = 0$ and $B = -1$. Following [143] the fit of this oscillation can be used to extract $\mathcal{R}(\rho_{01,10}) = |B|/2$ giving a fidelity $\mathcal{F} \sim 0.76$. However this does not account for loss of atoms that remain in the Rydberg state or that fall out-with the basis states after initialisation. These losses result in a false-positive error associated with the measurement of atoms in the state $|1\rangle$ which are lost during the blow away pulse. Therefore an intuitive way to measure the relative coherences and populations is through the analysis of P_{00} during the analysis pulse. This state is less susceptible to error as the only way it can be measured is through survival of both atoms and therefore can not be overestimated due to loss of atoms unlike P_{11}.

The P_{00} population during the analysis pulse is shown in Fig 9.3(c). Following the analysis presented in [63, 64] where it is assumed that ϕ is random and averages out over the course of the measurement; Populations $P_{|00\rangle}$ and $P_{|11\rangle}$ are simply extracted from this taking $P_{00}(0) = P_{|00\rangle} = 0.03 \pm 0.02$ and $P_{00}(\pi) = P_{|11\rangle} = 0.01 \pm 0.01$. Calculation of $P_{|01\rangle} + P_{|10\rangle}$ however requires losses to be considered. In the absence of losses over the duration of the analysis pulse one would expect the average survival probability of each atom independent of the other $\langle P_{1,2}\rangle$ to be 0.5, thus the loss probability of each

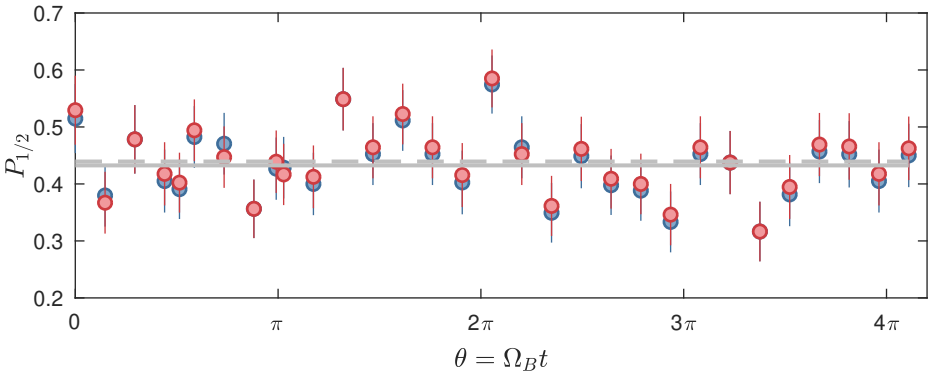

Figure 9.4: Probability of survival in either trap following parity analysis sequence. Line (Dashed) indicates average survival probability of trap 1 (2) giving $L_{1,2} = 0.13, 0.12$.

trap is given by [63]

$$L_{1,2} = 1 - 2\langle P_{1,2}\rangle, \tag{9.6}$$

the survival probability of each trap is shown in Fig 9.4, from this the loss rate from each trap averaged over θ is found to be $L_{1,2} = 0.13 \pm 0.01, 0.12 \pm 0.01$. This yields a total loss rate of $L_t = 1 - \rho = L_1 + L_2 - L_1 L_2 = 0.24 \pm 0.01$ which is in excellent agreement with the measured recapture probability of two atoms without the presence the state discrimination pulse, $p_{recap} = 0.78 \pm$ 0.03. Finally one can calculate $P_{|01\rangle} + P_{|10\rangle} = 1 - L_t - P_{|11\rangle} - P_{|00\rangle} = 0.72 \pm 0.03$. The off-diagonal coherence $\mathcal{R}(\rho_{01,10})$ can also be calculated from analysis of $P_{00}(\theta)$ with P_{00} averaged over theta equal to [63]

$$\langle P_{00}(\theta)\rangle = (P_{|01\rangle} + P_{|10\rangle} + 3(P_{|11\rangle} + P_{|00\rangle}) + \mathcal{R}(\rho_{01,10}))/8. \tag{9.7}$$

Calculation of the coherence via this method obtains $\mathcal{R}(\rho_{01,10}) = 0.27 \pm 0.09$ in excellent agreement with the value obtained from the simple analysis of the parity oscillation. This can be further verified with a more in depth

Elements	Measured Value
$\rho_{00,00} = P_{\|00\rangle} = P_{00}(0)$	0.03±0.02
$\rho_{11,11} = P_{\|11\rangle} = P_{00}(\pi)$	0.01±0.01
$\rho_{01,01} + \rho_{10,10} = P_{\|01\rangle} + P_{\|10\rangle}$	0.72±0.03
$\mathcal{R}(\rho_{01,10})$	0.27±0.03
$\mathcal{F} = (P_{\|01\rangle} + P_{\|10\rangle})/2 + \mathcal{R}(\rho_{01,10})$	0.63±0.03

Table 9.1: Measured values of the density matrix extracted from analysis of the parity oscillation data of Fig 9.3.

analysis by altering the above relation and fitting the data to [63]

$$\begin{aligned} P_{00}(\theta) =& \frac{1}{8}\left(P_{\|01\rangle} + P_{\|10\rangle} + 2\mathcal{R}(\rho_{01,10}) + 3(P_{\|11\rangle} + P_{\|00\rangle})\right) \\ &+ \frac{1}{2}(P_{\|11\rangle} - P_{\|00\rangle})\cos\theta \\ &+ \frac{1}{8}\left(P_{\|00\rangle} + P_{\|11\rangle} - P_{\|01\rangle} - P_{\|10\rangle} - 2\mathcal{R}(\rho_{01,10})\right)\cos 2\theta, \end{aligned} \tag{9.8}$$

and constraining already obtained values, with the resulting fit shown in Fig 9.3(b). This analysis yields $\mathcal{R}(\rho_{01,10}) = 0.27 \pm 0.03$, which is in excellent agreement with the previous methods . Collating the obtained information presents a deterministic fidelity of $\mathcal{F} = 0.63 \pm 0.03$, in excess of the $\mathcal{F} > 0.5$ threshold for entanglement verification. Factoring in the measured losses from the experiment the loss corrected fidelity is $\mathcal{F}_{\text{pairs}} = \mathcal{F}/p_{\text{recap}} = 0.81 \pm 0.05$. This represents the highest post-selected ground-state entanglement achieved via Rydberg blockade and equal to that obtained though Rydberg dressing [68]. A summary of the values obtained is presented in Table 9.1

It is expected that the main limitation preventing higher fidelities is caused by imperfect Rydberg excitation due to laser dephasing. For instance the maximum transfer in blockade measurements presented in Fig 9.2(b) sees around a 81 % transfer to the $|\mathcal{W}\rangle$ state. Factoring in detection and optical pumping efficiency this corresponds to an actual population of $\tilde{P}_r \approx 0.9$ indicating around 0.1 of the population are out-with the basis state following the first pulse mapping to $|\mathcal{W}\rangle$. Improvements to optical pumping and upgrading the laser system as in [141] should see the number of atom transfer

to $|\mathcal{W}\rangle$ increase and therefore should result in a higher ground state entanglement fidelity as seen by a demonstration of $\mathcal{F} = 97$ % in $|\mathcal{W}\rangle$. In the short term this could be overcome by driving faster Rydberg rotations to maximise state transfer, however this is detrimental to the blockade radius and will introduce spontaneous emission into the system.

9.3 Single Site Addressability

The vast majority of two-qubit gates such as C_Z and C_N require operations on each qubit to performed independent of the other. This requires single site addressability with the rotation lasers. As the 509 nm light does not couple to anything when an atom is in the ground state it requires no alteration and localised addressing can be achieved with only the 852 nm lasers. Removing the aperture placed in the Qubit A path allows the beam to be focused down to 2 μm this is aligned using the imaging system as previously as previously discussed to overlap with the same pixel as one of the traps. The power in the beam is reduced to 35 nW and a flop performed at resonance as shown in Fig 9.5(a), with the other site is located 6 μm away. As can be seen from this dataset a flop is observed in only one trapping site and a relatively constant baseline is observed within the other trap, indicating the ability to address a single trap. However a much faster dephasing in the Rabi flop is observed, $\tau = 1.2$ μs compared $\tau > 3$ μs in previous measurements. This is surprising as the relative couplings are similar, giving a two photon Rabi frequency of $\Omega/2\pi = 0.74$ MHz. It is hypothesised that this observed increase in dephasing could possibly be due to a beam pointing instability due to the much smaller focus or being more sensitive to the atomic motion during the 5 μs drop. Verification of this hypothesis is sought through increasing the Qubit A focus to 3.8 μm and repeating the measurement, Fig 9.5(b). A much better flop is obtained which is consistent with previous Rabi oscillations performed to the Rydberg state obtaining $\Omega/2\pi = 0.73$ MHz and $\tau = 2.5$ μs.

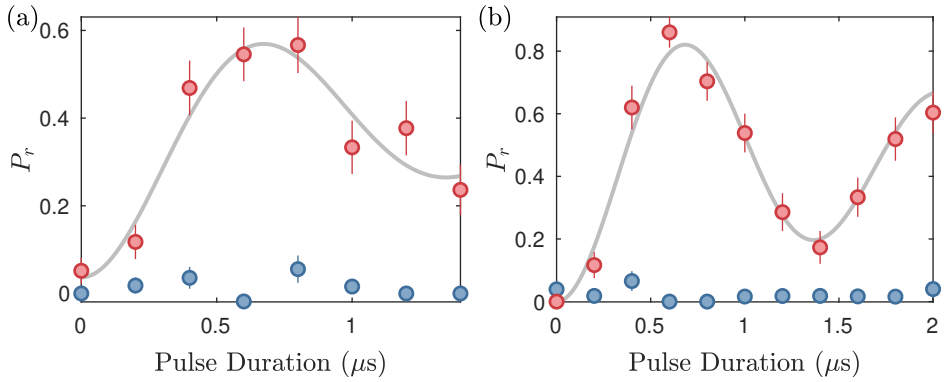

Figure 9.5: Rydberg excitation with a Qubit A waist of (a) $w_A = 2$ μm and (b) $w_A = 3.8$ μm focused upon trap 2 (red points). In both cases an oscillation is observed with $\Omega/2\pi = 0.74$ MHz and $\Omega/2\pi = 0.73$ MHz with minimal cross-talk in the other site trap 1 (blue) points.

Furthermore crosstalk < 5 % is seen in the other trapping site with slight discrepancies consistent with shot to shot retention, thus demonstrating single site addressability without detrimental effects on rotations.

9.4 Conclusion

Rydberg blockade has been shown between two single atoms achieving an almost complete suppression in the population of the double excited state $P_{rr} < 5\%$ and demonstration of excitation to the entangled $|\mathcal{W}\rangle$ shown through the collective enhancement in the Rabi frequency. This state has been mapped to to the other ground state level to create a maximumly entangled Bell state $|\Psi^+\rangle$ achieving a deterministic preparation fidelity of $\mathcal{F} = 0.63 \pm 0.03$ and a loss-corrected fidelity of $\mathcal{F}_{\text{pairs}} = 0.81 \pm 0.05$. This represents the highest post-selected ground-state entanglement achieved via Rydberg blockade. The deterministic fidelity could be further improved through elimination of laser phase noise as shown in [141], to reduce losses associated with imperfect Rydberg excitation and to increase the initial preparation fidelity in $|\mathcal{W}\rangle$. Further to this in preparation of future experiments single site addressability has been demonstrated between atoms separated by 6 μm

presenting a setup ready for gate operations.

Part V

Conclusions and Outlook

Chapter 10

Conclusion

The work in this thesis has presented a system capable of performing fast rotations between hyperfine ground states and ground-Rydberg excitation as well as demonstrating the necessary high fidelity readout for implementing quantum gate protocols. Further to this demonstration of the Rydberg blockade has been shown with the resulting entangled $|\mathcal{W}\rangle$ state being mapped to create a ground-state entangled Bell state.

10.1 Qubit Delivery and Readout

Single atom trapping using microscopic tweezers with waists of $w_0 = 1.82, 1.87$ μm has been shown achieving sub-Poissonian loading of single atoms with a probability $P > 0.5$. To improve the statistics gathered by the experiment and reduce the number of measurements cycles required the loading probability could be increased to $P > 0.9$ to give a near deterministic loading of single atoms, through careful tuning of light assisted collisions using light on the D_1 transition [112, 123] without compromising the experiment cycle time.

High fidelity imaging with a shot to shot retention probability limited by

background pressure has been demonstrated using an sCMOS camera offering far superior readout rates compared to EMCCD technology. Further to this the possibility to perform hyperfine selective readout has been shown as in [109] with the ability to scatter enough photons for high fidelity readout demonstrated without the need for repump light. This could be effectively implemented in the experiment though minor changes to increase the bias field along the probe axis and introducing a counter propagating probe beam, ideally with a frequency offset from the original probe beam to avoid creating of a standing wave.

The first statement of the DiVincenzo criteria for quantum computing requires a scalable physical system with well characterised qubits. As previously discussed a prime advantage of neutral atoms in quantum computation is scalability, with large 2D defect free arrays already possible with dynamically reconfigurable tweezers [40]. The fast readout speeds of sCMOS technology combined with enhanced loading and reconfigurable tweezers should offer a system that not only satisfies this criteria, but offers better scalability potential compared to EMCCD technology due to the larger available detector sizes.

10.2 Qubit Rotations

Two-photon transitions have been used to circumnavigate weak magnetic dipole coupling to perform rotations between hyperfine states with state transfer limited by optical pumping fidelity $\mathcal{F}_{\mathrm{OP}} = 0.96$. This could be further improved through optical pumping on the D_1 transition to achieve $\mathcal{F}_{\mathrm{OP}} > 0.99$ [67] due to the larger excited state hyperfine splitting of 1.2 GHz compared to 250 MHz on the D_2 line.

Ramsey spectroscopy has been performed on the qubit rotation and found an inhomogenous dephasing time of $T_2^* = 10 \pm 1$ ms which is over 4 or-

der of magnitudes greater than the π-rotation and in good agreement with the predicted limitation due to temperature. This coherence time can be further extended through a spin-echo sequence where reversible dephasing mechanisms are recovered through the application of a π-pulse in between the Ramsey pulses obtaining $T_2' = 150 \pm 20$ ms.

Similarly two photon transitions to Rydberg states overcome weak single photon electric dipole transitions to Rydberg states and have been performed to $|69S_{1/2}, m_j = 1/2\rangle$. Rabi oscillations to this state are found to be limited by laser phase noise arising from the ULE cavity lock at $2\pi \times 1$ MHz causing rapid dephasing of oscillations [139, 141]. However, it has been shown through Ramsey interferometry that rotations where the laser atom interaction time is short can still attain long coherence times with an inhomogenous dephasing time of $T_2^* = 15 \pm 4$ μs, far exceeding the timescale for the majority of quantum gates as required by the DiVincenzo criteria and demonstrating the longest ground-Rydberg coherence time to date. This is primarily due to the cold atomic temperature and almost Doppler free excitation configuration.

Rydberg state detection has been improved through recapturing the atom after excitation with a deeper trapping potential reducing the detection error to $e_{\mathrm{D}} = 0.06$ from $e_{\mathrm{D}} = 0.2$. This will be further improved when the experiment moves to a cryogenic environment at 4 K as the Rydberg lifetime will increase due to a suppression in black body induced transitions with the lifetime of $69S_{1/2}$ extending to $\tau'_{\mathrm{Ryd}} = 349$ μs from $\tau_{\mathrm{Ryd}} = 134$ μs, decreasing the detection error to $e'_{\mathrm{D}} = 0.023$. This combined with the scheduled upgrade of the optical pumping to the D_1 transition will see the total measurable Rydberg population scale up to $P_r = 0.97$ assuming no losses to back ground collisions and an improved optical pumping fidelity of $\mathcal{F}'_{\mathrm{OP}} = 0.99$. Observation of this will however still require an upgrade of laser systems to remove the associated phase noise as the dephasing caused by this also limits

Rydberg state transfer.

Coherence times of both hyperfine rotations and ground-Rydberg rotations could be further enhanced by cooling to the vibrational ground state via Raman sideband cooling [129, 131] which also optically pumps the atom thus avoiding heating caused by the optical pumping schemes presented in this thesis. Colder atoms however may increase Rydberg state detection error as they will now take longer to leave the trapping region and may decay to the ground state before having moved sufficiently far from the trapping region to not be recaptured. This can be compensated by increasing the potential the atom in recaptured with.

10.3 Two Atom Experiments

Rydberg blockade has been demonstrated between two atoms separated 6 μm attaining a high suppression of populating the doubly excited state $|rr\rangle$ with $P_{rr} < 0.05$ in line with other blockade experiments [141]. Excitation to the entangled symmetric $|\mathcal{W}\rangle$ state has also been demonstrated through observation of a collective $\sqrt{N}$ enhancement in the observed Rabi coupling compared to the single atom case $\Omega' = \sqrt{2}\Omega$.

The entangled $|\mathcal{W}\rangle$ state generated by blockade has been mapped down to the other hyperfine manifold to create the maximally entangled Bell state $|\Psi^+\rangle$. Fidelity of this preparation has been determined through measurement of the off-diagonal elements of the density matrix to obtain a deterministic fidelity of $\mathcal{F} = 0.63 \pm 0.03$. Imperfect Rydberg excitation and atoms being out with the basis states result in losses with the measured recapture probability of two atoms with no blow away pulse $p_{\text{recap}} = 0.78 \pm 0.03$ attaining a loss corrected fidelity of $\mathcal{F}_{\text{pairs}} = 0.81 \pm 0.5$ matching the best post selected Rydberg mediated ground state entanglement fidelity. Table 10.1 shows the current achieved fidelities for neutral atoms including this work.

Species	Method	Deterministic	Post Selected	Ref
^{87}Rb	Blockade	0.46	0.75 ± 0.07	[64]
^{87}Rb	Blockade	0.48 ± 0.07	0.58	[66]
^{87}Rb	Blockade	0.58 ± 0.04	0.71 ± 0.05	[67]
^{133}Cs	Blockade	0.73 ± 0.05	0.79 ± 0.05	[38]
^{87}Rb	Spin Exchange	0.44	0.63 ± 0.02	[44]
^{133}Cs	Dressing	0.6 ± 0.03	0.81± 0.02	[68]
^{87}Rb/^{85}Rb	Blockade	0.59 ± 0.03	-	[69]
^{87}Rb	Blockade	0.91 ± 0.02*	0.97 ± 0.03*	[141]
^{133}Cs	**Blockade**	**0.63 ± 0.03**	**0.81 ± 0.05**	[144]

Table 10.1: Experimentally achieved entanglement fidelities between two neutral atoms following this work, error bars shown when provided in literature. Asterisk indicates Rydberg $|\mathcal{W}\rangle$ state entanglement fidelity rather than ground state entanglement. The work presented in this thesis is highlighted in bold.

It is clear that the Rydberg dephasing issues on the single atoms are prominent in the two atom experiments with laser phase noise limiting transfer to the $|W\rangle$ state being the main source of loss as atoms remaining in the Rydberg state will be lost from the trap. However it is expected implementing upgrades to the laser systems should see the deterministic fidelity reach the loss corrected fidelity and with improvements in optical pumping efficiencies allowing the possibility to exceed it. Experiments have already shown significant advancements through such upgrades to avoid the detrimental effects of laser phase noise with a landmark result showing a deterministic fidelity of $\mathcal{F} = 0.91$ in the $|\mathcal{W}\rangle$ state. Although this fidelity is for ground-Rydberg entanglement one would expect this to have a huge impact when mapping down to create ground state entanglement considering that currently the best deterministic ground state entanglement is $\mathcal{F} = 0.73$ [38].

10.4 Outlook

The final experiment presented in this thesis demonstrated site addressability within the Rydberg blockade radius a necessary step before performing quan-

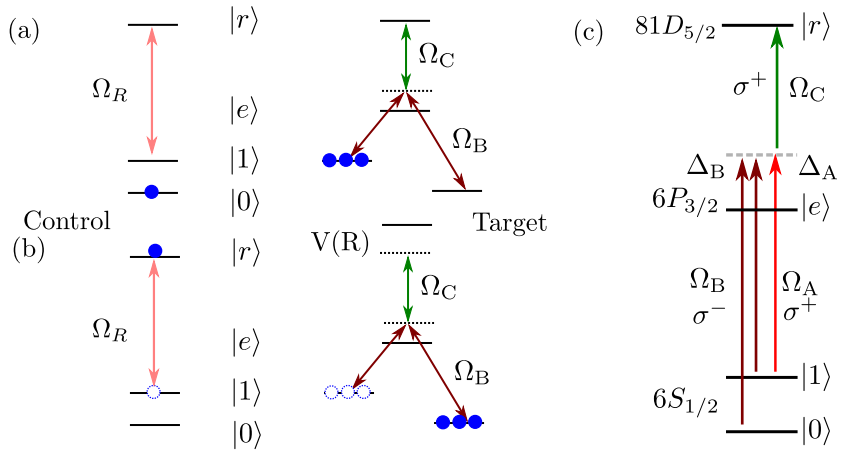

Figure 10.1: Proposed EIT gate, (a) EIT conditions make the Raman lasers transparent to the target atoms and they follow a dark state and remain in $|1\rangle$. (b) The control is excited to the Rydberg state and dipole interactions cause and energy shift lifting EIT conditions allowing Raman transfer between $|1\rangle \rightarrow |0\rangle$. (c) The proposed setup for implementation on the experiment using a phase lock to bring Qubit A and B to a common detuning.

tum gate operations. The next step for the experiment will be to implement a proof of principal demonstration of a mesoscopic gate based on Rydberg electromagnetically induced transparency (EIT), as proposed in [145]. In this proposed gate Rydberg blockade mediates the Raman transfer between hyperfine ground states. An example of the setup for the gate is shown in Fig 10.1. A single atom acts as a control and can be rotated to the Rydberg state if initialised in $|1\rangle$. The target ensemble is controlled by Raman lasers Ω_B which is in two-photon resonance with a coupling laser Ω_C to the Rydberg state. In the situation shown in Fig 10.1(a), where the control is in $|0\rangle$ and the two-photon resonance on the target satisfies the condition $\Omega_C >> \Omega_B$, upon application of the Raman pulse EIT conditions are met and the Raman lasers become transparent to the target ensemble. The ensemble will adiabatically follow a dark state where it remains in $|1\rangle$. Conversely, if the control is initialised in $|1\rangle$ as in Fig 10.1(b), can be excited to the Rydberg state when dipole interactions with the target ensemble shift the two-photon resonance condition for EIT and transfer between $|1\rangle \rightarrow |0\rangle$ can occur. The scheme can be used to realise a C_N gate and combined with Hadamard transformations

used to generate entanglement between a single atom and an ensemble. A significant advantage of this gate is that the target ensemble is not susceptible to a $\sqrt{N}$ enhancement from Rydberg blockade removing the error associated with stochastic numbers loaded in the sample.

The necessary transitions required for this gate have been demonstrated in this work, however experimental realisation requires a common detuning of Qubit A and Qubit B from the intermediate state as shown in Fig 10.1(c). This is currently being setup in the laboratory by phase locking Qubit B to Qubit A, with ground state rotations demonstrated when phase locked. A critical parameter in achieving high fidelity using this gate is that $\Omega_C/\Omega_A \geq 2$ [145]. Due to configuration of the ground state rotation laser implementation requires operation from the clock state, therefore achieving the necessary high coupling strength requires changing to a $nD_{5/2}$ state using a $\sigma^+\sigma^+$ excitation. Further to this $nD_{5/2}$ states have smaller blockade radiuses compared to $nS_{1/2}$ states for an angle of $\theta = \pi/2$ between the atoms therefore reduction of blockade error requires operation at higher n. Due to cavity modes restricting accessible states the target state for this experiment will be $81D_{5/2}$ where $C_6 = -1628$ GHz$\cdot\mu$m^6 and the blockade radius for $\Omega/2\pi = 1$ MHz is $R_b = 10.85$ μm.

Finally, following demonstration of the above gate the experiment will proceed to installation of a cryostat and introduce a superconducting resonator into the science chamber. Immediate goals will be to demonstrate strong coupling between a single atom and the microwave cavity field via the Rydberg state to achieve high fidelity entanglement. Following this the next target will be to demonstrate long distance entanglement (over several mm) between two single atoms by using the resonator to mediate interactions with Rydberg states [72, 146].

Bibliography

[1] C. H. Bennett and G. Brassard, *Quantum Cryptograpy: Public Key Distribution and Coin Tossing*, in *Proceedings of IEEE International Conference on Computers, System and Signal Processing* (IEEE, 1984) p. 175

[2] Artur K. Ekert, *Quantum cryptography based on bell's theorem*, Phys. Rev. Lett. **67**, 661–663 (1991)

[3] Peter W. Shor and John Preskill, *Simple proof of security of the bb84 quantum key distribution protocol*, Phys. Rev. Lett. **85**, 441–444 (2000)

[4] Nicolas Gisin, Grégoire Ribordy, Wolfgang Tittel, and Hugo Zbinden, *Quantum cryptography*, Rev. Mod. Phys. **74**, 145–195 (2002)

[5] D. Deutsch and R. Jozsa, *Rapid solution of problems by quantum computation*, Proceedings of the Royal Society of London A: Mathematical, Physical and Engineering Sciences **439**, 553–558 (1992), ISSN 0962-8444

[6] P. W. Shor, *Polynomial-Time Algorithms for Prime Factorization and Discrete Logarithms on a Quantum Computer*, SIAM J. Comput. **26**, 1484 (1997)

[7] Charles H Bennett, *Quantum information*, Physica Scripta **1998**, 210 (1998)

[8] Andrew Steane, *Quantum computing*, Reports on Progress in Physics **61**, 117 (1998)

[9] M. A. Nielsen and I. L. Chuang, *Quantum Computation and Quantum Information* (CUP, Cambridge, 2005)

[10] Joe O'Gorman and Earl T. Campbell, *Quantum computation with realistic magic-state factories*, Phys. Rev. A **95**, 032338 (2017)

[11] P. J. J. O'Malley *et al.*, *Scalable Quantum Simulation of Molecular Energies*, Phys. Rev. X **6**, 031007 (2016)

[12] Abhinav Kandala *et al.*, *Hardware-efficient variational quantum eigensolver for small molecules and quantum magnets*, Nature **549**, 242 (2017)

[13] Thomas Monz *et al.*, *Realization of a scalable Shor algorithm*, Science **351**, 1068 (2016)

[14] A. Einstein, B. Podolsky, and N. Rosen, *Can Quantum-Mechanical Description of Physical Reality Be Considered Complete?*, Phys. Rev. **47**, 777–780 (1935)

[15] J. S. Bell, *On the Einstein Podolsky Rosen paradox*, Physics Physique Fizika **1**, 195–200 (1964)

[16] S Boughn, *Making Sense of Bell's Theorem and Quantum Nonlocality*, Foundation of Physics **47**, 640 (2017)

[17] Alain Aspect, Philippe Grangier, and Gérard Roger, *Experimental Tests of Realistic Local Theories via Bell's Theorem*, Phys. Rev. Lett. **47**, 460–463 (1981)

[18] Gregor Weihs *et al.*, *Violation of Bell's Inequality under Strict Einstein Locality Conditions*, Phys. Rev. Lett. **81**, 5039–5043 (1998)

[19] L. K. Grover, *Quantum Mechanics Helps in Searching for a Needle in a Haystack*, Phys. Rev. Lett. **79**, 325 (1997)

[20] D. P. DiVincenzo, *The Physical Implementation of Quantum Computation*, Fortschr. Phys. **48**, 771 (2000)

[21] H. Häffner, C.F. Roos, and R. Blatt, *Quantum computing with trapped ions*, Physics Reports **469**, 155 – 203 (2008), ISSN 0370-1573

[22] G Wendin, *Quantum information processing with superconducting circuits: a review*, Rep. Prog. Phys. **80**, 106001 (2017)

[23] M. Saffman, T. G. Walker, and K. Mølmer, *Quantum information with Rydberg atoms*, Rev. Mod. Phys. **82**, 2313 (2010)

[24] J. P. Gaebler *et al.*, *High-fidelity universal gate set for* $^{9}\mathrm{Be}^{+}$ *ion qubits*, Phys. Rev. Lett. **117**, 060505 (2016)

[25] C. J. Ballance *et al.*, *High-fidelity quantum logic gates using trapped-ion hyperfine qubits*, Phys. Rev. Lett. **117**, 060504 (2016)

[26] T. Ruster *et al.*, *A long-lived zeeman trapped-ion qubit*, Applied Physics B **122**, 254 (2016), ISSN 1432-0649

[27] V. M. Schäfer *et al.*, *Fast quantum logic gates with trapped-ion qubits*, Nature **555**, 75 (2018)

[28] S. Debnath *et al.*, *Demonstration of a small programmable quantum computer with atomic qubits*, Nature **536**, 63 (2016)

[29] C. Figgatt *et al.*, *Complete 3-Qubit Grover search on a programmable quantum computer*, Nat. Comm. **8**, 1918 (2017)

[30] R. Barends *et al.*, *Superconducting quantum circuits at the surface code threshold for fault tolerance*, Nature **508**, 500 (2014)

[31] J. Preskill, *Quantum computing and the entanglement frontier* (2012), unpublished, arXiv:1203.5813 [quant-ph]

[32] *Intel advances quantum and neuromorphic computing research* (Accessed 27/09/2018), `https://newsroom.intel.com/news/intel-advances-quantum-neuromorphic-computing-research/`

[33] *The future is quantum* (Accessed 27/09/1992), `https://www.ibm.com/blogs/research/2017/11/the-future-is-quantum/`

[34] *A preview of bristlecone, google's new quantum processor* (Accessed 27/09/92), `https://ai.googleblog.com/2018/03/a-preview-of-bristlecone-googles-new.html`

[35] *The rigetti 128-qubit chip and what it means for quantum* (Accessed 27/09/18), `https://medium.com/rigetti`

[36] R. Grimm, M. Weidemuller, and Y. B. Ovchinnikov, *Optical dipole trap for neutral atoms*, Adv. At. Mol. Opt. Phys. **42**, 170 (2000)

[37] Immanuel Bloch, *Ultracold quantum gases in optical lattices*, Nature Physics **1**, 23 (2005)

[38] K. M. Maller *et al.*, *Rydberg-blockade controlled-not gate and entanglement in a two-dimensional array of neutral-atom qubits*, Phys. Rev. A **92**, 022336 (2015)

[39] T. Xia *et al.*, *Randomized Benchmarking of Single-Qubit Gates in a 2D Array of Neutral-Atom Qubits*, Phys. Rev. Lett. **114**, 100503 (2015)

[40] Daniel Barredo *et al.*, *An atom-by-atom assembler of defect-free arbitrary two-dimensional atomic arrays*, Science **354**, 1021 (2016)

[41] Yang Wang *et al.*, *Coherent Addressing of Individual Neutral Atoms in a 3D Optical Lattice*, Phys. Rev. Lett. **115**, 043003 (2015)

[42] Daniel Barredo *et al.*, *Synthetic three-dimensional atomic structures assembled atom by atom*, Nature **561**, 79–82 (2018)

[43] Y. O. Dudin, L. Li, and A. Kuzmich, *Light storage on the time scale of a minute*, Phys. Rev. A **87**, 031801 (2013)

[44] A. M. Kaufman *et al.*, *Entangling two transportable neutral atoms via local spin exchange*, Nature **527**, 208 (2015)

[45] M. Saffman, *Quantum computing with atomic qubits and Rydberg interactions: progress and challenges*, J. Phys. B **49**, 202001 (2016)

[46] M. D. Lukin *et al.*, *Dipole Blockade and Quantum Information Processing in Mesoscopic Atomic Ensembles*, Phys. Rev. Lett. **87**, 037901 (2001)

[47] Klaus Mølmer, Larry Isenhower, and Mark Saffman, *Efficient Grover search with Rydberg blockade*, J. Phys. B **44**, 184016 (2011)

[48] David Petrosyan, Mark Saffman, and Klaus Mølmer, *Grover search algorithm with Rydberg-blockaded atoms: quantum Monte Carlo simulations*, J. Phys. B **49**, 094004 (2016)

[49] Henning Labuhn *et al.*, *Tunable two-dimensional arrays of single Rydberg atoms for realizing quantum Ising models*, Nature **534**, 667 (2016)

[50] Hannes Bernien *et al.*, *Probing many-body dynamics on a 51-atom quantum simulator*, Nature **551**, 579 (2017)

[51] Vincent Lienhard *et al.*, *Observing the space- and time-dependent growth of correlations in dynamically tuned synthetic ising models with antiferromagnetic interactions*, Phys. Rev. X **8**, 021070 (Jun 2018)

[52] Elmer Guardado-Sanchez *et al.*, *Probing the quench dynamics of antiferromagnetic correlations in a 2d quantum ising spin system*, Phys. Rev. X **8**, 021069 (Jun 2018)

[53] D. Tong *et al.*, *Local Blockade of Rydberg Excitation in an Ultracold Gas*, Phys. Rev. Lett. **93**, 063001 (2004)

[54] K. Singer *et al.*, *Suppression of Excitation and Spectral Broadening Induced by Interactions in a Cold Gas of Rydberg Atoms*, Phys. Rev. Lett. **93**, 163001 (2004)

[55] R. Heidemann *et al.*, *Evidence for Coherent Collective Rydberg Excitation in the Strong Blockade Regime*, Phys. Rev. Lett. **99**, 163601 (2007)

[56] J. D. Pritchard *et al.*, *Cooperative Atom-Light Interaction in a Blockaded Rydberg Ensemble*, Phys. Rev. Lett. **105**, 193603 (2010)

[57] N. Schlosser, G. Reymond, I. Protsenko, and P. Grangier, *Sub-poissonian loading of single atoms in a microscopic dipole trap*, Nature **411**, 1024 (2001)

[58] N. Schlosser, G. Reymond, and P. Grangier, *Collisional Blockade in Microscopic Optical Dipole Traps*, Phys. Rev. Lett. **89**, 023005 (2002)

[59] D. D. Yavuz *et al.*, *Fast ground state manipulation of neutral atoms in microscopic optical traps*, Phys. Rev. Lett. **96**, 063001 (2006)

[60] T. A. Johnson *et al.*, *Rabi Oscillations between Ground and Rydberg States with Dipole-Dipole Atomic Interactions*, Phys. Rev. Lett. **100**, 113003 (2008)

[61] Y. Miroshnychenko *et al.*, *Coherent excitation of a single atom to a rydberg state*, Phys. Rev. A **82**, 013405 (2010)

[62] E. Urban *et al.*, *Observation of Rydberg blockade between two atoms*, Nature Phys. **5**, 110 (2009)

[63] A. Gaëtan *et al.*, *Observation of collective excitation of two individual atoms in the Rydberg blockade regime*, Nature Phys. **5**, 115 (2009)

[64] T. Wilk *et al.*, *Entanglement of Two Individual Neutral Atoms Using Rydberg Blockade*, Phys. Rev. Lett. **104**, 010502 (2010)

[65] A Gaëtan *et al.*, *Analysis of the entanglement between two individual atoms using global Raman rotations*, N. J. Phys. **12**, 065040 (2010)

[66] L. Isenhower *et al.*, *Demonstration of a Neutral Atom Controlled-NOT Quantum Gate*, Phys. Rev. Lett. **104**, 010503 (2010)

[67] X. L. Zhang *et al.*, *Deterministic entanglement of two neutral atoms via Rydberg blockade*, Phys. Rev. A **82**, 030306 (2010)

[68] Y.-Y. Jau *et al.*, *Entangling atomic spins with a Rydberg-dressed spin-flip blockade*, Nat. Phys. **12**, 71 (2016)

[69] Yong Zeng *et al.*, *Entangling Two Individual Atoms of Different Isotopes via Rydberg Blockade*, Phys. Rev. Lett. **119**, 160502 (2017)

[70] S. D. Hogan *et al.*, *Driving Rydberg-Rydberg Transitions from a Coplanar Microwave Waveguide*, Phys. Rev. Lett. **108**, 063004 (2012)

[71] J. D. Pritchard, K. J. Weatherill, and C. S. Adams, *Non-linear optics using cold Rydberg atoms*, Ann. Rev. Cold. Atoms and Mol. **1**, 301 (2013)

[72] D. Petrosyan and M. Fleischhauer, *Quantum Information Processing with Single Photons and Atomic Ensembles in Microwave Coplanar Waveguide Resonators*, Phys. Rev. Lett. **100**, 170501 (2008)

[73] Adriano Barenco *et al.*, *Elementary gates for quantum computation*, Phys. Rev. A **52**, 3457–3467 (1995)

[74] J. D. Pritchard, *Cooperative Optical Non-Linearity in a Blockaded Rydberg Ensemble* (Springer-Verlag, Berlin, 2012)

[75] N. Šibalić, J. D. Pritchard, C. S. Adams, and K. J. Weatherill, *ARC: An open-source library for calculating properties of alkali Rydberg atoms*, Comp. Phys. Comm. **220**, 319–331 (2017)

[76] L R Pendrill, D Delande, and J C Gay, *Quantum defect and fine-structure measurements of p, d, f and g rydberg states of atomic caesium*, Journal of Physics B: Atomic and Molecular Physics **12**, L603 (1979)

[77] P. Goy, J. M. Raimond, G. Vitrant, and S. Haroche, *Millimeter-wave spectroscopy in cesium rydberg states. quantum defects, fine- and hyperfine-structure measurements*, Phys. Rev. A **26**, 2733 (1982)

[78] C. J. Lorenzen and K. Niemax, *Precise quantum defects of nS, nP and nD Levels in Cs I*, Z. Phys. A **315**, 127 (1984)

[79] K.-H. Weber and Craig J. Sansonetti, *Accurate energies of nS , nP , nD , nF , and nG levels of neutral cesium*, Phys. Rev. A **35**, 4650–4660 (1987)

[80] I. I. Beterov, I. I. Ryabtsev, D. B. Tretyakov, and V. M. Entin, *Quasiclassical calculations of blackbody-radiation-induced depopulation rates and effective lifetimes of Rydberg nS, nP, and nD alkali-metal atoms with $n \leq 80$*, Phys. Rev. A **79**, 052504 (2009)

[81] D. A. Steck, *Cesium D Line Data*, http://steck.us/alkalidata

[82] A. Reinhard, T. Cubel Liebisch, B. Knuffman, and G. Raithel, *Level shifts of rubidium Rydberg states due to binary interactions*, Phys. Rev. A **75**, 032712 (2007)

[83] Sylvain Ravets *et al.*, *Measurement of the angular dependence of the dipole-dipole interaction between two individual rydberg atoms at a förster resonance*, Phys. Rev. A **92**, 020701 (2015)

[84] C. J. Foot, *Atomic Physics* (OUP, Oxford, 2005)

[85] E Brion, L H Pedersen, and K Mølmer, *Adiabatic elimination in a lambda system*, Journal of Physics A: Mathematical and Theoretical **40**, 1033 (2007)

[86] R. Loudon, *The Quantum Theory of Light*, 3rd ed. (OUP, UK, 2008)

[87] Sylvain Ravets, *Development of tools for quantum engineering using individual atoms*, Ph.D. thesis, Institut D'Optique Graduate School (2014)

[88] I. I. Sobelman, *Atomic Spectra and Radiative Transitions* (Springer-Verlag, Berlin, 1979)

[89] J. Halbritter, *On the oxidation and on the superconductivity of niobium*, Applied Physics A **43**, 1–28 (1987)

[90] J. D. Pritchard, J. A. Isaacs, and M. Saffman, *Long working distance objective lenses for single atom trapping and imaging*, Rev. Sci. Inst. **87**, 073107 (2016)

[91] Y. R. P. Sortais *et al.*, *Diffraction-limited optics for single-atom manipulation*, Phys. Rev. A **75**, 013406 (2007)

[92] L. Béguin *et al.*, *Direct measurement of the van der waals interaction between two rydberg atoms*, Phys. Rev. Lett. **110**, 263201 (2013)

[93] L. Béguin, *Measurement of the van der Waals interaction between two Rydberg atoms*, Ph.D. thesis, Institut D'Optique Graduate School (2013)

[94] Paul D. Lett *et al.*, *Observation of atoms laser cooled below the doppler limit*, Phys. Rev. Lett. **61**, 169–172 (1988)

[95] David S. Weiss *et al.*, *Optical molasses and multilevel atoms: experiment*, J. Opt. Soc. Am. B **6**, 2072–2083 (1989)

[96] J. Dalibard and C. Cohen-Tannoudji, *Laser cooling below the Doppler limit by polarisation gradients: simple theoretical models*, J. Opt. Soc. Am. B **6**, 2023 (1989)

[97] A. M. Steane and C. J. Foot, *Laser Cooling below the Doppler Limit in a Magneto-Optical Trap*, Europhys. Lett. **14**, 231 (1991)

[98] A. S. Arnold, J. S. Wilson, and M. G. Boshier, *A simple extended-cavity diode laser*, Rev. Sci. Inst. **69**, 1236–1239 (1998)

[99] M. L. Harris *et al.*, *Polarization spectroscopy in rubidium and cesium*, Phys. Rev. A **73**, 062509 (2006)

[100] Rowan W. G. Moore *et al.*, *Measurement of vacuum pressure with a magneto-optical trap: A pressure-rise method*, Review of Scientific Instruments **86** (2015)

[101] C. G. Townsend *et al.*, *Phase-space density in the magneto-optical trap*, Phys. Rev. A **52**, 1423 (1995)

[102] C. Salomon *et al.*, *Laser cooling of cesium atoms below 3 k*, EPL (Europhysics Letters) **12**, 683 (1990)

[103] Julian Léonard *et al.*, *Optical transport and manipulation of an ultracold atomic cloud using focus-tunable lenses*, N. J. Phys. **16**, 093028 (2014)

[104] P. Phoonthong, P. Douglas, A. Wickenbrock, and F. Renzoni, *Characterization of a state-insensitive dipole trap for cesium atoms*, Phys. Rev. A **82**, 013406 (2010)

[105] W. Alt, *An objective lens for efficient fluorescence detection of single atoms*, Optik **113**, 142 (2002)

[106] B. J. Lester, A. M. Kaufman, and C. A. Regal, *Raman cooling imaging: Detecting single atoms near their ground state of motion*, Phys. Rev. A **90**, 011804 (2014)

[107] J. Sherson *et al.*, *Single-atom-resolved fluorescence imaging of an atomic Mott insulator*, Nature **467**, 68 (2010)

[108] V. Y. F. Leung *et al.*, *Magnetic-film atom chip with 10 μm period lattices of microtraps for quantum information science with Rydberg atoms*, Rev. Sci. Inst. **85**, 053102 (2014)

[109] Minho Kwon, Matthew F. Ebert, Thad G. Walker, and M. Saffman, *Parallel Low-Loss Measurement of Multiple Atomic Qubits*, Phys. Rev. Lett. **119**, 180504 (2017)

[110] D. B. Hume *et al.*, *Accurate Atom Counting in Mesoscopic Ensembles*, Phys. Rev. Lett. **111**, 253001 (2013)

[111] W. Nagourney, G. Janik, and H. Dehmelt, *Linewidth of single laser-cooled 24Mg+ ion in radiofrequency trap*, Proc. Natl. Acad. Sci. **80**, 643 (1983)

[112] T. Grunzweig, A. Hilliard, M. McGovern, and M. F. Andersen, *Near-deterministic preparation of a single atom in an optical microtrap*, Nat Phys, 951–954(2010)

[113] A. Fuhrmanek, Y. R. P. Sortais, P. Grangier, and A. Browaeys, *Measurement of the atom number distribution in an optical tweezer using single-photon counting*, Phys. Rev. A **82**, 023623 (2010)

[114] C. J. Picken, R. Legaie, and J. D. Pritchard, *Single atom imaging with an sCMOS camera*, App. Phys. Lett. **111**, 164102 (2017)

[115] S Fullerton, K Bennett, E. Toda, and T Takahashi, *Optimization of precision localization microscopy using cmos camera technology*, Proc. SPIE **8228**, 82280T (2012)

[116] Hamamatsu, *Digital CCD Camera ORCA-R2* (2013), http://www.hamamatsu.com.cn/UserFiles/DownFile/Product/SCAS0054E03_C10600-10B.pdf

[117] Andor Technologies, *Andor iXon ULTRA EMCCD Specifications (Rev. 4)* (07 2017), http://www.andor.com/pdfs/specifications/Andor_iXon_ULTRA_EMCCD_Specifications.pdf

[118] Venkataraman Krishnaswami, Cornelis J F. Van Noorden, Erik M M. Manders, and Ron A. Hoebe, *Towards digital photon counting cameras for single-molecule optical nanoscopy*, Opt. Nano. **3**, 1 (2014)

[119] Hongqiang Ma *et al.*, *Localization-based super-resolution microscopy with an sCMOS camera part III: camera embedded data processing significantly reduces the challenges of massive data handling*, Opt. Lett. **38**, 1769 (2013)

[120] Andor Technologies, *Zyla for Physical Sciences Specifications (Rev. 1)* (05 2017), http://www.andor.com/pdfs/specifications/Andor_Zyla_for_Physical_Sciences_Specifications.pdf

[121] Yin H. Fung, Alicia V. Carpentier, Pimonpan Sompet, and Mikkel Andersen, *Two-atom collisions and the loading of atoms in microtraps*, Entropy **16**, 582–606 (2014)

[122] Yin Fung, Pimonpan Sompet, and Mikkel Andersen, *Single atoms preparation using light-assisted collisions*, Technologies **4**, 4 (2016)

[123] Alicia V Carpentier *et al.*, *Preparation of a single atom in an optical microtrap*, Laser Physics Letters **10**, 125501 (2013)

[124] Brian J. Lester *et al.*, *Rapid production of uniformly filled arrays of neutral atoms*, Physical Review Letters **115** (2015)

[125] Georges Reymond, Nicolas Schlosser, Igor Protsenko, and Philippe Grangier, *Single-atom manipulations in a microscopic dipole trap*, Philosophical Transactions of the Royal Society of London A: Mathematical, Physical and Engineering Sciences **361**, 1527–1536 (2003)

[126] J. Beugnon *et al.*, *Two-dimensional transport and transfer of a single atomic qubit in optical tweezers*, Nature Phys. **3**, 696–699 (2007)

[127] C. Tuchendler *et al.*, *Energy distribution and cooling of a single atom in an optical tweezer*, Phys. Rev. A **78**, 033425 (2008)

[128] Yue-Sum Chin, Matthias Steiner, and Christian Kurtsiefer, *Polarization gradient cooling of single atoms in optical dipole traps*, Phys. Rev. A **96**, 033406 (2017)

[129] A. M. Kaufman, B. J. Lester, and C. A. Regal, *Cooling a Single Atom in an Optical Tweezer to Its Quantum Ground State*, Phys. Rev. X **2**, 041014 (2012)

[130] J. D. Thompson *et al.*, *Coherence and Raman Sideband Cooling of a Single Atom in an Optical Tweezer*, Phys. Rev. Lett. **110**, 133001 (2013)

[131] P. Sompet *et al.*, *Zeeman-insensitive cooling of a single atom to its two-dimensional motional ground state in tightly focused optical tweezers*, Phys. Rev. A **95**, 031403 (2017)

[132] Andreas Bauch, *Caesium atomic clocks: function, performance and applications*, Measurement Science and Technology **14**, 1159 (2003)

[133] S. Kuhr *et al.*, *Analysis of dephasing mechanisms in a standing-wave dipole trap*, Phys. Rev. A **72**, 023406 (2005)

[134] M. Dornseifer D. Haubrich and R. Wynands, *Lossless beam combiners for nearly equal laser frequencies*, Rev. Sci. Inst. **71**, 338 (2000)

[135] T. G. Walker and M. Saffman, *Entanglement of Two Atoms using Rydberg Blockade*, Adv. At. Mol. Opt. Phys. **61**, 81 (2012)

[136] T Müller *et al.*, *Towards a guided atom interferometer based on a superconducting atom chip*, N. J. Phys. **10**, 073006 (2008)

[137] A. M. Hankin *et al.*, *Two-atom Rydberg blockade using direct 6S to nP excitation*, Phys. Rev. A **89**, 033416 (2014)

[138] R. Legaie, C. J. Picken, and J. D. Pritchard, *Sub-kHz excitation lasers for Quantum Information Processing with Rydberg atoms*, J. Opt. Soc. Am. B **35**, 892 (2018)

[139] Sylvain de Léséleuc *et al.*, *Analysis of imperfections in the coherent optical excitation of single atoms to Rydberg states*, Phys. Rev. A **97**, 053803 (2018)

[140] H. Saßmannshausen, F. Merkt, and J. Deiglmayr, *High-resolution spectroscopy of Rydberg states in an ultracold cesium gas*, Phys. Rev. A **87**, 032519 (2013)

[141] Harry Levine *et al.*, *High-Fidelity Control and Entanglement of Rydberg-Atom Qubits*, Phys. Rev. Lett. **121**, 123603 (2018)

[142] L. Isenhower, *Demonstration of Rydberg Blockade, a Neutral Atom CNOT Gate, and Entanglement Generation*, Ph.D. thesis, University of Wisconsin-Madison (2010)

[143] Q. A. Turchette *et al.*, *Deterministic Entanglement of Two Trapped Ions*, Phys. Rev. Lett. **81**, 3631 (1998)

[144] C J Picken, R Legaie, K McDonnell, and J D Pritchard, *Entanglement of neutral-atom qubits with long ground-rydberg coherence times*, Quantum Science and Technology **4**, 015011 (2019)

[145] M. Müller *et al.*, *Mesoscopic Rydberg Gate Based on Electromagnetically Induced Transparency*, Phys. Rev. Lett. **102**, 170502 (2009)

[146] L őrinc Sárkány, József Fortágh, and David Petrosyan, *Long-range quantum gate via rydberg states of atoms in a thermal microwave cavity*, Phys. Rev. A **92**, 030303 (2015)